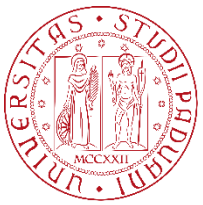

UNIVERSITA' DEGLI STUDI DI PADOVA

DIPARTIMENTO DI SCIENZE CHIMICHE

CORSO DI LAUREA MAGISTRALE IN CHIMICA

TESI DI LAUREA MAGISTRALE

Photodegradation of encapsulated terpenoids studied by Raman spectroscopy

Relatore: Prof. Moreno Meneghetti

Correlatore: Dott. Lucio Litti

Controrelatore: Prof.ssa Cristina Peggion

LAUREANDO: Cardoni Francesco

ANNO ACCADEMICO 2021/2022

Table of contents

1. Abstract

Terpenoids are playing a major role in agriculture, given their fungicidal and herbicidal action, as well as their favorable toxicological, ecotoxicological and environmental profile. Despite all these advantages, terpenoids are reported of being unstable to direct sunlight and atmospheric conditions, so that both commercial suppliers and scientific literature foresee their protection by encapsulation. This thesis is therefore dedicated to determining whether, and to what extent, terpenoids photoprotection against UV light is needed, and which are the strategies to make it more effective. The terpenoids under consideration were eugenol, thymol and geraniol. Increasingly more sophisticated encapsulations were designed and prepared in order to provide a gradually opaquer covering shell, starting from a surfactant (soybean lecithin) to a complex shell made of gold nanostars covered with chitosan. Confocal micro-Raman was used to provide a deep morphological description of the terpenoids microbeads before and after a prolonged UV irradiation. The results of this study shed new light on the photo-instability of the microcapsules and terpenoids under investigation, which resulted much more resistant than expected.

2. Introduction

2.1 Terpenoids: an overview

Terpenes are a subclass of secondary metabolites typical of living organisms, alongside alkaloids, shikimates, and polyketides. This classification depends on the biosynthetic pathway used by the organisms to produce these products. Terpenes are therefore defined as compounds with molecular structures containing carbon backbones made up of isoprene (2-methylbuta-1,3-diene, C_5H_8) units. Isoprene contains five carbon atoms and, therefore, the number of carbon atoms in any terpene is a multiple of five. [1] According to the so-called "isoprene rule", established by Otto Wallach in 1887 and subsequently refined by other authors (R. Robinson and L. Ružiča), each terpene is basically composed from isoprene units mainly in head-to-tail fashion, either directly or by cyclization rearrangements, or further conversions means. [2]

Terpenoids are a modified class of terpenes with different functional groups and oxidized methyl groups placed, or removed, at various positions. [3,4] More specifically, terpenoids derive from the C_5– building blocks isopentenyl diphosphate (IPP) and its isomer dimethylallyl diphosphate (DMAPP). [5]

The majority of terpenoids are colorless, non-polar, volatile, and hydrophobic. They possess one or more double bonds, a property that makes them prone to undergo addition reactions (with hydrogen, halogens, and acids) as well as polymerization and dehydrogenation. They are easily oxidized by nearly all oxidizing agents. The thermal decomposition yields isoprene as one of the major products. [6,7]

In Nature, terpenoids are produced by a wide variety of plants, animals and microorganisms, often as major components in essential oils (EOs). [8] The preferred method for their extraction from the EOs of origin is hydrodistillation, alongside other classic extraction techniques such as soxhletation, solvent extraction and pressurized liquid extraction. [4,5] However, with the growing energy prices and associated CO_2 emissions, there is a growing interest in developing novel, "greener" techniques to extract the pure terpenoids from EOs. These alternative techniques include trend-setting technologies such as supercritical carbon dioxide extraction, static headspace extraction and microwave-assisted hydrodistillation (MWHD). [9–11]

The roles which the terpenoids play in living organisms can be grouped into three classes: functional, communication and defense. Examples of terpenoids playing the functional role include vitamin A (precursor of the pigment responsible for the sense of sight in the eyes) and vitamin E (an antioxidant which prevents oxidative damage to cells). Examples regarding the communication function of terpenoids include hormones as gibberellic acid (regulator of growth

rate in plants), pheromones as *d*-limonene (Australian termites' alarm agent) and allelochemicals as camphor (protector against insect attacks in plants). Lastly, as far as the defense function of terpenoids is concerned, terpenoids-based resins are produced by damaged plants as physical barrier to infectious organisms. In addition, terpenoids are also produced by plants and animals to make themselves unattractive to predators. [1]

Thanks to these properties, terpenoids as well as many essential oils of natural origin are used in a variety of anthropogenic fields to improve human life: in the medical sector thanks to their antimicrobial, antiviral, anthelminthic, antiulcer and anti-inflammatory actions, in the food industry given their antioxidant and flavoring actions, and in the agricultural field because of their herbicide, antifungal and insect pest repellent properties. [4,12,13]

The need for new pesticides ("biopesticides") is dictated by the fact that many conventional synthetic pesticides do not comply with the requirements of modern agriculture. [14] One of the major problems is associated with synthetic pesticide residues, often found in foods at concentrations above the recommended limits, which ultimately can have negative effects on human health. Other problems include the side-action of synthetic pesticides to non-targeted organisms, which is associated to the development of pathogen and insect populations resistant to the synthetic active principles. [15]

All the properties of terpenoids presented above, combined with other unique properties such as low toxicity, biodegradability, and renewable source-based production,[16] make their class an excellent candidate for use in the modern agricultural industry.

This thesis work focuses on the study of a mixture of three terpenoids: eugenol, thymol and geraniol. The following chapter will highlight specific properties and current commercial uses of these three compounds that are increasingly being utilized in agriculture.

2.1.1 Agricultural usage of eugenol, thymol and geraniol

Figure 2.1 shows the molecular structures of the three terpenoids studied in this thesis work.

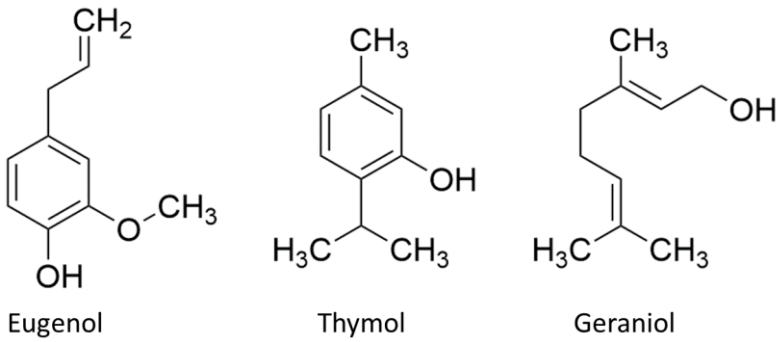

Figure 2.1. Molecular structures of the terpenoids mixture used as the active principle for this thesis work.

Eugenol is a monocyclic terpenoid which constitutes a main component in *Syzygium aromaticum* essential oil (EO).[17] It presents high toxicity against sanitary pest insects, mites, and nematodes. It possesses contact toxicity against a variety of insects and parasites (American cockroach, *Blattella germanica*, carpenter ants and *Dermanyssus gallinae*), as well as fumigation toxicity against a multitude of moths and bedbugs (*Plutella xylostella*, *Cimex lectularius*, *Bemisia procera* and *Bemisia tabaci*). Eugenol has also repellent action against second-stage juveniles of *Caenorhabditis elegans*, *Meloidogyne javanica* and *Meloidogyne incognita*. [18]

Thymol is a monocyclic terpenoid which constitutes the main component of *Saccocalyx satureioides* and *Lippia gracilis* EOs. [19] It has shown a multitude of biological activities: contact toxicity towards larvae and mites (*Culex quinquefasciatus*, *Spodoptera littoralis*, coconut mite, red palm mite, *D. gallinae*), fumigant toxicity against parasites (*P. xylostella*, *B. tabaci*), topical and fumigant toxicity against bedbugs (*C. lectularius*), topical toxicity against *Trichoplusia ni*, and ovicidal and larvicidal toxicity against *Culex pipiens*. Thymol-containing EOs from *Trachyspermum ammi* have antigrowth activities against *Aspergillus flavus*. Thymol is also antifungal against *Fusarium graminearum*, *Colletotrichum fructicola* and *Colletotrichum acutatum*, while at the same time exhibiting antibacterial properties against *Agrobacterium tumefaciens* and *Erwinia carotovora*. [19] Furthermore, thymol shows herbicidal properties and inhibits the germination and growth of a variety of infesting weeds such as *Amaranthus retroflexus*, *C. album* and *Rumex crispus*. Lastly, it is repellent against second-stage juveniles and adults of *C. elegans*, *M. incognita* and *Ascaris suum*. [18,20]

Geraniol is an acyclic monoterpenoid which is toxic to sanitary and stored product pest insects, phytopathogenic fungi and pest nematodes. It has shown contact activity against bedbugs (*C. lectularius*) and fumigant toxicity towards *B. tabaci*. The EO extracted from *Melissa officinalis*, which contains a high quantity of geraniol, has demonstrated to be an excellent repellent against *Tribolium castaneum*, given its good contact and fumigant toxicities towards this infesting beetle. Geraniol is also an antifungal against *C. fructicola* and *C. acutatum*. Lastly, it is nematicidal against second-stage juveniles of *M. javanica*, *C. elegans* and *M. incognita*. [18]

Z. Liu *et al.* [18] report that the putative insecticidal modes of action of the three terpenoids consist in their neuroinhibitory effects on the thoracic ganglion of insects, inhibition of transient receptor potential (TRP) channels and reduction of spontaneous and irritating impulses outside the ventral nerve cord cells of insects. As far as the putative antiphytopathogenic mode of action is concerned, it has been reported that geraniol and thymol destroy the integrity of cell walls and cell plasma membranes, reduce the cell metabolism and accumulate reactive oxygen species (ROS). The putative herbicidal mode of action of thymol consists in causing oxidative damage in

infesting root tissue. Lastly, the putative nematicidal mode of action takes place through the inhibition of the acetylcholinesterase enzyme (AChE), as well as the action on the tyramine receptors in nematode cells. In addition, a synergistic effect between eugenol and thymol has been demonstrated, which could result from a simultaneous action on multiple targets in the insect nervous system. [21]

There are many formulations on the market that use a mixture of the three above-mentioned terpenoids, with properties ranging from antibotritic to repellent towards nematodes. Examples include 3LOGY® and Andromeda® (marketed in Italy by Sipcam Italia S.P.A.), as well as Cedroz® (marketed by Eastman Italia S.R.L.). [22] The proportion of the active principles varies across the range of products, as well as the composition. As an example, 3LOGY® consists of a proportion of 1:2:2, by means of eugenol, thymol and geraniol, respectively. On the contrary, Cedroz® consists of a mixture of thymol and geraniol only, in a proportion of 1:3. According to the manufacturers, these products are a copy of the natural defense mechanisms of plants, are free of maximum residue limit (MRL), and have an effective protective action which can also prevent resistance phenomena. [23,24]

However, these commercial formulations contain other compounds besides terpenoids. The terpenoids mixtures are encapsulated in complex microbeads whose purpose is to protect the active ingredients and to promote their release depending on atmospheric conditions (*e.g.*, humidity) when the latter could lead to favorable conditions for pest growth. [24] In fact, as the next chapter will describe, specialized literature reports that terpenoids are unstable under certain conditions of light, temperature, and oxygen availability.

2.1.2 Stability of terpenoids

Once deprived of their protective structures in the plant matrix, EOs constituents are prone to oxidation, chemical transformations, or polymerization reactions. Often, the degradation can be recognized macroscopically by the appearance of unpleasant and pungent flavors, the shift in the color of the solution, usually to a dark yellow staining, and changes in viscosity, up to the formation of resins. [25,26]

One of the chemical reactions mainly responsible for the degradation of terpenoids is autoxidation, a well-known reaction especially in the field of fatty acids. Autoxidation is defined as the spontaneous oxidation of a substance at ambient temperatures in the presence of oxygen. Unsaturated molecules react in a free radical chain reaction mechanism with atmospheric oxygen, yielding a range of primary and secondary oxidation products. **Figure 2.2** shows the autoxidation

reaction general scheme. Alkyl radicals are initially generated, promoted by heat, catalytic quantities of redox-reactive metals or exposure to light (**Fig. 2.2 (1)**). The generated alkyl radicals react almost immediately with triplet oxygen to form peroxyl radicals (**Fig. 2.2 (3)**). [5] As far as the initiation step is concerned, another alternative reaction can take place whether trace levels of peroxides are present in the solution (**Fig. 2.2 (2)**). [27] Peroxyl radicals formed in the propagation step selectively abstract weakly bounded hydrogen atoms adjacent to double bonds. This leads to the formation of hydroperoxides and another alkyl radical (**Fig. 2.2 (4)**), which can now propagate the radical chain reaction. Other propagation steps can also involve the generation of epoxides (R>O in **Fig. 2.2 (6)**), alcohols (ROH in **Fig. 2.2 (7)**) and ketones (R=O in **Fig. 2.2 (8)**), as proposed by Neuenschwander *et al*. [28] As far as the termination step is concerned, radicals combine to alkyl and peroxyl dimers, which may polymerize or decompose further to nonradical products (**Fig. 2.2 (10–12)**). [28,29]

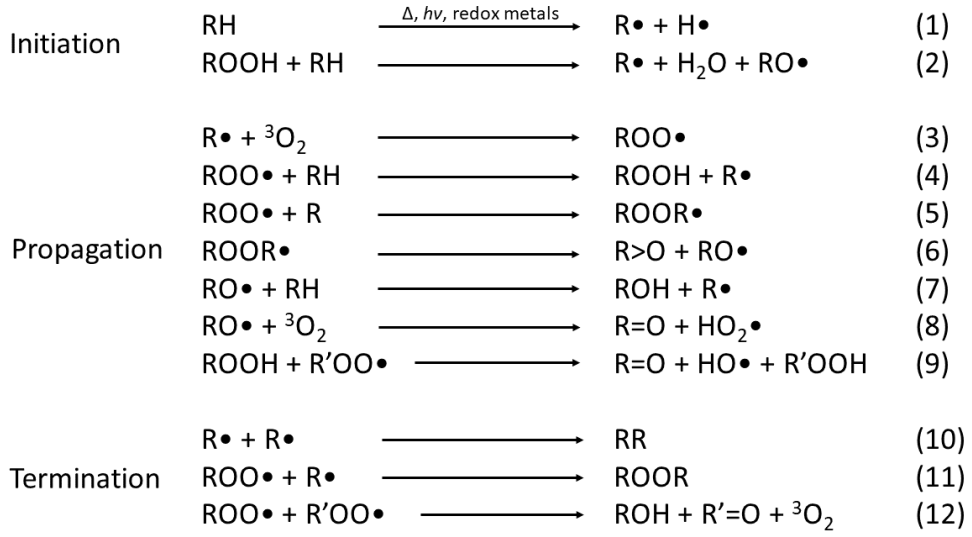

Figure 2.2. Main mechanisms of the autoxidation radical chain reaction. [28,29]

Light, temperature, and accessibility to atmospheric oxygen are so far the main factors favoring the ignition of the terpenoid degradation cited above. [5] In fact, it is reported that, at elevated temperatures and under the presence of light, the amounts of unsaturated terpenes remarkably decrease over time, while at the same time the amounts of oxidized compounds increase. [30,31]

According to Choe *et al.*, ultraviolet (UV) and visible (Vis) light can accelerate the autoxidation process by facilitating the hydrogen abstraction, which ultimately results in the formation of alkyl radicals. [29] Indeed, it has been shown that two identical solutions of EOs, one placed in sunlight and the other placed in the dark, will degrade producing similar degradation products. However, the degradation rate is considerably faster for the sunlight-irradiated solution, especially as far as monoterpenes are concerned. [31] In addition, sunlight irradiation plays a fundamental role in the

photooxidation process, another degradation pathway. During the photooxidation process, triplet oxygen is converted into its excited singlet state ($^1O_2$) by an organic photosensitizer. $^1O_2$ is a nonradical electrophilic molecule which can directly react with a double bond, ultimately abstracting an allylic hydrogen atom to form hydroperoxides. These hydroperoxides decompose in the same fashion as the ones formed by autoxidation (**Fig. 2.2 (9)**). However, for photooxidation to occur, it is required the presence of a photosensitizer, such as chlorophylls or porphyrins, which are generally absent in distilled EOs. [32] As for the terpenoids under study in this thesis work, Jhones Luiz de Oliveira *et al.* report that terpenoids, geraniol in particular, are susceptible to degradation when irradiated by a 365 nm UV light. [33]

Temperature is also an important parameter for the stability of terpenoids. [34] Even if only considering the Arrhenius equation, a generic reaction rate increases following the temperature of the system. Thus, increasing the temperature will lead to an increase in the speed of reactions of autoxidation and hydroperoxide decomposition, also considering that heat is one of the factors contributing to the initiation step of the radical chain reaction of autoxidation. [29] On the contrary, low temperatures favor the solubility of oxygen in liquids, ultimately affecting in a negative manner the stability of terpenoids, as will be discussed in the next paragraph. Another fact to consider is that terpenoids, especially aldehydes and mere terpenes, are thermolabile and undergo rearrangement processes as the temperature raises. Thermal degradation of terpenes and terpenoids has been classified into four different categories of oxidative reactions: cleavage of double bonds, epoxidation, dehydrogenation to form aromatic systems, and allylic oxidation into oxygen-containing species, such as alcohols, ketones and aldehydes. [35]

The last factor considered to be crucial for the stability of terpenoids is oxygen availability. It is obvious that as oxygen availability increases (*e.g.*, in a half-filled closed container rather than in a fully filled one), the degree of degradation contributed by autoxidation also increases. Moreover, the oxidation rate appears to accelerate as the available oxygen concentration increases. As stated before, the concentration of dissolved oxygen in a terpenoids solution is inversely proportional to the solution temperature, according to Henry's law. Hence, at low temperatures, peroxyl radicals as well as hydroperoxides are the most abundant oxidation products. [36] Compounds which are characteristics of the termination step of the autoxidation radical chain reaction, such as polymers, are formed only when either the amount of oxygen or oxidable substrate are exhausted. [5] Only by treating the terpenoids under an inert gas atmosphere, such as argon, the formation of peroxides can be averted, and the degradation degree of the solution lowered. [36]

The importance of proper storage conditions derives mainly from the facts discussed above, namely minimizing the amount of oxygen, light, and so on. It has been proposed, and verified, that storage at freezing temperatures (–20° C) is the best method to properly retain compounds such as thymol. [37]

Aside from these concepts, it has also been shown that alterations of each compound depend on the presence of other molecules in solution. Phenols such as eugenol, thymol and carvacrol are known to be protective towards other molecules more susceptible to oxidation reactions. [38] Their antioxidant action takes place by rapidly abstracting the phenolic oxygen atom, ultimately forming relatively long-living radicals stabilized by the possibility of delocalization of the unpaired electron on the aromatic ring, resulting in several various resonance structures. These so-called primary antioxidants will subtract further free reactive radicals from the solution (alkyl, alkoxy or peroxyl radicals), increasing the overall stability of the mixture. [39] In fact, N. Tiwari *et al.* reported the augmented stability against photooxidation of an active pharmaceutical ingredient, itraconazole, which has been micro-emulsified in the presence of eugenol. The increased stability of the active principle is due to the significant protective activity of eugenol in the 265–287 nm wavelength range of the light spectrum. [40]

Upon all the considerations about the instability of terpenoids in the presence of light (UV and Vis), over a wide range of temperatures (lower as well as higher), and in the presence of available oxygen, it is no coincidence that a multitude of terpenoid-containing formulations are encapsulated into protective matrices to allow for greater preservation. The next chapter will investigate the encapsulation aspects in detail.

2.1.3 Microencapsulation of terpenoids

The application of pure terpenoid formulations on the agricultural field faces many problems. In particular, the main issue regards the degradability of terpenoids under mild atmospheric conditions. In fact, as seen above, terpenoids, as well as other EOs constituents, are volatile and thermolabile, susceptible to autoxidation and hydrolysis. [15] Even if the biodegradability of terpenoids can be considered as a *pro*, given the absence of residues on harvested products and on the environment, on the other side it reduces their efficacy against insect pests and fungi, caused by the low persistence of pure active principles on crops. [41] Another problem regarding the application of pure active principles on fields is given by the fact that EOs and their constituents are lipophilic and generally poorly soluble in water, negatively affecting the ease of distribution in fields and the absorption of the active principles by plants. [42] The third issue is that, given the phytotoxic effects of many EOs and of their constituents, their direct and indiscriminate

application on crops could yield severe plant desiccation, even to the plants to be protected, resulting in harvest losses. [43]

The solution to solve these issues is encapsulating the active principles inside a matrix which grants the isolation of the bioactive components from the external atmospheric environment. This guarantees the stability of terpenoids over time, as well as their constant release when applied to crops, minimizing the adverse effects on plant tissues. [44]

Encapsulation is defined as a process in which droplets of the bioactive oil are surrounded by a coating, or embedded in a homogeneous or heterogeneous matrix, to give small capsules with useful properties. [45] The matrix material can either be made up of a synthetic or natural polymer. The resulting size of the microparticles is in the micrometric regime (1–1000 μm). By isolating the inner core from environmental elements, microencapsulation techniques can preserve the bioactive molecules from external factors (light, heat, oxygen), preventing the autoxidation processes which would lead to the degradation of the EOs compounds. Hence, the shelf-life of said formulations can be increased. In addition, microencapsulation decreases the volatility of the inner core and promotes easier handling of the formulations (control of hygroscopicity, flowability, dispersibility and solubility). [46] Furthermore, microcapsules can achieve a controlled release of the active principles as a response to changes of the external conditions, such as pH, temperature, pressure, or humidity. [47]

There are many approaches to microencapsulate EOs and their components. Each method is selected depending on the final intended usage of the formulation. The most relevant methods are spray drying, *in situ* polymerization, extrusion, layer-by-layer coating and coacervation. [44] Several of these approaches are based on the preparation of emulsions before the encapsulation process. Emulsions consist of at least two immiscible liquids (oil phase and aqueous phase), with one phase being dispersed in the other in the form of small droplets. The bioactive compounds usually constitute the dispersed phase to be encapsulated, while the aqueous solution of the matrix material constitutes the continuous phase. Emulsifiers are often used in emulsions to prevent coalescence of phases.

Spray drying methods consist in the dispersion of the matrix material and the bioactive compounds to form an emulsion or dispersion. The resulting mixture is sprayed into a drying chamber, which has the aim of evaporating the solvent. The drying process can also modify the physical, chemical, and biological properties of the matrix material, ultimately affecting the protection degree towards the external environment. The obtained microcapsules are characterized by a high stability. [48]

In situ polymerization methods consist in using aminoplast resins as matrix materials, in particular as the monomers for the polymerization reaction which occurs in the continuous phase. Changing the pH and temperature of the solution, the matrix material precipitates, and evenly distributes and polymerizes over the surface of the emulsion droplets containing the bioactive principle. Microparticles obtained by this approach are spherical and smooth, with transparent and pressure-sensitive walls which ensure controlled diffusion. [44]

Extrusion consists in the dissolution of a hydrocolloid in which the active compounds are added. The resulting mixture is then extruded through a syringe to form droplets, which are then dripped into a hardening solution. The advantages of this approach are the mild temperatures and low-pressure conditions required, making extrusion the preferred technique for microencapsulating thermolabile active ingredients. [49]

Layer-by-layer coating approaches are typically produced through the electrostatic-assisted deposition of charged biopolymers onto a droplet of active principle which has been covered with an opposite charged emulsifier. The thickness of the coating can be tuned by modifying the number of layers. However, while this approach is simple at a laboratory scale, it presents difficulties in the scale-up process. [50]

Lastly, the coacervation approach consists in the dissolution of the polymer (relative concentration ≤10% m/V) in water, at 40–50° C, and in the presence of the dispersed bioactive ingredient. After that, the interactions between the polymeric coating and the inner oil core lead to the deposition of the former on the latter. Finally, the coating is stabilized and hardened to form stable microcapsules (*e.g.*, by lowering the temperature). Coacervation can be distinguished into two kinds: simple coacervation, in which only one polymer is used for the coating, and complex coacervation, in which two polymers with opposite charge are used (*e.g.*, positively charged chitosan and negatively charged arabic gum). In both cases, the particle size can be controlled by varying temperature, stirring speed, viscosity of the solution and concentration of the components. Emulsifiers such as soybean lecithin can be used to achieve micelle formation prior to the coating process by coacervation. [45] The advantages of the coacervation approach are a high encapsulation efficiency (>50%), a thicker coating, improved stability for the active principles against autoxidation and decreased surface oil content. [51] Nonetheless, there are a few disadvantages, such as a narrow range of pH and ionic strength in which the coacervates are stable. [44] As a matter of fact, the chitosan coacervation approach, preceded by emulsion formation with soybean lecithin, has been used to produce the terpenoids formulations studied in this thesis work. The next chapter will report the latest results obtained in the rapidly growing field of “green” microencapsulation by chitosan.

2.1.4 Lecithin-chitosan stabilized microemulsions of terpenoids

Chitosan is one of the most popular polysaccharides used as a raw matrix material to encapsulate many bioactive compounds alongside EOs, such as pharmaceutical and nutraceutical drugs, either by coacervation or other approaches. Chitosan is a linear polysaccharide consisting of randomly distributed β-(1→4)-linked D-glucosamine (**Figure 2.3.a**) and *N*-acetyl-D-glucosamine (**Figure 2.3.b**). It is a natural polymer which can be derived from deacetylation of chitin in an alkaline medium, from crustacean shells (*e.g.*, crabs or prawns), or from cell walls of fungi. [52] In an acidic environment, the amine groups of the deacetylated monomers can be protonated, resulting in a net positive charge. Its natural origin, combined with its high stability and antimicrobial properties, is among the main reasons why chitosan is an excellent candidate for obtaining a "green" and more environmentally conscious encapsulation of bioactive principles, as opposed to the encapsulation through synthetic polymers. [53]

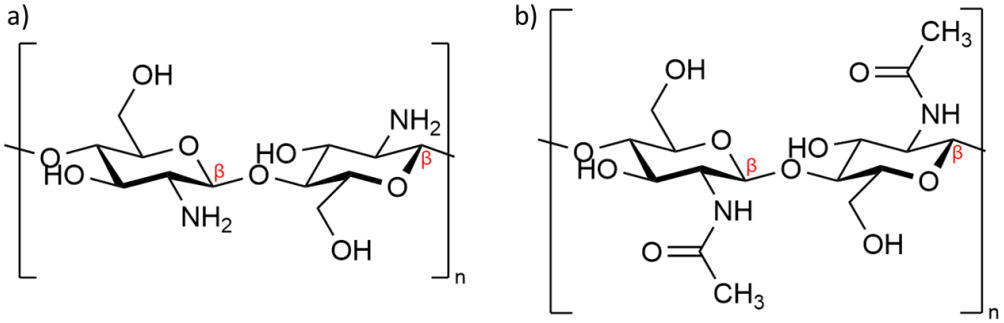

Figure 2.3. Molecular structure of the chitosan-constituting monomers. On the left (a), the deacetylated monomer is shown, whereas on the right (b) the acetylated monomer is shown.

Lecithin is a complex mixture of phospholipids (65–75%), triglycerides and small amounts of other substances. The phospholipidic content is composed mainly of phosphatidylcholine, phosphatidylethanolamine, and inositol-containing phosphatides. Other substances include triglycerides, carbohydrates, fatty acids, pigments, sterols, and sterol glycosides. It can be obtained from various natural sources, such as egg yolk, marine foods, soybeans, and milk, by a degumming process followed by an exsiccation of the extracted gums. [54,55] Nowadays, the commercially available lecithin is predominantly derived from soybean. **Figure 2.4** represents an example for the phosphatidylcholine class of molecules, a type of phospholipid which is present in lecithin.

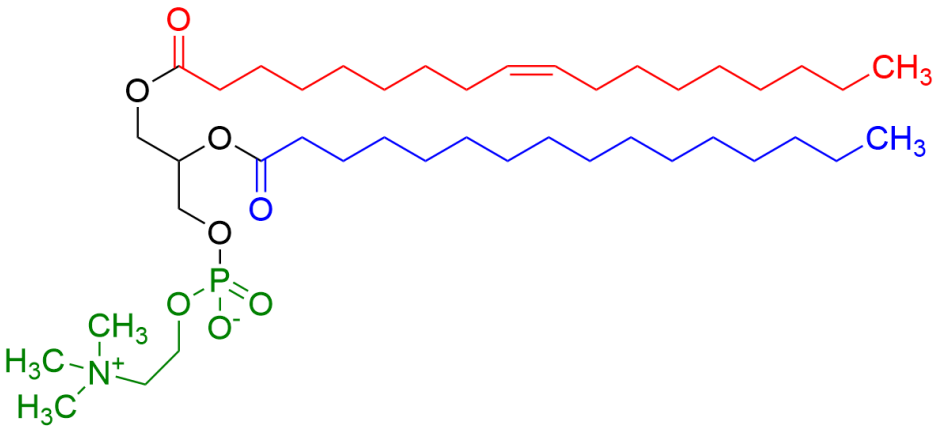

Figure 2.4. Molecular structure of 1-oleoyl-2-palmitoyl-phosphatidylcholine, as an example for the class of phosphatidylcholines, a type of phospholipid which is present in the composition of lecithin. Highlighted in red: monounsaturated fatty acid residue (oleate); in blue: saturated fatty acid residue (palmitate); in green: choline residue and phosphate group; in black: glycerol residue.

Given their amphiphilic nature, the phospholipids contained in lecithin can form liposomes, bilayer sheets, micelles, or lamellar structures in aqueous solution. As a results, soybean lecithin is mainly used as a surfactant, from the pharmaceutical to the food industry. [54] In fact, the components present in lecithin interpose themselves spontaneously between the water phase and the oil phase, so as to minimize the interfacial tension between the phases (enthalpic driving force). In addition, micelle formation is also promoted by an entropic driving force: phospholipids arranging themselves in organized, micellar-like, structures will present fewer hydration waters coordinated to them than in a configuration in which phospholipids are not assembled. Thus, the number of degrees of freedom of the system increases as a result of the loss of coordination of hydration waters, increasing entropy, and ultimately leading the system towards a lower free energy. [56] The surfactant properties of lecithin contrast the natural processes which lead to emulsion destabilization, such as gravitational separation, flocculation, coalescence, and Ostwald ripening. [57] In addition, emulsifiers such as lecithin reduce the tendency of droplet aggregation by generating repulsing electrostatic forces between micelles.

Recently, lecithin has gained popularity in the microencapsulation field. [58] In fact, given its properties of anionic emulsifier, lecithin can stabilize the emulsions obtained when mixing a bioactive principle (oil phase) in water. The non-polar hydrophobic tails point towards the interior of the micelles, where the hydrophobic bioactive principle is present, while the polar hydrophilic heads, composed of the choline residues and phosphate groups, point towards the aqueous environment.

When a cationic polymeric matrix (*e.g.*, chitosan) is added to the solution, the result is the formation of stable microbeads which encapsulate and protect the inner oily core from the

external environmental agents, as described before. The main forces driving the adsorption of the cationic biopolymer onto the surface of the anionic emulsified droplets are of electrostatic nature. **Figure 2.5** shows the schematic of a microbead obtained by coacervation, using soybean lecithin as the anionic emulsifier and chitosan as the cationic polymeric matrix material. [45]

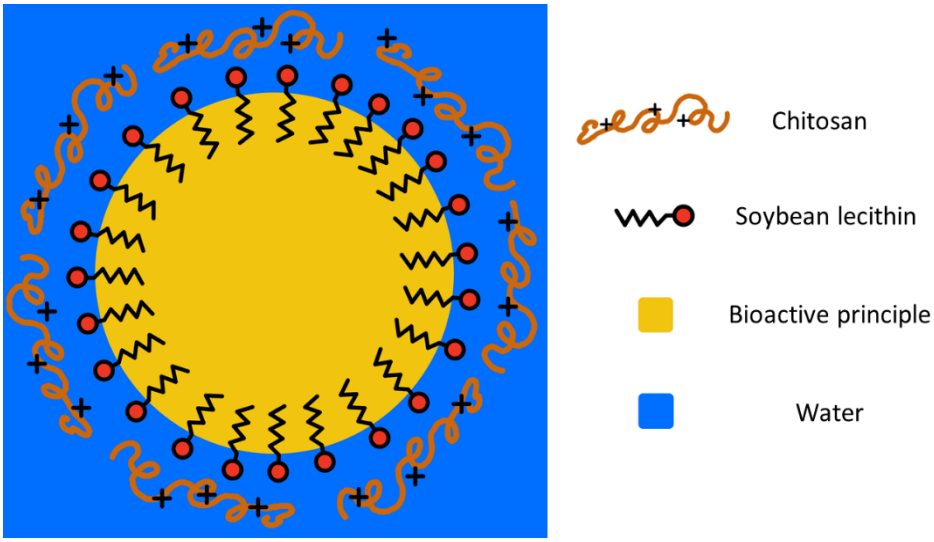

Figure 2.5. Schematic of a coacervated emulsion droplet stabilized by an emulsifier (soybean lecithin) and a natural polymer (chitosan). [45]

Few sources in the literature have reported an efficient production of chitosan-stabilized microbeads, either by coacervation or by other approaches. Mondéjar-Lòpez *et al.* described the chitosan-encapsulation of carvacrol and eugenol, yielding an improvement in stability and antimicrobial properties of these active principles. [59] However, instead of the anionic surfactant soybean lecithin, a nonionic surfactant, Tween 80 (polysorbate 80), was used. The antioxidant activity was tested by DPPH (2,2-diphenyl-1-picryl-hydrazyl-hydrate) scavenging method, in which the intensity of the violet color of an ethanolic solution of this compound is inversely proportional to the concentration of antioxidant analytes. [60] The resulting formulations appeared to have increased the antioxidant power.

Ogawa *et al.* described the production of oil-in-water emulsions stabilized by lecithin-chitosan membranes by the coacervation approach. [57] **Figure 2.6** schematizes the procedure to obtain stable chitosan-coated microbeads encapsulating a generic hydrophobic material (corn oil), to simulate the properties of other hydrophobic bioactive principles. The authors have used the anionic emulsifier lecithin to stabilize the droplets produced in the so-called *primary* emulsion. In slight acidic condition, the cationic biopolymer (chitosan) present in solution adsorbs onto the emulsified droplets thanks to electrostatic attraction between the negatively charged lecithin-stabilized surface and the protonated amines of chitosan, to form the *secondary* emulsion. The secondary emulsion showed to be more stable against flocculation and coalescence than the

emulsion stabilized with lecithin alone. Furthermore, the secondary emulsion appeared to be stable at low pH (3–5) and low ionic strength (<500 mM).

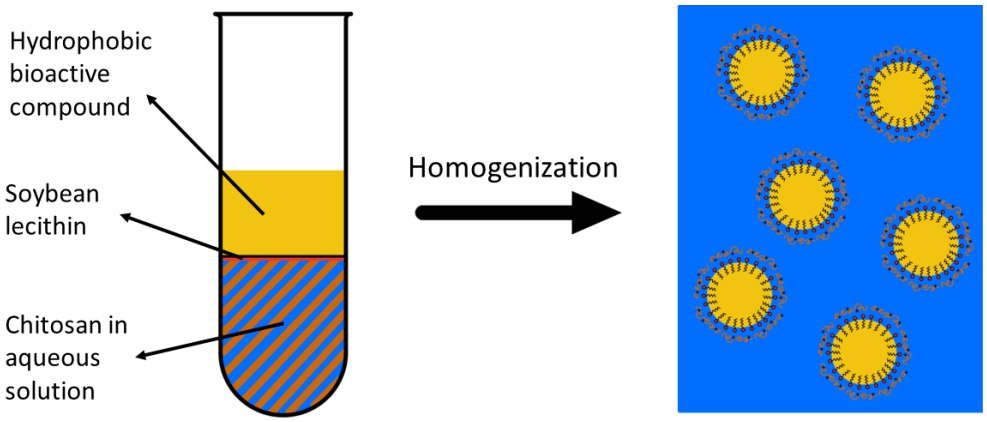

Figure 2.6. Schematization of the procedure used by Ogawa *et al.* to produce lecithin-chitosan stabilized microemulsion encapsulating corn oil. [57] The color code is the same as **Figure 2.5**.

The same authors also established the stabilities of the secondary emulsions against thermal processing, high ionic strength, and inner core lipid oxidation. [61] It has been found that lecithin-chitosan stabilized emulsions are more stable than lecithin-only stabilized emulsions after exposition at elevated temperatures (90° C). It is hypothesized that the additional chitosan layer protected the hydrophilic heads of lecithin to a certain extent from heat-induced dehydration, which in primary emulsions led to deformation of the droplets and their coalescence. The stability of secondary emulsions to freeze-thaw cycles (-10° C for 22 h, followed by 30° C for 2 h) did not change much from the stability of primary emulsions, resulting ultimately in a >10-fold increase in mean particle size for both the emulsions. It has been suggested that these results depended on the rapprochement forced between droplets, caused by the icing of increasing volumes of water. Also, the freezing of water increases the ionic strength of the non-frozen portion of water. High ionic strength induces the aggregation of droplets. The authors suggested that the addition of cryoprotectants in solution may help to extend the temperature range in which especially secondary emulsions are stable. As mentioned above, an increasing ionic strength of the solution corresponded to an increasing degree of droplet aggregation. However, the secondary emulsion remained stable in a far wider ionic strength range (0–500 mM, $CaCl_2$) rather than the primary emulsion (0–3 mM, $CaCl_2$). The thicker secondary emulsion coating manages to support more charges present in solution before reaching a neutral condition that leads to the cancellation of repulsion between droplets and eventually to aggregation. Finally, as far as the oxidation of the core compounds is concerned, the authors evaluated the peroxide concentration of the formulations stored at room temperature. During the first three weeks, the incremental rates of peroxides were similar for both the primary and secondary emulsions. However, after that, the

oxidation proceeded significantly more rapidly in the primary emulsion. Given that the binding of Fe(II) or Fe(III) ions to the surface of negatively charged droplets accelerates lipid oxidation by bringing closer the catalysts to the substrate, [62] it is possible that a catalytic amount of endogenous iron ions bound to the lecithin layer led to a similar rate of oxidation in both emulsions. Nevertheless, the magnitude of oxidation in the secondary emulsion was much smaller than that of the primary emulsion after the initial three weeks.

Lastly, Carvalho *et al.* produced lecithin-chitosan coated microparticles which encapsulated green coffee oil, a sun protective bioactive agent, through the electrostatic layer-by-layer approach followed by spray drying. [63] Thanks to the presence of chitosan, the microparticles demonstrated greater stability against coalescence than the lecithin-only stabilized emulsion. This was attributed to the heterogeneity of the polyelectrolyte composition of chitosan: in particular, the more acetylated monomers are more hydrophobic, while the others are more hydrophilic. This property results in a greater stabilizing action of the chitosan because it more easily adsorbs at the oil/water interface of the droplets, protecting them from coalescence. The encapsulation efficiency of the microparticles was high (~83%). They also set out to evaluate the stabilizing action of chitosan against oxidation of the compounds in the inner core, comparing it with emulsion stabilized only by lecithin. *Rancimat* was the method chosen to evaluate the oxidation degree. This method evaluates the production of volatile oxidation products as a result of forced passage of air within the formulation. These products are then solvated by the measuring solution (distilled water), whose electrical conductivity increases proportionally to the amounts of solvated products. The longer the induction time during which the electrical signal arises, the greater the stability of the formulation tested against oxidation. [64] The authors found that the oxidation stability of lecithin-chitosan encapsulated green coffee oil improved by a ~10-fold when compared to non-encapsulated green coffee oil (from 2.26 h to 26.75 h), confirming a significant improvement of stability against oxidation brought by encapsulating the bioactive principle with chitosan. Regarding the sun protection factor (SPF) of green coffee oil, it has been found that encapsulating the bioactive agent in lecithin-chitosan coated microparticles had resulted in a slight increase in the photoprotective power of the formulation (from 2.1 to 2.5 %SPF) if the microparticles were fortified with an additional layer of wall material (corn syrup). Specifically, the resulting formulation was found to have effectively absorbed light in the UV-B portion of the spectrum (280–315 nm). [63,65]

To maximize the photoprotection of the active principles to be encapsulated in lecithin-chitosan microbeads, the photoprotective action of gold nanoparticles was considered in this

thesis project. Current knowledge on the photoprotection contributed by this colloid is presented in the next chapter.

2.1.5 Gold nanoparticles for photoprotection enhancement

Thanks to their light absorption and scattering capabilities, gold nanoparticles (AuNPs) are an excellent candidate to be used in photoprotection. These properties, together with their biocompatible nature, low toxicity, and possibility of using ecofriendly production methods, make AuNPs attracting compounds in the formulation of cosmetic products with sun protective properties. [66] Theoretically, they can also be used to protect photolabile terpenoid formulations, by means of a similar principle of action.

Borase *et al.* studied the %SPF enhancement on sunscreen formulations apported by the addition of AuNPs. [67] They used plant latex metabolites as reducing agents as well as capping agents to stabilize AuNPs. Their nanoparticles manifested the characteristic surface plasmon resonance (SPR) broad absorption band centered at 550 nm. Additional absorption peaks found in the 310–330 nm range and were attributed to chlorine-gold bonds (from the $HAuCl_4$ used to produce the NPs) and to plant latex residues. The authors found a ~10-fold increase in the sun protection ability (from 2.4 to 24.1 %SPF) of sunscreens fortified with a small amount of AuNPs (2 to 4% w/w). They justified the increase in SPF by the reflection and scattering properties of UV radiation by AuNPs.

Rizzi *et al.* used the *Helix aspersa* Muller snail secretion (SS) as reducing and stabilizing agents for the bottom-up synthesis of AuNPs, whose photostability has then been tested. [68] The theoretical SPF of the resulting formulation was calculated to be in the range of 1 to 12. This is due to both the large absorption of SS in the UV-A and B range (280–400 nm) and the action of the metal core of the AuNPs acting as a physical sunscreen (inorganic diffuser/reflector). By increasing the colloid concentration, a corresponding increase in the %SPF value, up to 12, was observed.

The same authors described a method to produce a AuNP/chitosan/ellagic acid self-assembly and reported its antioxidant and sun protection properties. [69] The produced AuNP/chitosan assembly, without the functional ingredient, was found to be temperature resistant up to 70° C, indicating high thermal stability. Furthermore, the system turned out to be photostable after its irradiation with a sun simulator lamp, fact that is evident from the absorption spectra which showed no change in the intensities and shape of the peaks after degradation. However, to obtain

a real improvement of the sun protecting factor of the AuNP/chitosan assembly (~3 %SPF), the functional ingredient (ellagic acid) had to be added to the assembly, raising the %SPF to 20.

These results, although indicating an excellent action of AuNPs as inorganic sun filters, nevertheless seem to suggest that to achieve a high %SPF value it is advisable to take advantage of the synergistic action of chromophore molecules, capable of an efficient absorption in the UV-A and B light range as well.

Despite few examples were found in specialized literature about AuNPs as a photoprotection system in cosmetics, there is a clear lack regarding the application of this colloid to agricultural-directed formulations. In this thesis, sophisticated Au nanostructures are implemented along this latter direction.

2.2 Raman spectroscopy

Raman spectroscopy is a vibrational spectroscopic technique, therefore widely used to resolve complex mixtures by means of the fingerprint vibrational modes of their components. Raman spectroscopy is based upon the inelastic scattering of the electromagnetic radiation from particles, or molecules, whose size is somehow comparable with the wavelength of the incident radiation. With respect to Rayleigh's elastic scattering, the inelastic scattered radiation constitutes only a little fraction of the overall incident light, in which the scattered frequency is different from the initial, incoming, frequency. This phenomenon, at the core of the Raman spectroscopy theory, was discovered by Chandrasekhara Venkata Raman in 1928 and earned him the 1930 Nobel Prize in Physics "for his work on the scattering of light and for the discovery of the effect named after him". [70]

The next chapters will briefly report the theory and applications of this method of investigation of the matter.

2.2.1 Principles of Raman spectroscopy

When an electromagnetic radiation interacts with a sampled molecule, it may be absorbed or scattered in all directions. The absorption takes place if the energy of the incident photons corresponds to the energy gap between the ground and one of the excited states of the sample. Conversely, there is no need for such energy match for the scattering to occur. In fact, during scattering, light interacts with the molecule by polarizing the electrons cloud around the nuclei to form a short-lived, unstable, "virtual" state. So, the photon is quickly re-radiated (*i.e.*, scattered). Virtual states are not real molecular states, being that they are created by the interaction between the molecule electrons and the incident radiation. The energy of the virtual states ($E_0 = hc/\lambda_0$) is thus determined by the wavelength of the incident light source, λ_0.

If only the electron cloud is distorted when light scattering takes place, and not the spatial distribution of nucleus of the molecule, the re-radiated photons will be scattered in all possible directions with minimal frequency changes, as electrons have smaller mass than protons and neutrons. This scattering process is regarded as elastic scattering, also called Rayleigh scattering. It is the most dominant scattering process.

If nuclear motion (*i.e.*, vibrations) is induced during the scattering process, there will be an inelastic process related to the coupling of the induced polarization with the vibrational modes, that eventually drives to a difference between the energy of the scattered photon with respect to the incident one. This is Raman scattering, and it is an inherently a weak process: only one in 10^6–10^8 scattered photons undergo this phenomenon. [71]

Although the classical theory of Raman scattering cannot possibly deal with all the aspects best figured by the quantum theory, it provides a useful insight into some aspects of such effect, in particular the selection rules and the frequency dependance of scattering.

Along the next dissertation, all physical entities, naturally vectorial, are going to be considered as their modulus. It begins by introducing the frequency-dependent linear induced electric dipole μ^{ind}:

$$\mu^{ind} = \boldsymbol{\alpha} \cdot E \qquad \textbf{(2.1)}$$

where E is the electric field of the incident, plane wave, monochromatic radiation of frequency ω_0, and $\boldsymbol{\alpha}$ is the polarizability tensor of the molecule. The polarizability tensor is a function of the molecular vibrations, so that of the nuclear coordinates of the molecule. In other words, the polarizability tensor indicates how, and to what extent, the molecular electronic density will be distorted when influenced by an incoming electromagnetic field. To obtain the frequency dependance of the induced electric dipole μ^{ind}, we shall introduce the frequency dependance of both E and $\boldsymbol{\alpha}$ into **Eq. 2.1**.

A hypothetical molecule is assumed, which is free to vibrate but not to rotate, so that the nuclei may oscillate about their equilibrium positions. As a result, each polarizability tensor element ($\alpha_{i,j}$, where the indexes i and j represent the rows and columns of the tensor matrix of rank 2, respectively) can be expanded in a Taylor series with respect to normal coordinates of vibration Q_k and Q_l, each associated with the molecular vibrational frequencies ω_k and ω_l:

$$\alpha_{i,j} = (\alpha_{i,j})_0 + \sum_k \left(\frac{\partial \alpha_{i,j}}{\partial Q_k}\right)_0 Q_k + \frac{1}{2}\sum_{k,l}\left(\frac{\partial^2 \alpha_{i,j}}{\partial Q_k \partial Q_l}\right)_0 Q_k Q_l \ldots \qquad \textbf{(2.2)}$$

where $(\alpha_{i,j})_0$ is the value of $\alpha_{i,j}$ at the equilibrium configuration. If the electrical harmonic approximation is considered, the terms which involve powers of Q higher than the first can be neglected. By fixing our attention on only one vibrational mode, Q_k, **Eq. 2.2** thus becomes:

$$\boldsymbol{\alpha} = \boldsymbol{\alpha}_0 + \left(\frac{\partial \boldsymbol{\alpha}}{\partial Q_k}\right)_0 Q_k = \boldsymbol{\alpha}_0 + \boldsymbol{\alpha}' Q_k \qquad \textbf{(2.3)}$$

where $\boldsymbol{\alpha}$ is the tensor with components $\alpha_{i,j}$, $\boldsymbol{\alpha_0}$ is the polarizability tensor at equilibrium, $\boldsymbol{\alpha'}$ is the tensor ("derived polarizability tensor") whose components are first-order partial derivatives of polarizability with respect to normal coordinate Q_k. In other words, both terms of **Eq. 2.3** represent the perturbed molecular system, with the second being specifically modulated by molecular vibrations.

The frequency dependence of the normal vibrational coordinates Q, and of the electric field E, can be expressed classically as:

$$Q_k = Q_{k_0} cos\,(\omega_k t) \qquad \textbf{(2.4)}$$

where Q_{k_0} is the normal coordinate amplitude. **Equation 2.5** gives the frequency dependance of *E*:

$$E = E_0 cos\,(\omega_0 t) \qquad \textbf{(2.5)}$$

The frequency-dependent forms of $\boldsymbol{\alpha}$ (**Eq. 2.3**) becomes explicit by substituting Q_k with **Eq. 2.4**. One can now rewrite **Eq. 2.1**, with the expression of ***E*** by **Eq. 2.5**, and have a look at the frequency dependency of the induced electrical dipole μ^{ind}:

$$\mu^{ind} = \left[\boldsymbol{\alpha}_0 + \boldsymbol{\alpha}' Q_{k_0} cos\,(\omega_k t)\right] \cdot E_0 cos\,(\omega_0 t) \qquad \textbf{(2.6)}$$

Carrying out the products and using a trigonometric identity, one can obtain:

$$\begin{aligned} \mu^{ind} &= \boldsymbol{\alpha}_0 E_0\, cos(\omega_0 t) + \boldsymbol{\alpha}' Q_{k_0} E_0\, cos(\omega_0 t)\, cos(\omega_k t) \\ &= \boldsymbol{\alpha}_0 E_0\, cos(\omega_0 t) + \frac{1}{2}\boldsymbol{\alpha}' Q_{k_0} E_0 \{\cos\left[(\omega_k + \omega_0)t\right] + \cos\left[(\omega_k - \omega_0)t\right]\} \end{aligned} \qquad \textbf{(2.7)}$$

which can be rewritten in a simpler form as:

$$\mu^{ind} = \mu^{ind}(\omega_0) + \mu^{ind}(\omega_0 - \omega_k) + \mu^{ind}(\omega_0 + \omega_k) \qquad \textbf{(2.8)}$$

where $\mu^{ind}(\omega_0)$ represents the Rayleigh scattering contribution, in which electric dipole oscillates at the same frequency as the incident electric field, $\mu^{ind}(\omega_0 - \omega_k)$ and $\mu^{ind}(\omega_0 + \omega_k)$ represent the Raman scattering contributions, named Stokes and anti-Stokes respectively.

The energy levels diagram helps to visualize the concept behind the difference between Stokes and anti-Stokes Raman scattering (**Figure 2.7**).

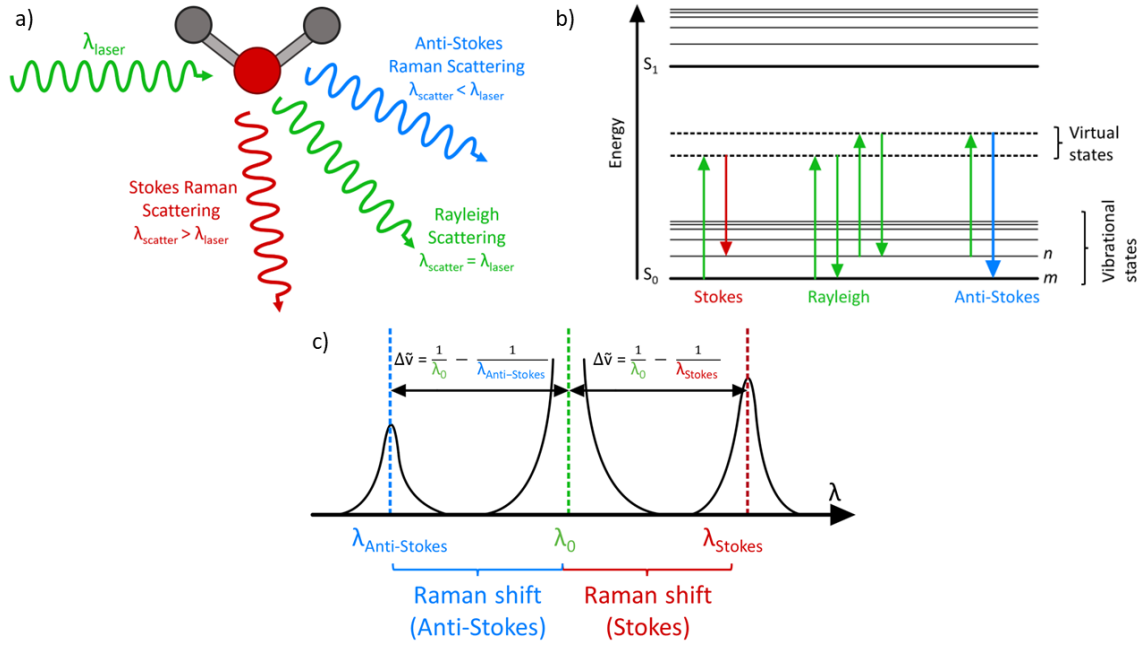

Figure 2.7. a) Visualization of the electromagnetic radiation interacting with the sample molecule. Elastic scattering (Rayleigh) is shown in green, inelastic scattering is shown in red (Stokes) and blue (anti-Stokes). [72] b) Visualization of the vibrational energy levels of a generic molecule. The different types of transitions are depicted using the same

color code. c) Visualization of the hypothetical Raman peaks for the generic molecule under investigation. Note the higher intensity of Stokes scattering than anti-Stokes scattering. This is due to the larger population of the ground vibrational state at room temperature, compared with the excited vibrational levels.

The Raman scattering which occurs from the ground vibrational state *m* (**Figure 2.7.b**) leads to the absorption of energy from the incident photon by the molecule, which is then promoted to the higher energy excited vibrational state *n*, trough the so-called Stokes Raman scattering. The resulting scattered photon will possess less energy than the incident one, translating into a greater wavelength ($\lambda_{Stokes} > \lambda_0$).

On the other hand, anti-Stokes Raman scattering takes place when the molecule, thanks to thermal agitation, lies in a vibrational excited state, such as *n* (**Figure 2.7.b**). Scattering from these excited states to the ground state *m* involves a transfer of energy from the molecule to the scattered photon. The resulting scattered photon will possess more energy than the incident one, translating into a smaller wavelength ($\lambda_{anti\text{-}Stokes} < \lambda_0$).

The intensity of the anti-Stokes process is smaller than the intensity of the Stokes one (**Figure 2.7.c**), because the relative intensities depend on the populations of the various vibrational states. Most molecules at room temperature populate the ground vibrational state. Therefore, the vast majority of Raman scattering will be of the Stokes type. This can be deduced from a reformulation of the Boltzmann equation (**Equation 2.9**), where N_n is the population of the excited vibrational state *n*, N_m is the population of the ground state *m*, *g* is the degeneracy of *n* and *m* levels, $E_n - E_m$ is the energy difference between states, k_B is the Boltzmann's constant and *T* is the temperature of the system: [71]

$$\frac{N_n}{N_m} = \frac{g_n}{g_m} exp\left[\frac{-(E_n - E_m)}{k_B T}\right] \qquad \textbf{(2.9)}$$

We can deduct that $N_m > N_n$, given the negative exponential and the fact that $E_n > E_m$. If the temperature is raised, the behavior of the negative exponential brings the value of the population ratio more and more towards unity, increasing the population of state *n*, and ultimately allowing inelastic anti-Stokes scattering phenomena to increase in frequency.

Raman spectra are recorded by evaluating the energy difference between the incident photons and the scattered ones. This is obtained by subtracting the scattered energy from the laser energy, ultimately giving the difference in energy corresponding to the ground and excited vibrational states (*e.g.*, *n* and *m* in **Figure 2.7.b**), *i.e.,* the Raman shift (expressed in cm^{-1}). **Equation 2.10**, where $\Delta\tilde{\nu}_{Raman\ shift}$ is the Raman shift expressed in cm^{-1}, $\tilde{\nu}_{excitation}$ is the excitation light wavenumber and $\tilde{\nu}_{scattered}$ is the scattered light wavenumber, rationalizes this concept.

$$\Delta\tilde{\nu}_{Raman\ shift} = \tilde{\nu}_{excitation} - \tilde{\nu}_{scattered} \qquad \textbf{(2.10)}$$

The Raman spectra are obtained by plotting the Raman shifts on the *x*-axis and the intensities (*i.e.*, Raman photon counts) on the *y*-axis. Peaks in Raman spectra are thus due to the vibrational modes of the sample.

Another fundamental aspect, evident indeed from **Eq. 2.7**, is about the necessary condition for having Raman active vibrational modes at frequency ω_k, namely that $\boldsymbol{\alpha'}$ been non-zero. That is to say:

$$\boldsymbol{\alpha}' = \left(\frac{\partial \boldsymbol{\alpha}}{\partial Q_k}\right)_0 \neq 0 \qquad \textbf{(2.11)}$$

or, in other words, a change in the polarizability with respect to the vibrational coordinate is necessary.

As another important aspect, most intense Raman signals come from molecules with a high polarizability, which possess big and easily deformable electron density clouds. Also, symmetric vibrations cause the greatest changes in the electron density, hence giving high intensity Raman signals. When compared to IR spectroscopy, one can observe that the selection rules are different: in fact, IR active signals are observable only if there is a change in the molecule permanent dipole moment due to the vibrational mode. Also, asymmetric vibrations give the most intense IR signals. The difference in selection rules makes Raman and IR complementary techniques. Another important difference is brought by the so-called "mutual exclusion rule", involving centrosymmetric molecules. For this class of molecules, the vibrations can either be Raman active or IR active, not both. [73]

Other key differences between Raman and IR spectroscopies include the increased spatial resolution in micro-spectroscopic experiments and the absence of interference due to water and glass for the Raman technique. The increased spatial resolution is ascribable to the use of lasers with a wavelength in the visible range, since the spatial resolution is directly proportional to the incident wavelength, as stated by the Rayleigh criterion: [74]

$$r = \frac{0.61 \cdot \lambda}{NA} \qquad \textbf{(2.12)}$$

where *r* is the minimum distance at which the points can be distinguished as individuals and *NA* is the numerical aperture of the lens. The absence of interference from water and glass is attributable to the fact that the O-H group is a weak Raman scatterer. As a result, Raman spectra from aqueous solutions can be easily acquired, unlike in IR spectroscopy.

The unique characteristics of the Raman technique, together with the technology connected to the micro-Raman instrumentation and the better spatial resolution compared to the IR technique, allow the acquisition of sequential spectra along the points of a 2D surface or even

forming a 3D volume at microscale resolution. The spectra collected in this way are analyzed with statistical methods, as will be shown later, and the use of false-colored scales thus allows a quick and intuitive interpretation. The ultimate purpose of micro-Raman maps is to locate the contributions of the different chemical compounds on the sample. **Figure 2.8** shows an example of 2D Raman maps acquired to study nanoparticles (NP) uptake in human dermal fibroblasts (HDF). [75]

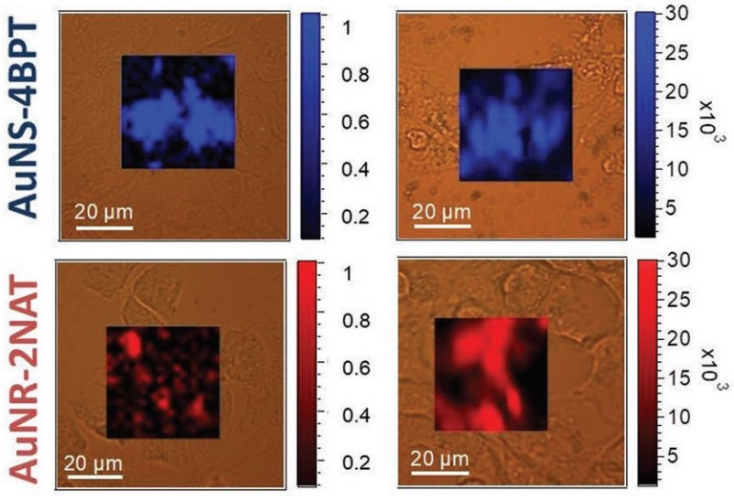

Figure 2.8. Cell viability and NP uptake in HDF cells. Brightfield optical images overlaid with colored maps of HDF containing Au nanostars functionalized with biphenyl-4-thiol (blue), and Au nanorods functionalized with 2-naphthalenethiol (red), expressing either anionic (left) or cationic (right) surface charges depending on the nanoparticle functionalization. [75]

However, Raman spectroscopy is not devoid of disadvantages. The main one is the low probability of photons to be Raman scattered (1 in 10^6–10^8). This issue may be solved by means of high-power densities that can be delivered to very small samples thanks to modern lasers. However, this solution can also determine a higher probability of sample degradation, precisely because of the power of the laser. In addition, some molecule may give fluorescence, masking Raman peaks.

The discovery of the SERS effect helped to overcome some of the problems of the Raman technique, as the next chapter will explain.

2.2.2 The SERS effect

Surface-enhanced Raman scattering (SERS) is an effect which gives an enhancement of up to 10^6 in far field Raman scattering signals, and for this reason is a valuable effect to be exploited to increase the sensitivity of the technique. It is often observed when the Raman active molecule is adsorbed or chemically bonded to plasmonic materials, namely metal surfaces or nanoparticles supporting the so-called localized surface plasmon resonances (LSPR). SERS was discovered in

1974 by Fleischmann *et al.*, during experiments that aimed to shed light on the adsorption of pyridines on silver surfaces. [76] The authors observed a strong enhancement of pyridine Raman signals when it was adsorbed on the roughened surface of a silver electrode but were unable to correctly explain the cause. To this day, the true nature of the SERS effect is still actively investigated. There are two main different theories of surface enhancement: the electromagnetic enhancement theory and the chemical enhancement theory. The current hypothesis is that these two effects, electromagnetic and chemical, work in synergy to give the SERS effect.

The theory of electromagnetic enhancement for SERS explains the amplification of the Raman scattering of molecules as a result of the localized plasmon resonance on the surface of metals, caused by the application of an exciting electromagnetic radiation. As a matter of fact, the surface as well as the bulk of the metal is characterized by the presence of freely moving electrons arisen from the conduction band. Electron density can expand outside of the metal surface boundaries thanks to the high mobility of the electrons and high polarizability of the metal atoms. This results in an exponential decay of the electronic potential intensity as one moves away from the metal surface (along the direction of the axis normal to the surface, *z*-axis in **Figures 2.9.a**). When an electromagnetic field is applied to the system, its interaction with the metal free electrons generates a collective oscillation across the surface. These collective oscillations are called “surface plasmons” (**Figure 2.9.a**). Surface plasmons from small uniform particles, such as metallic nanospheres, are characterized by a resonance frequency at which they absorb and scatter light most efficiently. This type of plasmons is called “localized surface plasmons” (LSP), as the relative dimensions of the particle in respect to the exciting wavelength make the whole particles subjected to a coherent oscillating induced field (**Figure 2.9.b**). The resonance frequency depends on the type of metal, as well as on the nanoparticles shape and their surrounding environment. By means of the Maxwell equations, the induced field on the metal nanoparticle accumulates at the surface, so that it also results in the amplification of the field exciting the Raman scattering of nearby molecules.

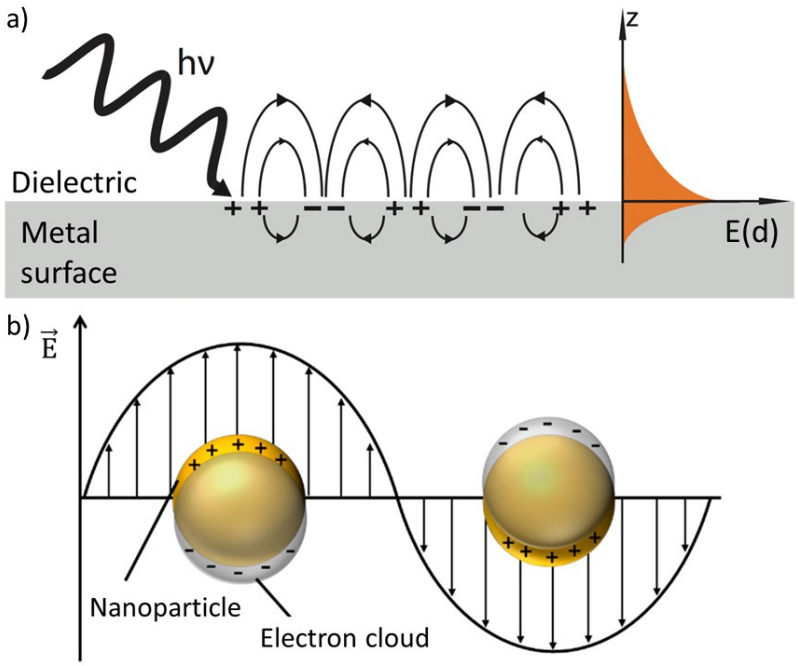

Figure 2.9. a) Schematic representation of surface plasmons propagating along a metal-dielectric interface. The exponential dependence of the electronic potential intensity (*E(d)*) on the distance away from the interface (*z* axis) is shown on the right. b) Schematic representation of localized surface plasmons resonance of a metal sphere. [77]

Electromagnetic SERS enhancement can be rationalized by using a simple model based on small metallic spheres. When an electromagnetic field is applied to a small metal sphere, the field at the surface is described by **Equation 2.13**:

$$E(d) = E_0 cos(\Theta) + g\left(\frac{r^3}{d^3}\right)E_0 cos(\Theta) \qquad \textbf{(2.13)}$$

where *E(d)* is the total electric field at the distance *d* from the sphere surface, *r* is the radius of the sphere, *Θ* is the angle describing the direction of the electric field, and *g* is a constant depending on the dielectric constant of the dielectric surrounding the metal sphere (ε_0) and on the dielectric constant of the metal sphere itself ($\varepsilon_1(\nu_L)$). **Equation 2.14** makes the constant *g* explicit:

$$g = \frac{\varepsilon_1(\nu_L) - \varepsilon_0}{\varepsilon_1(\nu_L) + 2\varepsilon_0} \qquad \textbf{(2.14)}$$

where ν_L is the frequency of the incident radiation. The value of *g* has a maximum when the denominator value is at its minimum, *i.e.*, when $\varepsilon_1(\nu_L) \approx -2\varepsilon_0$. At the frequency ν_L that verifies this equality, the excitation of the surface plasmon greatly increases the local field experienced by the molecule adsorbed on the metal surface. As one may recall from **Equation 2.1**, the module of the induced dipole is directly proportional to the module of electric field (E_0), so that to the generated Raman signals.

It can be demonstrated that the electric field is greater along the axis normal to the surface of the metal sphere rather than in the tangential direction. Hence, the greatest enhancement is observed for a molecule adsorbed on the surface of the metallic sphere and for Raman active vibrations having the associated induced dipole vector oriented perpendicular to it. Furthermore, since the enhanced field is inversely proportional to d^3, the magnitude of SERS quickly decays as the molecule moves away from the surface.

The greatest enhancement of Raman signals comes however from regions in which local fields may accumulate, *i.e.*, particles junctions or tips. These peculiar regions are commonly called "hot spots" (**Figures 2.10.a**, **2.10.b**). Thanks to constructive interference of localized surface plasmons, the enhancement of Raman signals can be as large as 15 orders of magnitude. [78] Furthermore, plasmonic surfaces that have sharp protuberances are indeed capable of developing strongly enhanced electromagnetic fields at the tip apex. As in classical physics, electric field in charged conductors accumulate at areas at higher curvature. The same happens at sharp protuberances of plasmonic materials. [79] Such materials include metal nanostars (**Figure 2.10.c**), as the ones produced as part of this thesis work.

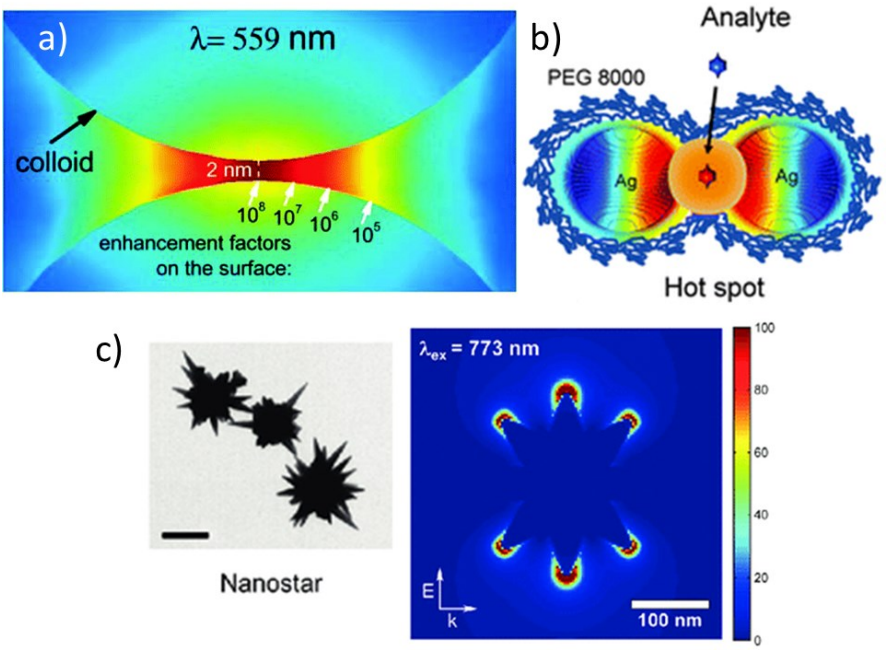

Figure 2.10. a) Electromagnetic field increase with the calculated corresponding SERS enhancement factor distribution in the nanogap (2 nm) between two gold nanoparticles at excitation wavelength of 559 nm. b) Schematic illustration of the "hot spot" formation of silver nanoparticles in the matrix of polyethylene glycol (PEG). [80] c) Simulated local field distribution around a gold nanostar excited at λ = 773 nm. The color-scale for intensity is expressed in $|E|^2$. The *E*, *k* and the corresponding arrows represent the polarization and propagation directions of the incident light. The black scale bar on the TEM image is set to 100 μm. [81]

The other theory believed to enhance the Raman effect goes under the name of chemical enhancement (or charge transfer), as it involves the formation of strong interactions between the molecule and the metal surface. The bonding makes possible to transfer charges (electrons or electron holes) from the metal to the molecule, thus influencing the molecular polarizability. Specifically, the enhancement is thought to proceed via the formation of new electronic states, arising from the charge transfer from the electron. However, it should be noted that the onset of new electronic states can also be independent of the charge transfer processes. The new states may resonate when an electromagnetic radiation is applied to the system, resulting in surface-enhanced Raman scattering phenomena. [82]

Although there is evidence for both theories, the prevailing contribution is thought to be made by the electromagnetic enhancement. Indeed, the developed electrical fields are very intense, while experimentally the chemical gain is rather small, ultimately allowing the enhanced electric fields to extend well beyond the monolayer chemically bonded to the plasmon surface. [71]

3. Materials and methods

Over the course of this chapter, the materials and tools used in this thesis will be reported, as well as the experimental and data analysis methods used to reach the conclusions presented at the end of this work.

3.1 Instruments

Micro-Raman

The micro-Raman used in this thesis is a Renishaw *InVia* model, equipped with three different laser sources and connected to a Leica DM-LM optical microscope. The two laser lines used for the characterization of the microbeads are a He-Ne, with laser emission at 633 nm and maximum power on the sample of 8.8 mW, and a diode, with laser emission at 785 nm and maximum power on the sample of 168 mW (without pinhole) and 3.8 mW (with pinhole). The simplified general scheme of the spectroscope is presented in **Figure 3.1**, together with a picture of the micro-Raman made available by the hosting research group, Nanostructures & Optics Laboratory (NOL).

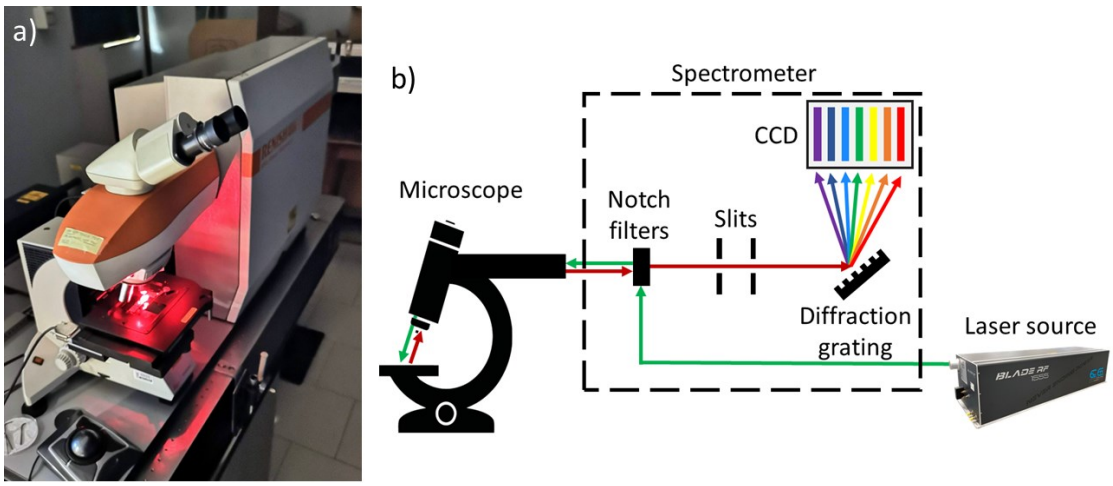

Figure 3.1. a) Picture of the micro-Raman instrument. b) Schematic diagram of the micro-Raman instrument.

The sample is initially presented to the microscope, equipped with 5x, 10x, 20x, 50x and 100x objectives, either from Leica or Olympus. Thanks to the microscope objectives, it is possible to focus the incident laser radiation on small portions of the sample, allowing for the detection of very small amounts of material despite the weakness of Raman scattering. Since light is scattered in all directions, the larger the cone of light collection, the better. For this reason, large lenses, or lenses with short focal lengths are used to cover the largest possible angle.

The spectrometer (**Figure 3.1.b**) is composed of a series of edge filters specific for each laser wavelength, entrance slits, two diffraction gratings (for visible light and NIR) and a CCD (Charge-

Coupled Device) detector. The edge filters are used to cut all light having the frequency equal or higher than the incident laser radiation, with a cut-off capacity of about 80 cm^{-1}. Entrance slits are used to improve spectral resolution by adjusting their width. Before being detected by the CCD detector, the collected scattered light is directed into a diffraction grating which separates the different frequencies of the Raman scattering. The used spectrometer has two different built-in gratings, one for the 633 nm laser line, possessing 1800 lines/mm, and the other for use with the 785 nm laser line, possessing 1200 lines/mm. The resulting energy-separated radiation is recorded by the CCD, a piece of silicon sectored into photosites (*i.e.*, pixels) which can accumulate an electric charge proportional to the intensity of the incident electromagnetic radiation. The used CCD presented 400 pixels and had dimensions of 22x22 μm. By this way, it is possible to discriminate each frequency of the scattered light and therefore construct the Raman spectrum.

Transmission electron microscopy (TEM)

Transmission electron microscopy (TEM) was used over this thesis work to better characterize Au nanostars and microbeads. It is a particular typology of microscopy, in the sense that it uses electron beams to generate an image of the sample, instead of photons. The images are thus obtained by transmitting a beam of electrons through the sample placed on a grid, usually made of a carbon thin layer over a copper or nickel grid, in a high vacuum condition. The grid, with a diameter of few millimeters, is necessary precisely because of its meshes, which allow for the passage of electrons without blocking them. By exploiting the modification of electric and magnetic fields, magnetic "lenses" drive the electrons already passed through the sample towards the detector. The magnetic lenses also widen the electron beams guaranteeing the magnification of the image. The detector can consist of a fluorescent screen, a photographic layer or a scintillator attached to a CCD.

Dense materials, such as metals, generate dark images as they better block the transmission of electrons, while less dense materials generate clear images by virtue of the greater electron transmission they allow. For this reason, only samples with nanometric thickness (up to a hundred nanometers) are suitable for TEM.

Compared to conventional light microscopies, TEM has a fundamental advantage: it has a resolution higher than 1000 times the one achievable by light microscope. High-resolution TEM can reach details of about 0.2 nm. This is because resolution is directly related to the wavelength of the radiation source, as stated by the already mentioned Rayleigh criterion (refer to **Section 2.2.1**). [83] In fact, as stated by the De Broglie equation, electrons present a characteristic wavelength of 2.2 to 3.9 pm, depending on the energy at which the microscope is operated.

Another important feature of the TEM technique is the possibility of staining low-contrast samples with heavy metal compounds (*e.g.*, uranyl acetate). Heavy metals functionalized with specific groups can interact with materials which do not possess a great TEM image contrast: this is the case of organic and carbonaceous matter, due to their low atomic density. As an example, uranyl ions combine in large quantities with phosphate groups in nucleic acids as well as phosphate and carboxyl groups on the cell surface, giving rise to enhanced contrasts in cell structures. [83]

UV-Vis and NIR Spectrophotometer

Finally, the last instrument used in this thesis work is the Agilent Technologies Cary 5000 spectrophotometer. This technique is based on the absorption of electromagnetic radiation from the sample, in a range of wavelengths from near UV (200 nm) to near IR (1300 nm). **Figure 3.2** represents the general diagram of a single beam spectrophotometer, set up so as to acquire an absorption spectrum. Specifically, light coming from the light source is directed onto a grating, which separates it into its monochromatic components. A slit selects a single monochromatic wavelength of excitation (λ_{ex}). The excitation radiation is sent to the sample, and the transmitted radiation is detected by the detector. The detector associates the intensity of transmitted radiation with the excitation wavelength which generates it. The measurement is repeated by selecting all the other excitation wavelengths by slightly turning the grating, until the entire absorption spectrum of the sample is obtained. [84]

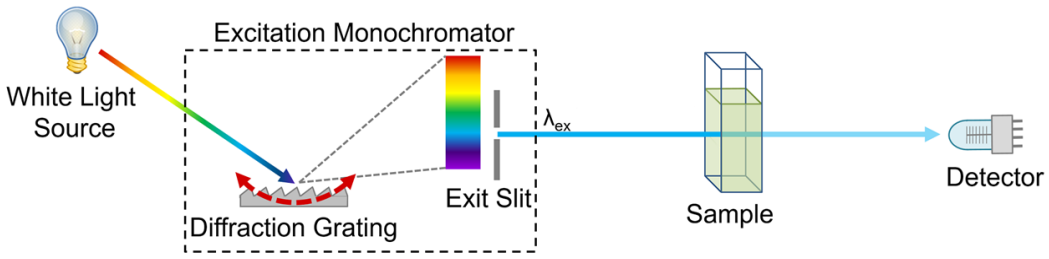

Figure 3.2. Schematic diagram of a single beam spectrophotometer, set up so as to acquire an absorption spectrum. [84]

Since the excitation range of the spectra acquired in this work also includes UV radiation, the samples were placed in quartz cuvettes, given its property of not blocking the transmission of UV light.

3.2 Experimental procedures

Having illustrated the general functioning of the characterization instruments, this chapter will illustrate the experimental procedures used for carrying out the experiments.

3.2.1 Microscope slide setup and Raman spectroscopy measurements

The setups for the acquisition of Raman spectra of microbead samples were subjected to extensive optimization, with the one described below being the optimal one. 15 μL of sample are deposited onto the microscope glass slide, which is then covered by a coverslip. The coverslip is fixed to the glass slide by a silicon-based glue. The operation must be carried out quickly enough because the glue hardens within 5 minutes after mixing its two components. The sample thus treated must remain steady for the at least 2 hours prior to the acquisition of the Raman spectra, to allow the microbeads to stabilize and remain still during the acquisition. The resulting condition has been called “wet” condition. A further expedient for sample preparation if Raman measurements are carried out with the 785 nm laser line is to deposit the sample on an adhesive aluminium sheet, glued on the glass slide. The rest of the operations remain unchanged. This expedient allows to exclude as much as possible the contributions of glass, which are particularly interfering in the spectra acquired with this laser line. **Figure 3.3** shows a picture of the glass slides as they were prepared for Raman acquisitions. In the same slide showed in the picture, the tested "dry" conditions in the absence of a coverslip, judged unsuitable for acquisitions, are visible on the right.

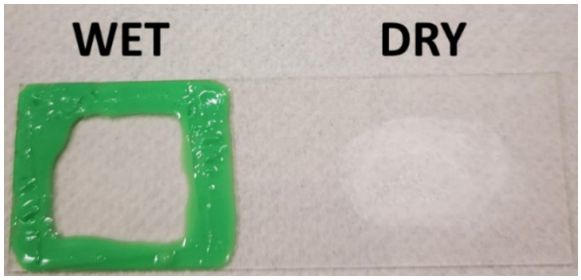

Figure 3.3. Picture of the glass slides onto which the sample has been deposited, both in “wet” and “dry” conditions, with the latter being unsuitable for Raman acquisitions.

The aforementioned procedures thus allow the maintenance of samples in the liquid phase, which would otherwise evaporate in absence of a coverslip. The maintenance of the liquid phase is considered essential because it ensures the maintenance of the spherical morphology of microbeads, especially fundamental for 3D Raman maps acquisitions. In addition, several tests were performed on the minimum amount of rest time required to reach the quiescent condition

of the microbeads during Raman acquisition. Two hours were judged sufficient based on the superimposition of the microscope pictures of the samples before and after the acquisitions.

Together with the best conditions for sample preparation, the instrumental setup for Raman maps and spectra acquisition was optimized as well, as reported in **Table 3.1**.

Table 3.1. Optimal Raman acquisition conditions used for each different experiment carried out during this thesis work.

Type of acquisition	Instrumental condition	633 nm line	785 nm line
Single spectra	Optical zoom	Leica NPlan L 100x/0.75	Leica NPlan L 100x/0.75
	Laser power (%)	50–100	1–10
	Acquisition time (s)	10	10
	Accumulations	3–5	3–5
	Confocality	Low	Low
	Pinhole (if using 785)	/	OUT
	Raman shift window (cm^{-1})	150–3200	150–3200
2D maps	Optical zoom	Leica NPlan L 100x/0.75	Leica NPlan L 100x/0.75
	Laser power	10–50	1–50
	Acquisition time	5	5
	Accumulations	3	3
	Confocality	Low	Low
	Pinhole (if using 785)	/	IN
	Grating mode	Static	Static
3D maps	Optical zoom	Leica NPlan L 100x/0.75	Leica NPlan L 100x/0.75
	Laser power	10	5
	Acquisition time	5	5
	Accumulations	2	2
	Confocality	High	High
	Pinhole (if using 785)	/	IN
	Grating mode	Static	Static

3.2.2 Synthesis and functionalization of Au nanostars

The following materials (**Table 3.2**) were purchased and supplied by the hosting research group, Nanostructures & Optics Laboratory (NOL).

Table 3.2. List of the different materials used to synthesize AuNSs capped with chitosan and Nile blue A.

Substance	CAS number	Molar weight (g/mol)	Volume used (μL)	Concentration	Moles (mol)
$HAuCl_4$	16903-35-8	339.79	50	30 mM	$1.5 \cdot 10^{-6}$
HCl	7647-01-0	36.46	5	1 M	$5 \cdot 10^{-6}$
$AgNO_3$	7761-88-8	169.88	50	10 mM	$5 \cdot 10^{-7}$
Ascorbic acid	50-81-7	176.13	50	100 mM	$5 \cdot 10^{-6}$

Chitosan	9012-76-4	/	1000	1 g/mL	/
Nile blue A lipoate	/	507.71	250	$4.5 \cdot 10^{-7}$ mM	$1.1 \cdot 10^{-13}$
AuNP	/	/	100	1.025 mM in [Au]	$1.025 \cdot 10^{-7}$

The procedure for the synthesis of gold nanostars capped with chitosan and the SERS reporter Nile blue A (from now on referred as "AuNS@NBSH@CHTS") is herein described. 5 mL of bi-distilled water, 50 μL of $HAuCl_4$ 30 mM and 5 μL of HCl 1 M were added into a new (or well cleaned) 10 mL vial. The solution, which appeared pale yellow, was stirred vigorously. Then, in sequence and very rapidly, the following aliquots were added to the solution:

1. 100 μL of AuNP 1.025 mM in [Au] ("seed" solution)
2. 50 μL of $AgNO_3$ 10 mM
3. 50 μL of ascorbic acid 100 mM

The solution appeared dark red after the addition of the seed solution, but it turned dark blue right after the addition of ascorbic acid. After 1 minute, 1 mL of a 1 g/mL solution of chitosan (dissolved in acidic distilled water, pH=2.75, following the research of Baginskiy *et al.*),[85] as well as 250 μL of a $4.5 \cdot 10^{-7}$ mM solution of Nile blue A lipoate, were added to the solution. No color change was further observed. The solution was left under vigorous stirring for one hour. The obtained solution was centrifuged for 10 minutes at 1500 rcf. The supernatant was discarded, and the remaining solution was diluted with distilled water up to 750 μL.

The successful synthesis of AuNS@NBSH@CHTS was evidenced by the color change of the solution from dark red to dark blue, a change that reflects the shift of the plasmon band of the "seed" AuNPs (at about 520 nm in the absorption spectrum) towards the plasmon band of AuNSs (at about 650-800 nm). This shift was also experimentally verified by the acquisition of absorption spectra of the solutions just after synthesis (refer to **Section 4.1.2**).

The amount of chitosan functionalized on AuNS during the synthesis was evaluated as follows. Two parallel syntheses were performed. The first is the one described above, where chitosan-capped AuNSs are obtained. Chitosan was added in excess in solution, to allow the maximum degree of interaction between it and the AuNSs. The second synthesis was obtained by using no capping and stabilizing agent. The AuNSs thus produced were not stable and agglomerated in a short time, in contrast to the stars stabilized with chitosan. Subsequently, the two solutions were centrifuged for a total of 30 minutes at 30 000 rcf, to separate the AuNSs and collect the solvent (hereafter referred as *supernatant*). The two supernatants were then analyzed by spectrophotometry: specifically, the absorbance of the solution at 300 nm, the maximum absorption of chitosan, was observed. The difference in absorbance at 300 nm between the two

solutions was therefore attributed to the amount of chitosan remaining after the functionalization of the nanostars (**Figure 3.4**). The last, namely the amount of chitosan functionalized on AuNSs was estimated thanks to a calibration curve of the absorbance at 300 nm against chitosan concentration (**Figure 3.5**). It was possible to determine that only 3% of the initial chitosan interacts with the AuNSs, meaning that, following the above procedure, AuNS@NBSH@CHTS at an overall content 0.04 g/mL *(i.e.*, 4 % m/v) of chitosan can be produced. This recipe was scaled up to obtain 10mL of final AuNS@NBSH@CHTS to be used in the microbeads formulation.

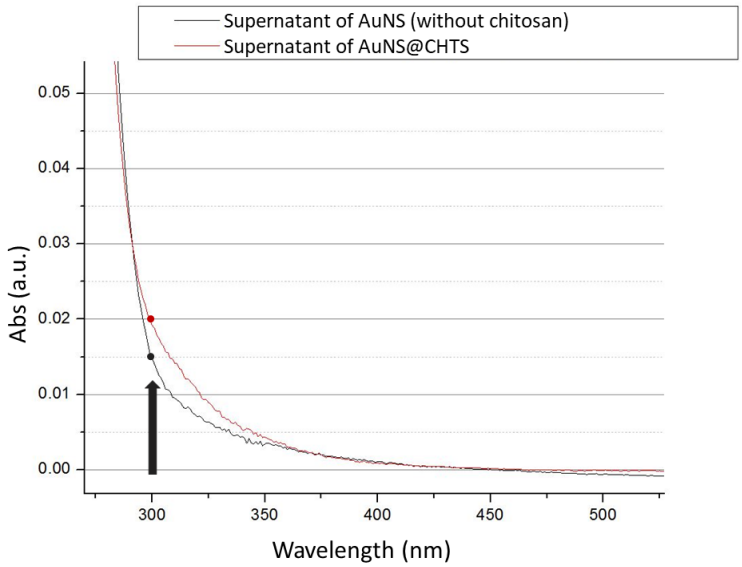

Figure 3.4. Difference in absorbance at 300 nm between the supernatants of AuNS@CHTS and AuNS without chitosan. The black arrow points to the difference in absorption between the two samples.

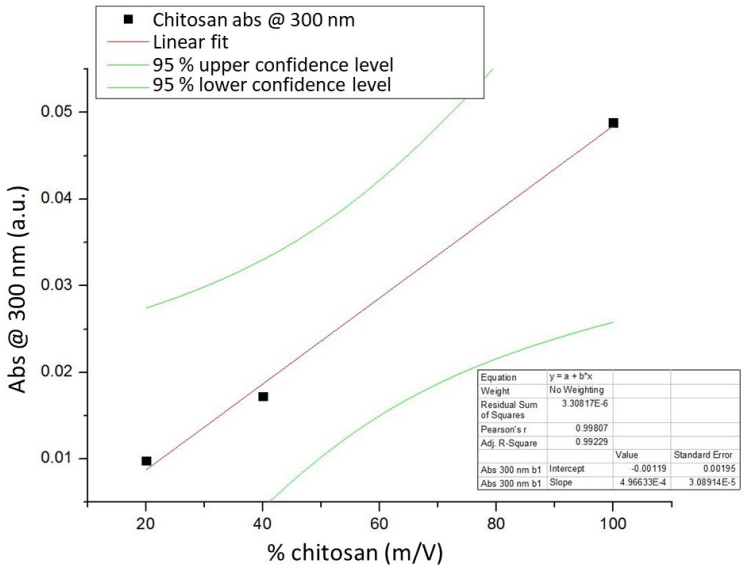

Figure 3.5. Calibration curve of the absorbance at 300 nm against chitosan concentration.

In order to validate the actual occurrence of the functionalization of the stars with chitosan through an analysis with TEM technique (refer to **Section 3.1**), AuNSs functionalized with mercaptobenzoic acid (MBA) were synthesized. The procedure is the same as that reported above for the synthesis of AuNS@NBSH@CHTS, except for the addition of 100 μL of a solution of MBA 1 mM, together with 250 μL of NaOH 0.1 M, instead of adding chitosan and Nile blue A. **Table 3.3** reports the compounds, in addition to those reported in **Table 3.2**, used for the synthesis of AuNS@MBA.

Table 3.3. List of the different materials used to synthesize AuNS@MBA, in addition those already reported in the previous table.

Substance	CAS number	Molar weight (g/mol)	Volume used (μL)	Concentration	Moles (mol)
MBA	4869-59-4	154.19	100	1 mM	$1 \cdot 10^{-7}$
NaOH	1310-73-2	40.00	250	0.1 M	$2.5 \cdot 10^{-2}$

3.2.3 Preparation of terpenoids-encapsulating formulations

Raw materials such as the terpenoids mixture (thymol/geraniol/eugenol, 2:2:1) and soybean lecithin, chitosan (4% m/V), and AMD 10 were provided by Merck, Glentham, and BASF, respectively. AuNS@NBSH@CHTS (4% m/V in chitosan) were produced at the University of Padova, starting from AuNPs, as described in the previous chapter. The formulations were produced by combining the reagents according to the quantities reported by **Table 3.4**, and then by emulsifying the obtained solutions with an IKA T25 Ultra Turrax digital disperser for 4 minutes at 12000 rpm.

Table 3.4. Quantities used to produce the formulations.

Formulation name	Oil phase	Aqueous phase	Total volume (mL)
A	Terpenoids mix (8 mL)	Soybean lecithin (2.5 mL)	20
		Distilled water (9.5 mL)	
B	Terpenoids mix (8 mL)	Chitosan (5 mL)	20
		Soybean lecithin (2.5 mL)	
		Distilled water (4.5 mL)	
C	Terpenoids mix (4 mL)	Chitosan (5 mL)	20
		Soybean lecithin (2.5 mL)	
	AMD 10 (4 mL)	Distilled water (4.5 mL)	
D	Terpenoids mix (4 mL)	AuNS@NBSH@CHTS (5 mL)	20
		Soybean lecithin (2.5 mL)	
	AMD 10 (4 mL)	Distilled water (4.5 mL)	

The thus prepared formulations were then conserved in the fridge at 4° C.

3.2.4 UV degradation setup

The lamp used for the photodegradation process of terpenoids is the Spectronics ENF-240C 4W, capable of emitting UV light with a wavelength of either 254 or 365 nm, at a power of 4 Watts. The setup for the photodegradation process consisted of placing the lamp at 4.5 cm from the quartz cuvettes containing the samples. The lamp has been set for the emission of light with a wavelength of 365 nm. Everything was placed inside a box to exclude the irradiation of the samples with ambient light. The total irradiation time of the samples was 168.0 h, *i.e.*, 1 week. The experimental setup for the photodegradation process follows the one used by de Oliveira *et al*. [33]

3.3 Data analysis of 2D/3D Raman maps: Pearson's correlation coefficient (PCC)

Raman spectra contained in 2D and 3D maps datasets were analyzed using Pearson's correlation coefficient (PCC) analysis. This multivariate statistical analysis measures the strength of the linear association between two sets of data, or, in other words, how closely the points lie to the straight line. Specifically, it is defined as the ratio between the covariance of two variables and the product of their standard deviations, and it is indicated by letter "*R*". Essentially, it is a normalized covariance measurement and measures only linear correlations of variables, as it ignores other types of relationships and correlations. Indeed, the Pearson's correlation coefficient "*R*" ranges from -1 to +1, passing through zero. Positive values close to the unity indicate that a positive correlation exists in the dataset, while negative values close to -1 indicate a negative correlation. Correlation coefficients close to zero indicate that no linear association is present between the two variables. It is worth noting that the statistical significance of *R* is directly related to the sample size ρ. Indeed, smaller samples require the correlation coefficient to have values closer to the unity, be it positive or negative, for the linear association to be significant. Conversely, in large samples, a small *R* value may still be statistically significant, despite the linear association being weak. [86]

As far as the analysis of Raman spectra datasets is concerned, as in the case of this thesis work, the PCC is computed between each experimental spectrum from the 2D and 3D Raman map datasets and the reference spectrum of the component to be identified and located. Although, as already mentioned, the values of the Pearson coefficient *R* can assume both positive and negative values, in this case only values from 0 to 1 are considered, since only positive Raman signals have

physical significance. Given the not too large size of the dataset analyzed by PCC for the 2D and 3D Raman maps here acquired (static windows of acquisition, accounting for a Raman shift range of about 800 cm^{-1}), only values of $R \geq 0.3$ were considered as statistically significant. The same PCC analysis was performed for single spectrum experiments as well.

4. Results and discussion

4.1 Materials production and characterization by Raman means

The principal aim of this thesis work is to establish if it is possible to protect the terpenoids from UV light-induced degradation, and, if so, to what extent. In addition, the retention of the active ingredient by the microbeads has also been studied as subject of this work. Along the way to address these objectives, an extensive spectroscopic and morphological characterization of the microbeads was done by Raman spectroscopy means as a secondary task. Four different formulations of encapsulated terpenoids have been therefore produced. In particular, the components added to each formulation were though to increase the theoretical photoprotection degree, as presented in the next chapter. This has been justified by the UV-vis absorption spectrum of the compounds added in solution to produce the formulations. Gold nanostars have been used with the twofold intent of shielding the capsules by means of their broad absorption band, and to provide enhanced contrast for the morphological characterization of microbeads by advanced confocal micro-Raman imaging. The latter objective has been justified because of the SERS effect brought by said nanostars.

The idea behind the production of the formulations, as well as the choice of using gold nanostars, will be explained in detail in the following paragraphs.

4.1.1 Chitosan-encapsulated terpenoids: the experimental design

Four different formulations of encapsulated terpenoids have been designed and produced by the coacervation method (as described in **Section 2.1.3** and **3.2.3**). The increasing complexity in the composition of each formulation accounts for the hypothesis of an increasing degree of photoprotection of the terpenoids located at the core. **Figure 4.1** shows the conceptualization of the general structure of the microbeads.

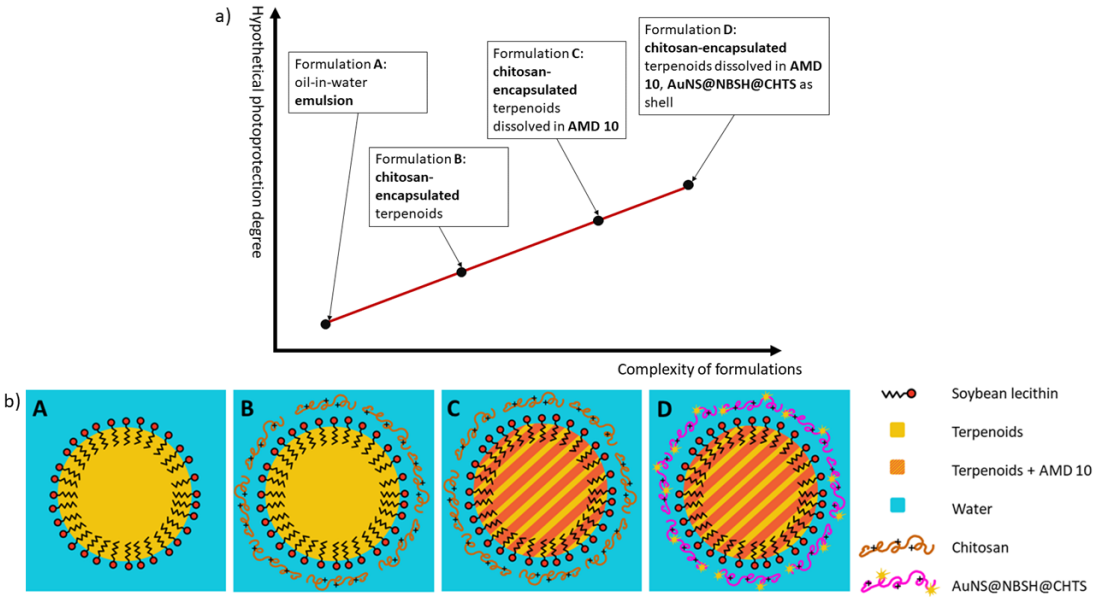

Figure 4.1. a) Conceptualization of the experimental design behind the production of the four different formulations. b) Cartoon rendition of the microbeads for each formulation produced. The drawings are not in proportion.

The increasing trend of hypothetical photoprotection should follow the addition of components that gradually cover a wider and wider range of the solar radiation spectrum (reported as reference in **Figure 4.2**). [87] The absorption spectra of all the used compounds can be seen in **Figure 4.3**. Even though the terpenoids mixture absorption maximum is located at 279 nm (so within the UV-C range from 100 to 280 nm), the use of other components ensures the theoretical protection against all UV-B (280-315 nm), UV-A (315-400nm) and visible portions of the light spectrum. [65]

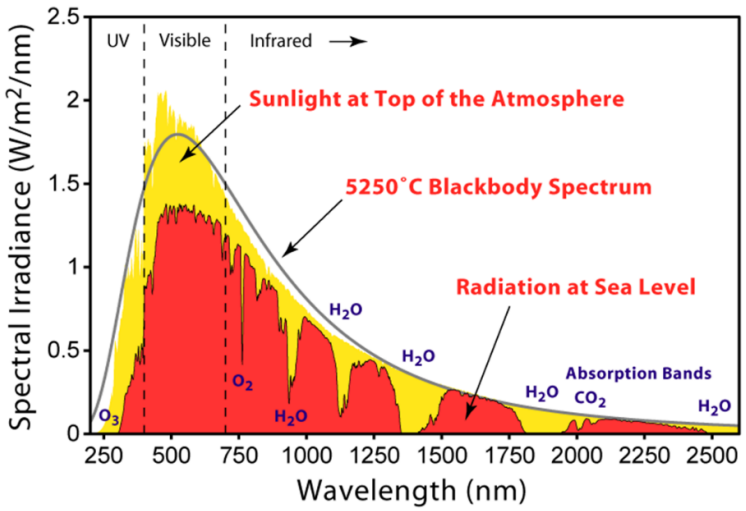

Figure 4.2. Solar radiation spectrum as a function of wavelength. In yellow, the radiation present at the top of the atmosphere. In red, the radiation at sea level. In grey, the theoretical blackbody radiation spectrum calculated at 5250° C. [87]

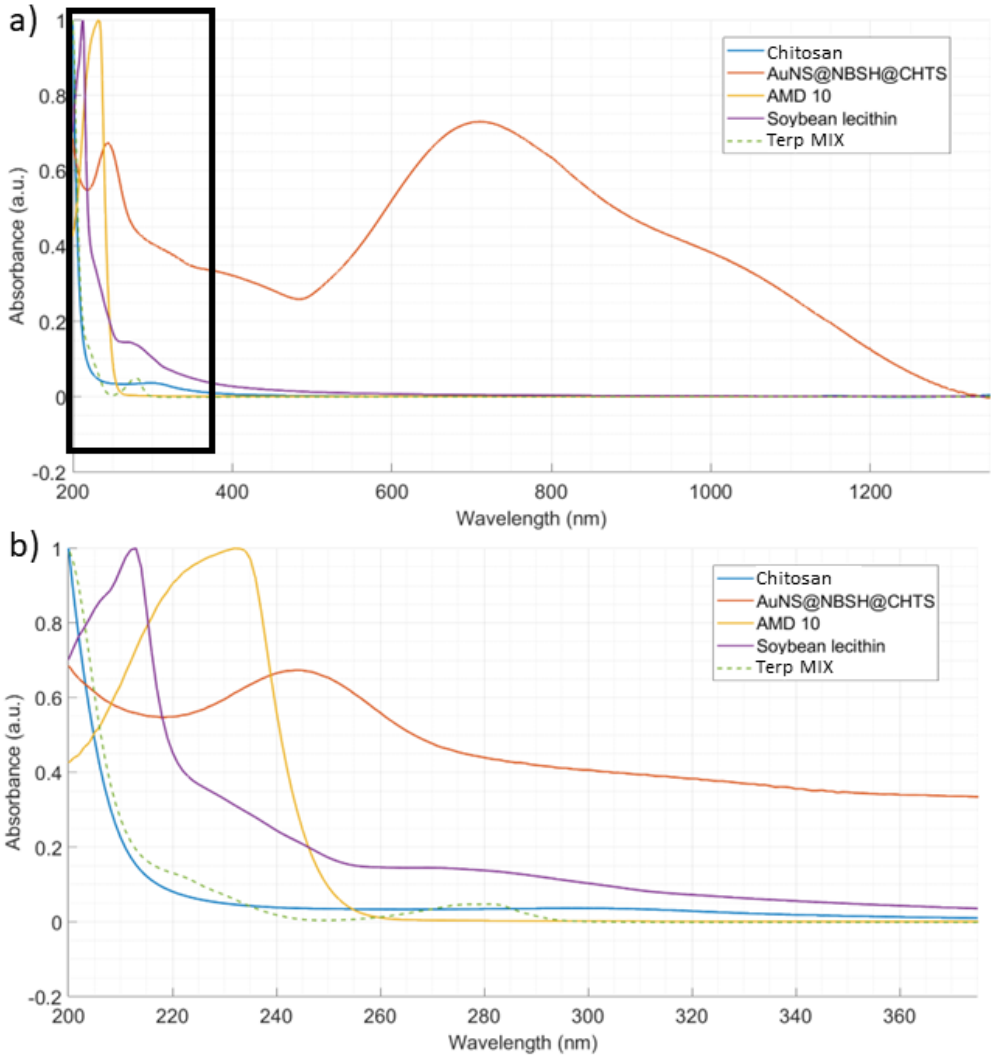

Figure 4.3. a) UV-vis spectra of all the components used to produce the formulations. The black rectangle highlights the area which is enlarged in section (b). The terpenoids mixture UV-vis spectrum is displayed by a green, dashed curve. b) Enlargement of the UV-vis spectrum shown in section (a).

Table 4.1 reports the absorption maxima of each component used to produce the encapsulated-terpenoid formulations.

Table 4.1. Absorption maxima of each component used to produce the formulations.

Component	Absorption maximum (nm)
Chitosan	300
AMD 10	232
Soybean lecithin	213
AuNS@NBSH@CHTS	710 (plasmonic band), 244 (secondary band)
Terpenoids mixture	279

While the addition of chitosan from formulation B onward makes very little absorption contributions, according to **Figure 4.3**, it does indeed contribute to the stabilization of the micelles (refer to **Section 2.1.4**). In fact, the positive charges of chitosan amine residues in an acidic environment allow effective interaction with the polar heads of soybean lecithin around the hydrophobic core of micelles, increasing their stability. The contribution of chitosan slows down the natural coalescence processes between the oil and water phase. [45] On the other hand, the addition of AMD 10 (**Figure 4.4**) from formulation C onward helps to expand the total absorption range of the formulations, adding photoprotection effects from within the core of the microbeads as well.

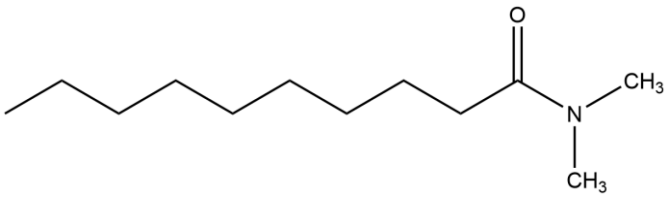

Figure 4.4. Molecular structure of AMD 10 (commercial name of *N,N*-dimethylcapramide).

Finally, AuNS@NBSH@CHTS added to formulation D offer extended photoprotection from UV to visible light, as one can observe from the absorption spectrum in **Figure 4.3**. Further details on AuNSs will be presented in the next chapter.

Optical microscopy pictures captured immediately after the production of the formulations (described in **Section 3.2.3** and in **Fig. 4.1**) are shown in **Figure 4.5.a**. The results of the size distribution analysis report an average size for the microbeads diameters of 4.5±0.3 μm for formulation A, 2.4±0.1 μm for B, 2.9±0.1 μm for C, and 4.9±0.3 μm for D (n=200; confidence interval of 95%, for all formulations). As can be seen from the results and pictures, the average size of microbeads from formulations A and D is about twice the average size of microbeads from B and C, with a relatively narrow dispersion. By **Figure 4.5.b**, the formulations appear opaque and milky white in color. With the addition of chitosan, a higher solution viscosity is observed. To be noted, the addition of Au nanostars capped with Nile blue A and chitosan results in a bluish coloration of formulation D, again accordingly to the contribution given by the AuNS plasmon bands (**Figure 4.3**).

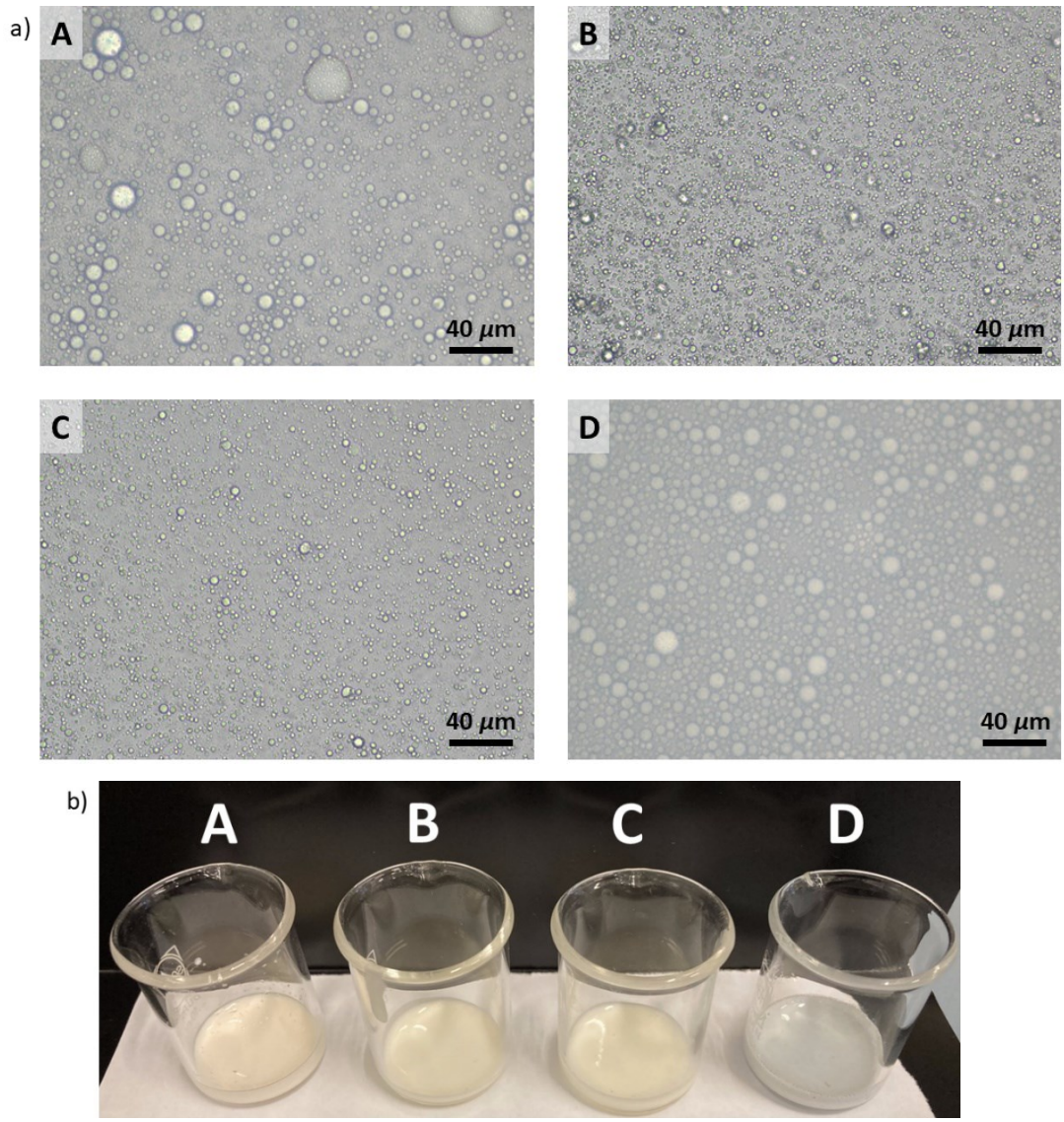

Figure 4.5. a) Pictures of formulations A, B, C and D acquired with an optical microscope, 40x optical magnification, right after their production. b) Photos of how formulations A, B, C and D look to the naked eye immediately after their preparation. To be noted the bluish coloration of formulation D, resulting from the addition of Au nanostars capped with Nile blue A.

4.1.2 Why to use AuNSs? Photoprotection and SERS effect

Au nanostars were synthetized following a silver-assisted seed-growing approach (refer to **Section 3.2.2** for details). During Au^0 deposition on the surface of Au nanoparticles (AuNPs), Ag atoms drived the anisotropic growth of tips by blocking few crystal facets on AuNPs seeds.[88] **Figure 4.6.a** shows the resulting solution of AuNSs, as well as the starting AuNPs seed solution. As far as the photoprotection is concerned, the choice of using chitosan-functionalized AuNSs is justified by their already mentioned ability to absorb light in a wide range of wavelengths, as shown by **Figure 4.6.b**. In this spectrum, the AuNSs plasmonic band is visible in the range of about 600÷850 nm, while the narrow band at about 250 nm can be ascribed to some other species used to produce the nanostars (refer to **Section 3.2.2** for details). [69] In addition, the shift in the absorption maximum, with respect to the seed spectrum of AuNPs, is clearly visible, thus attesting to the successful synthesis of AuNSs. [88] This shift is also visible to the naked eye with a change in the color of the solution, from the dark red of the seed to the dark blue of the AuNSs (**Figure 4.6.a**).

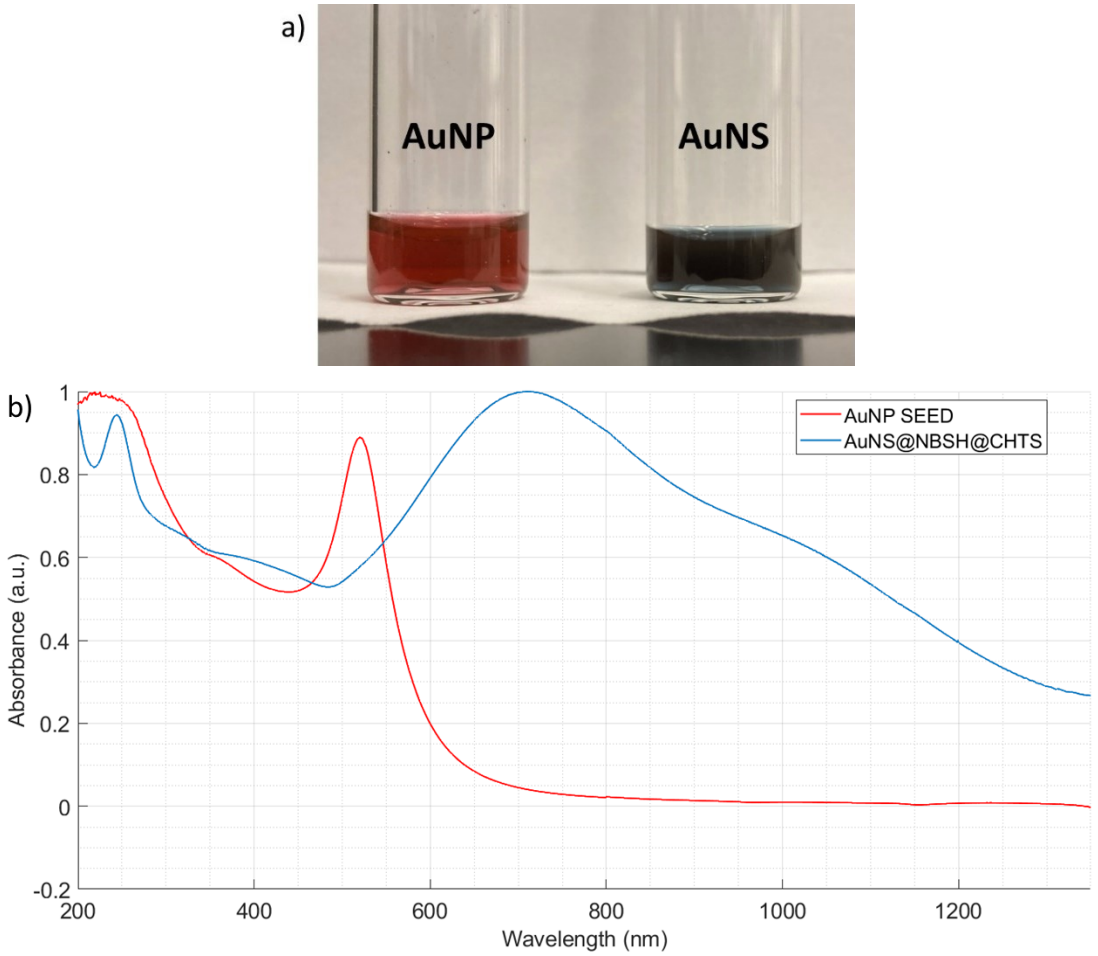

Figure 4.6. a) Picture of AuNP seed and AuNS@NBSH@CHTS solutions. b) Absorption spectra of AuNP seed and gold nanostars capped with chitosan and Nile Blue A lipoate (AuNS@NBSH@CHTS).

On the other hand, AuNSs have been used because of their Surface Enhanced Raman Scattering (SERS) effect (refer to **Section 2.2.2**). This phenomenon has been exploited to correctly locate a challenging component among the morphological structure of the microbeads, *i.e.*, chitosan. In fact, this component does not present a sufficiently high Raman cross section to be effectively detected as the outer layer of the microbeads: specifically, the intensities of the Raman peaks are too weak compared to those of the other components, so that chitosan could not be correctly localized in the presence of the other compounds added to formulations.

AuNSs have been functionalized with chitosan (referred to as "CHTS"), which acted at the same time as functionalizing and stabilizing agent for the AuNSs. [85] The functionalization occurs thanks to the chitosan amine residues, positive at acidic pH values, which strongly bind to the gold surface of the nanostars thanks to electrostatic attraction. [69,89] Thus, chitosan-functionalized AuNSs can be used to produce terpenoids-encapsulating formulations, instead of pure chitosan. This assumption is based on the fact that the dimensions of the AuNSs (~100 nm) are two orders of magnitude smaller than the microbeads present in the formulations (~10 µm), so that it may be assumed that there may be no substantial difference between using pure and AuNS-modified chitosan.

In the presence of a capping SERS reporter (Nile blue A lipoate, "NBSH"), AuNSs can enhance its Raman signals thanks to the SERS effect. The SERS reporter NBSH has been chosen based on its Raman signals, which do not interfere with the ones of the active principle of the formulations, namely the terpenoids mixture (**Figure 4.7**), as well as on its capability to strongly bind to the gold surface of nanostars.[90] **Table 4.2** resumes the main Raman peaks assignments for the SERS reporter Nile blue A. [91–93] The peak at 592 cm^{-1} was selected as diagnostic for its identification.

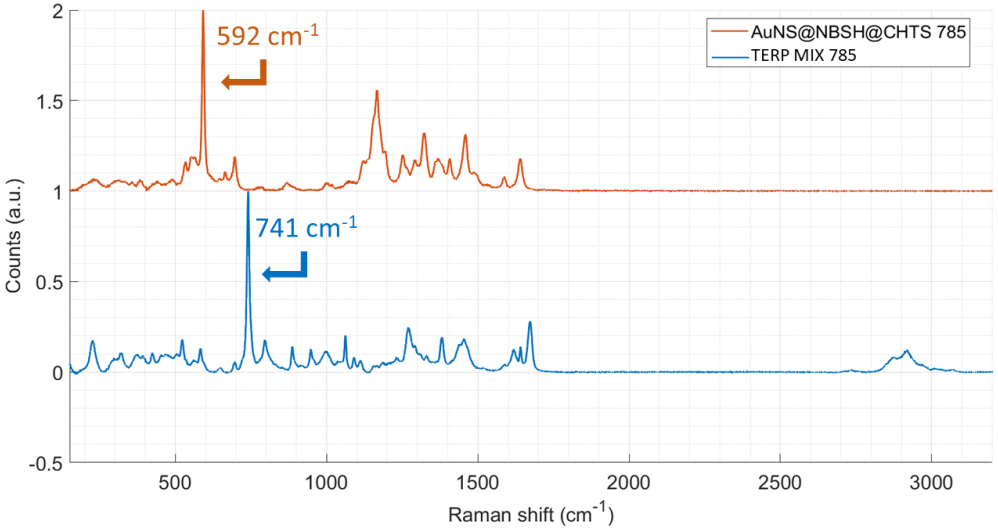

Figure 4.7. Comparison between Raman spectra of AuNS@NBSH@CHTS and of terpenes mixture, acquired by using the 785 nm laser line. The AuNSs diagnostic peak is located at 592 cm^{-1}. The terpenoids mixture diagnostic peak is located at 741 cm^{-1}.

Table 4.2. Raman peak assignments of Nile blue A, acquired by using the 785 nm laser line.

Raman shift (cm^{-1})	Intensity	Assignment
592	vs	C-C-C/C-N-C deformations [91]
1167	s	C-H bend [91]
1361	m	α(CC), β(CCH)/β(CH_3), γ(CCC)[92]
1587	w	CNH str. and bend (R-NH-CO-R)[93]
1640	vs	C=O str. (R-NH-CO-R)[93]

By these means, as will be shown in the next chapters, chitosan can be indirectly localized among the morphological structure of the microbeads by the SERS signals associated to the Nile blue A reporter, which indicates the presence of both AuNSs and chitosan. The system of Au nanostar functionalized with Nile blue A and chitosan (AuNS@NBSH@CHTS) is depicted in **Figure 4.8**.

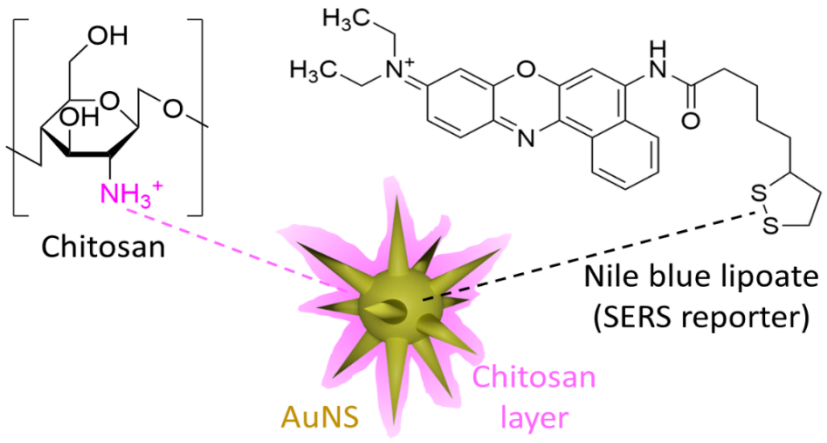

Figure 4.8. Scheme of the AuNS@NBSH@CHTS system.

AuNS@NBSH@CHTS have been therefore characterized by TEM (refer to **Section 3.1**). **Figure 4.9** shows TEM images obtained at two different magnifications, using uranyl acetate to enhance the contrast of the soft chitosan layer surrounding the gold nanostars.

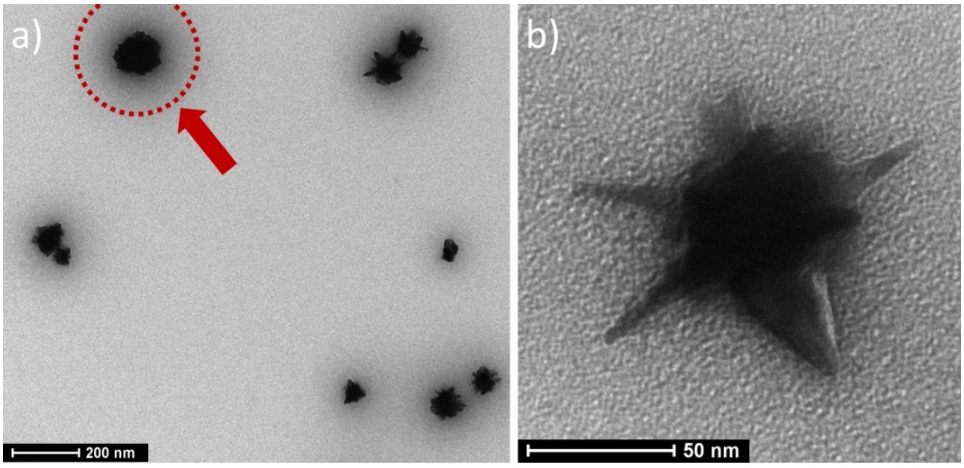

Figure 4.9. a) TEM image of AuNS@NBSH@CHTS. The sample of AuNSs was stained with uranyl acetate. The red dashed circle and arrow highlight the extent of the stained polymeric layer. b) Detail of a single AuNS@NBSH@CHTS.

As shown by Potara M. *et al.*, the staining process can highlight the polymer layer with which the AuNSs are functionalized. [94] A size analysis of the nanostars was performed using the opensource software ImageJ. [95] The average Feret's diameter turned out to be 113 ± 5 nm (n=199; confidence interval of 95%). The thickness of the stained chitosan layer was evaluated as well, revealing a thickness of 31 ± 1 nm (n=109; confidence interval of 95%). However, this analysis presents a fundamental problem, which is given by the lack of a clear boundary at the edge of the stained layer. Instead, there is a shadowing gradient which fades away moving apart from nanostars, as highlighted by the red circle in **Figure 4.9.a**. The thickness of the polymeric layer has thus been taken by measuring the distance between the edge of the nanostars and the point at which the color of the stained layer becomes comparable to that of the general image background. For this reason, this piece of data must be taken as a qualitative estimation. Furthermore, a comparison with literature data seems to cast doubt on whether nanostars and chitosan have interacted. In fact, Gubitosa *et al.* reported a TEM image of AuNPs capped with chitosan where a clear boundary between chitosan layer and environment can be clearly observed (**Figure 4.10**). [69] The synthesis proposed by the authors is similar to the one used in this thesis work (**Section 3.2.2**); however, it was followed by an addition of chitosan hydrogel, which may have resulted in a greater definition of the chitosan layer stained in the TEM image.

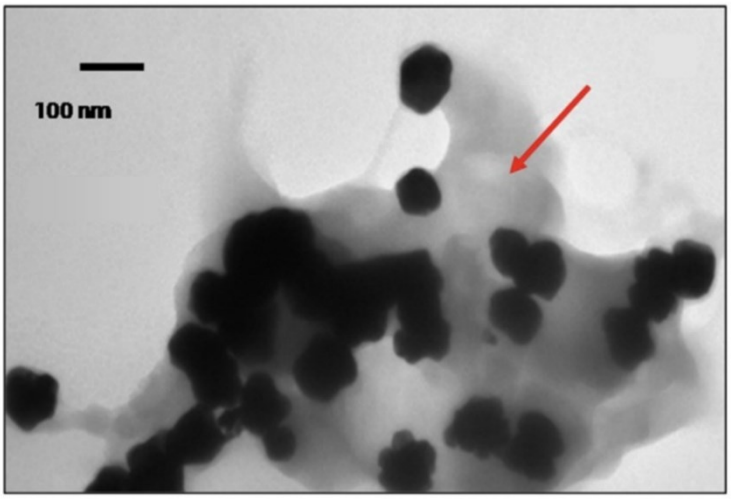

Figure 4.10. TEM image of AuNPs capped with chitosan hydrogel, from the publication of Gubitosa *et al.* [69] The red arrow indicates the presence of the soft chitosan shell around AuNPs.

However, a comparison between the TEM images of AuNS@NBSH@CHTS and an analogue formulation, MBA-tagged AuNS (AuNS@MBA, so without chitosan, average Feret's diameter 80 ± 4 nm, n=216, confidence interval of 95%), shows interesting results regarding the abovementioned thickness of the stained polymeric layer (**Figure 4.11**). Under the same TEM instrumental conditions and having both samples been stained with uranyl acetate, it is clearly visible that there is a substantial difference between the thickness of the shadow around the two samples: there is no layer to be seen as far as the sample of AuNS@MBA is concerned. This would confirm the formation of a chitosan layer bound to AuNSs.

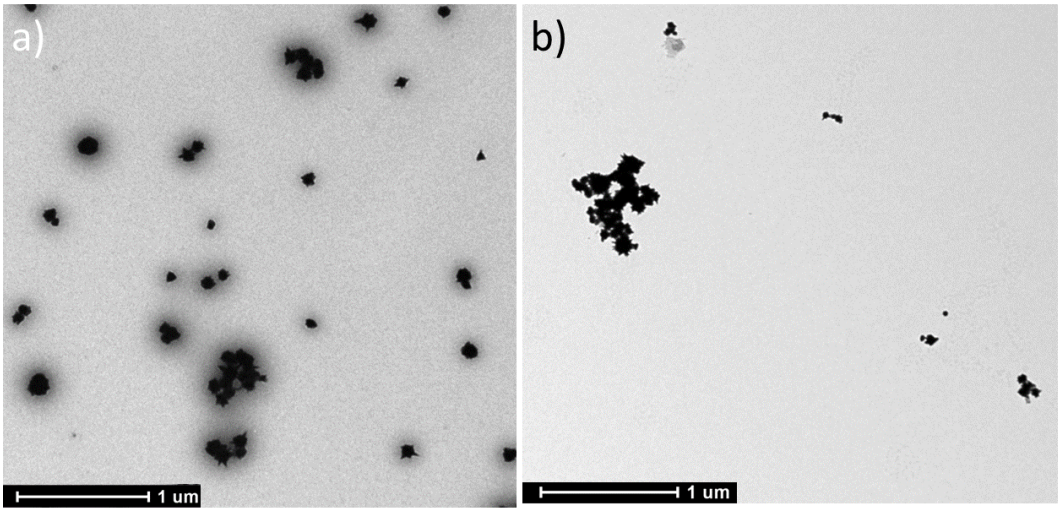

Figure 4.11. Comparison between a) AuNS@NBSH@CHTS and b) AuNS@MBA, both stained with uranyl acetate. The staining contribution (dark "shadow" around the AuNSs) is clearly visible on the AuNS@NBSH@CHTS sample (a), while it is not visible on the AuNS@MBA sample (b).

The same conclusion can be reached by observing **Figure 4.12**. By comparing the TEM images of AuNS@MBA, either stained with uranyl acetate (**Figure 4.12.a**) and unstained (**Figure 4.12.b**), one can see that the process of staining is uneffective as far as AuNS@MBA are concerned, given the similarity between the two images. The most probable hypothesis is that the staining process is not effective due to the small size of the MBA layer bound to the nanostar surface, which ultimately depends on the small molecular size of mercapto-benzoic acid (MW=154.19 g/mol). In contrast, the stained chitosan layer is visible due to its large molecular size (MW=3800÷20 000 g/mol).

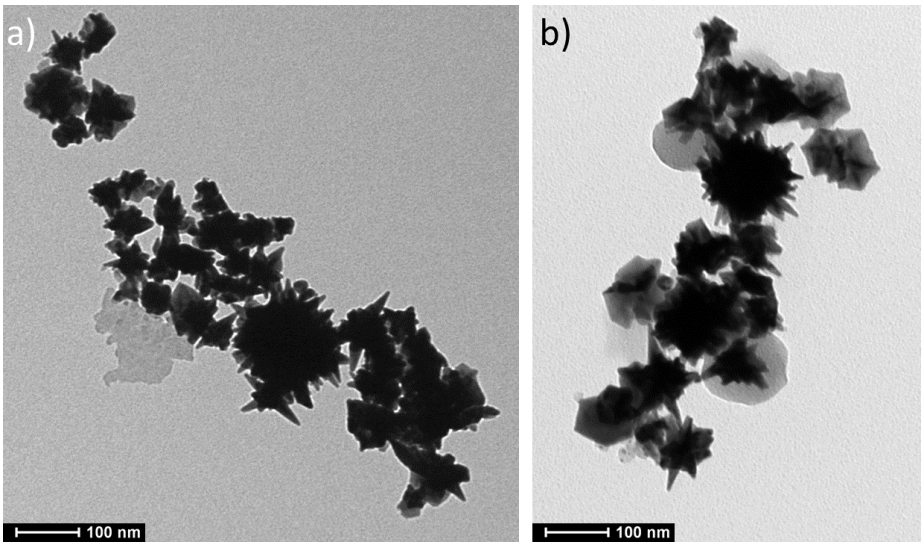

Figure 4.12. Comparison between a) stained AuNS@MBA and b) unstained AuNS@MBA. There is no visible difference between the two samples images, as far as staining is concerned, indicating that the staining process is not efficient for MBA-functionalized AuNSs.

The chitosan and Nile blue A functionalized AuNSs were used to encapsulate the terpenoids, as discussed in the previous chapter. The relative microbeads sample is hereafter marked with the letter “D”. TEM was again involved to address whether the AuNS@NBSH@CHTS did accumulate in correspondence of the microbeads. Given that the microbeads are essentially made of carbon, they result in a pale contrast only because of their microscale dimension. By the images reported in **Figure 4.13**, it it is worth noting that the chitosan-functionalized nanostars (the darker dots, as relative to the high density of Au with respect to carbon) are preferentially positioned within pale gray areas, namely the residues of the microbeads which survived to the vacuum environment within the TEM instrument.

One may also notice that the AuNSs do not entirety cover the beads surface. Indeed, the TEM technique cannot even provide evidence if the nanostars are located over, or into the beads.

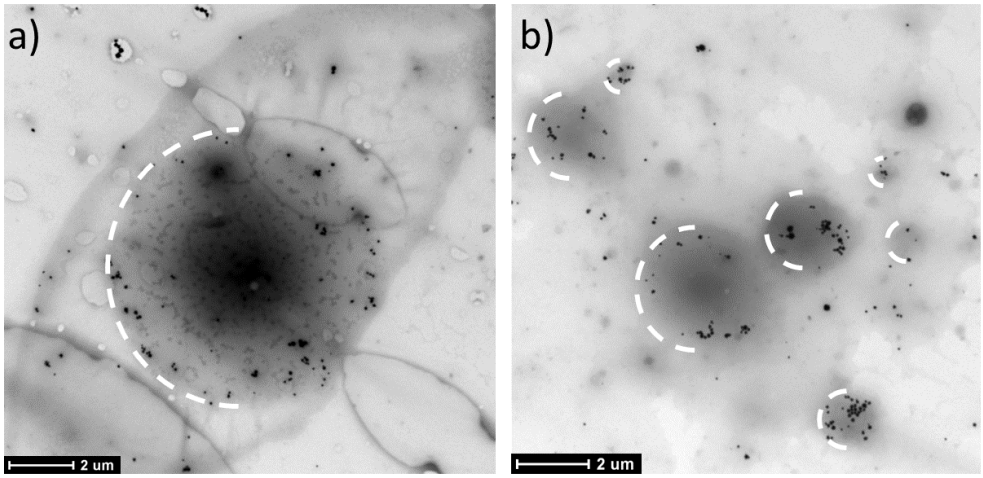

Figure 4.13. a,b) TEM images of different microbeads of formulation D. It can be seen that the AuNS@NBSH@CHTS (black dots) are localized preferentially inside the surface occupied by the residues of the evaporated microbeads (dark circular stains). The half dashed white circles help with the visualization of microbeads boundaries.

The next chapter will show how the characteristic Raman signals of AuNSs functionalized with chitosan and Nile blue A, as well as of all other components, are exploited.

4.1.3 Characterization by Raman spectroscopy means

This chapter shows the Raman spectra of all the pure components used in the preparation of the formulations (described in **Sections 3.2.3** and **4.1.1**). To avoid repetition, the Raman spectra of AuNS@NBSH@CHTS already presented and discussed in the previous chapter (**Section 4.1.2**) will not be reported in this chapter. The Raman spectra presented here are part of the so-called Raman spectra "library", which allows for the identification of components within formulations by comparison with experimental spectra by using PCC analysis (refer to **Section 3.3**).

Figure 4.14 shows the Raman spectra, obtained exciting at 633 nm (**Fig. 4.14.a**) and at 785 nm (**Fig. 4.14.b**), of the three terpenoids used in the mixture constituting the active principle of all the formulations (referred to as "terpenoids mixture"). **Table 4.3** displays the Raman signals assignments to the normal vibrational modes for each molecule.[93,96]

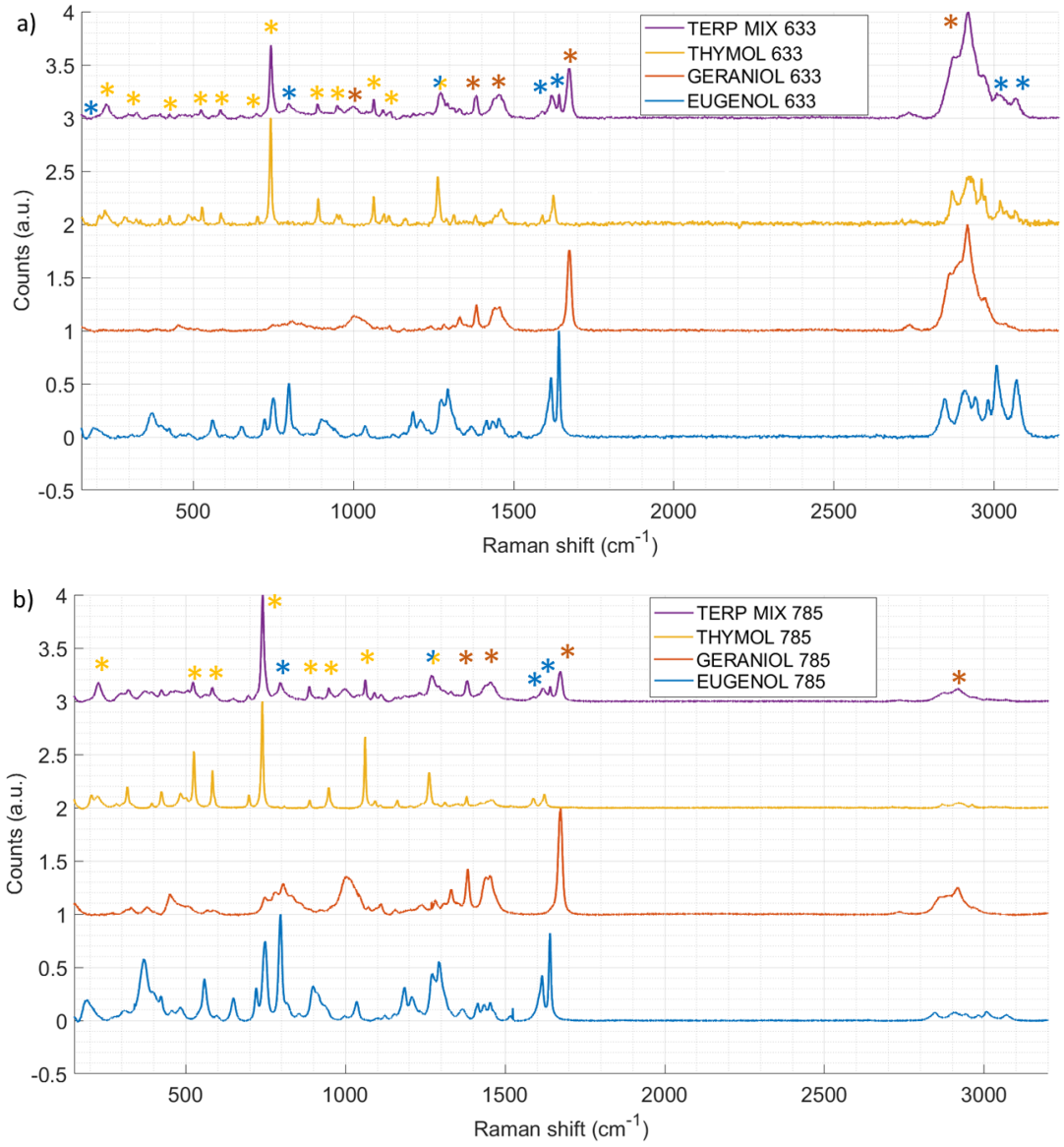

Figure 4.14. 633 nm (a) and 785 nm (b) laser line Raman spectra of the terpenoids mixture, as well as of its single components. The colored asterisks above the spectrum of the terpenoids mixture indicate to which individual component that particular peak in the spectrum is due, according to the legend color scheme.

Table 4.3. 633 nm and 785 nm laser line Raman signals assignments to the corresponding normal vibrational modes of each molecule. "o.ph. str." = out-of-phase stretch, "i.ph. str." = in-phase stretch.

Terpenoid	Raman shift (cm^{-1}) and intensity (633 nm excitation)	Raman shift (cm^{-1}) and intensity (785 nm excitation)	Assignment
Thymol	741 vs	740 vs	Ring quadrant in-plane bend [93]
	/	803 w	Ring deformation [93]
	890 m	888 w	Lone H wag [93]
	1063 m	1062 s	Ring in-plane C-H bend [93]
	1263 s	1263 m	Ar-OH: C-O str. [96]
	/	1380 w	Ar-CH_3: CH_3 bend [96]
	1462 w	/	R-CH_3: o.ph. bend [96]
	1590 w	1590 w	Ring quadrant str. [93]
	1624 m	1622 w	
	2868 m	/	Aryl-CH_3: bend overtone [96]
	2914-2931 s	/	Aryl-CH_3: i.ph. str. [93]
	2960 s	2962 w	R-CH_3: o.ph. str. [93]
	3019 m	/	Aryl-CH: C-H str. [93]
	3037 w	/	
	3064 w	/	
Geraniol	808 w	805 m	CH_2-OH: C-O str. [96]
	1003 m	/	
	1384 s	1383 m	$(CH_3)_2$ bend [96]
	1442 s	1439 m	CH_3/CH_2 bend [96]
	1456 s	1456 m	
	1674 vs	1674 vs	C=C(tri) str. [96]
	2862 s	/	R-CH_2-R i.ph. str. [93]
	2917 vs	2919 m	R-CH_2-R o.ph. str. [93]
	2972 m	/	R-CH_3 o.ph. str. [93]
Eugenol	798 s	797 vs	R-CH=CH_2: =CH wag [96]
	899 m	899 m	Lone H wag [93]
	1036 w	1034 w	Ar-O-CH_3: O-CH_3 str. [96]
	1185 m	1186 m	Ar-OH: C-O str. [96]
	1209 w	1210 w	
	1275 s	1271 m	Ar-O str. [96]
	1294 s	1292 m	
	1434 m	1436 w	R-O-CH_3: i.ph. bend [93]
	1453 m	1454 w	
	1518 w	/	Ring semicircle str. [93]
	1616 s	1615 m	Ring quadrant str. [93]
	1641 vs	1641 s	C=C(mono) str. [96]
	2845 m	2848 w	R-O-CH_3: i.ph. str. [96]
	2980 m	2983 w	C=CH_2(mono): CH_2 i.ph. str. [93]

As expected, the spectra resulting from the use of two different laser lines do not differ with regard to the position or presence of peaks, the only appreciable difference is the relative intensities between the peaks, as is clearly visible in **Figure 4.15**.

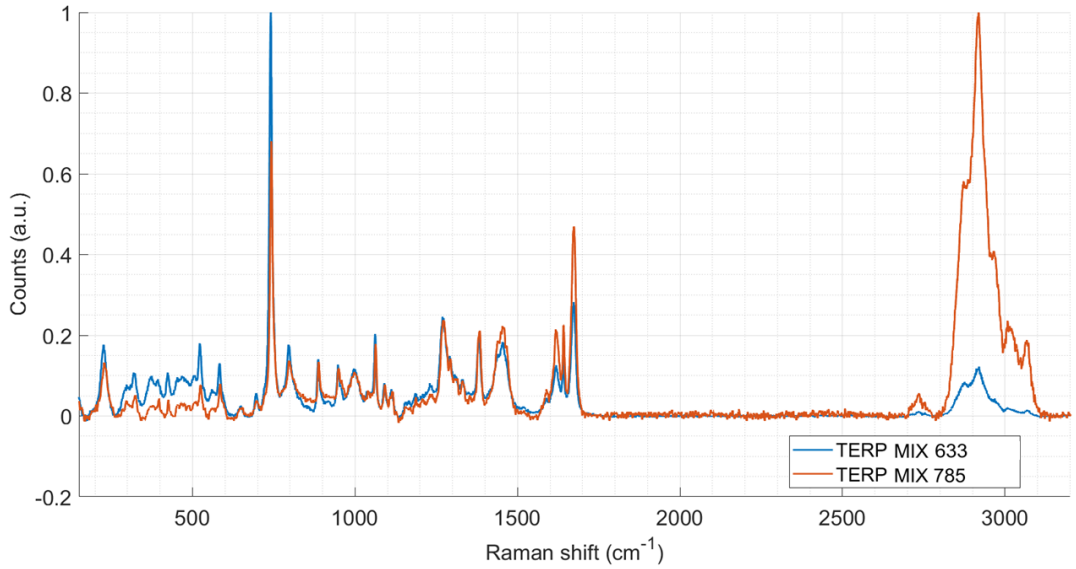

Figure 4.15. Comparison between the Raman spectra of the terpenoids mixture obtained by using two different laser lines. The main difference consists only of the relative intensity of the peaks between the two Raman spectra.

An attempt was made to separate the spectral contributions of the individual components from the experimental terpenoids mixture Raman spectrum, by means of a deconvolution algorithm. **Figure 4.16** shows the results. The purpose of this analysis is to have a tool to automatically determine whether the terpenoid spectrum changes in its shape, taken as the sum of the three contributions, before and after UV treatment. The resulting coefficients of each single component contribution to the overall spectrum of the mixture are 0.57, 0.88 and 0.67 for thymol, geraniol and eugenol, respectively. This is by no means an analytical analysis of the estimated mixture composition, if only because the spectra were taken as normalized.

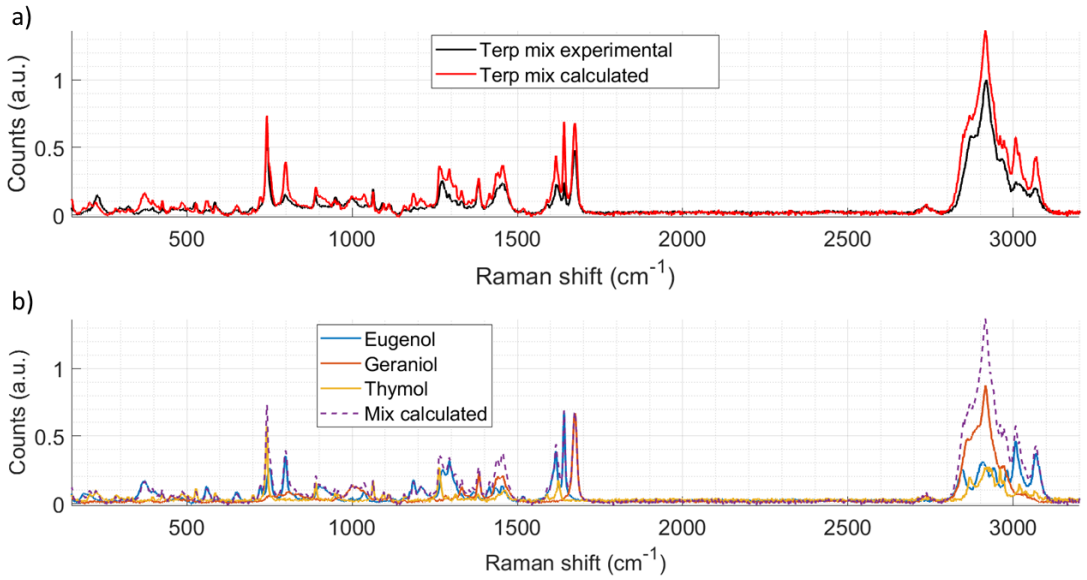

Figure 4.16. a) Comparison between the 633 nm laser line experimental Raman spectrum of the terpenoids mixture (in black) and the calculated one (in red). b) Superposition of the calculated Raman spectrum of the terpenoids mixture (dashed, purple curve) with the single compounds' spectra. Each single compound spectrum has been weighted according to the corresponding coefficient deriving from the deconvolution analysis.

For the sake of completeness, the Raman spectra of the other components are also shown, together with the corresponding Raman peaks assignments: chitosan (**Figure 4.17**, **Table 4.4**), soybean lecithin (**Figure 4.18**, **Table 4.5**) and AMD 10 (**Figure 4.19**, **Table 4.6**). Chitosan exhibits relatively low absolute intensities in Raman spectra, as shown by **Fig. 4.17**. Specifically, the difference with absolute intensities of other compounds is least an order of magnitude smaller (according to the CCD sensor). For this reason, the spectral fingerprint of chitosan is not visible when other compounds are also present in the sample, as could be observed in the following chapters. This is also one of the reasons why the system of AuNSs capped with the SERS reporter was designed, as already discussed in **Section 2.1.2**. Similar arguments apply to soybean lecithin, which was not localizable or detectable in any formulation, despite the high absolute intensities of the Raman peaks obtained with excitation at 785 nm. However, the rationale behind the inability to properly localize this compound, which is theoretically localized at the interphase between the oil and aqueous phases, is likely due to the small thickness of the lecithin layer.

It is worth noting that chitosan and AMD 10 Raman spectra at 785nm, as well as soybean lecithin spectrum at 633 nm, were not presented nor used hereafter, because of the lack of significative signals.

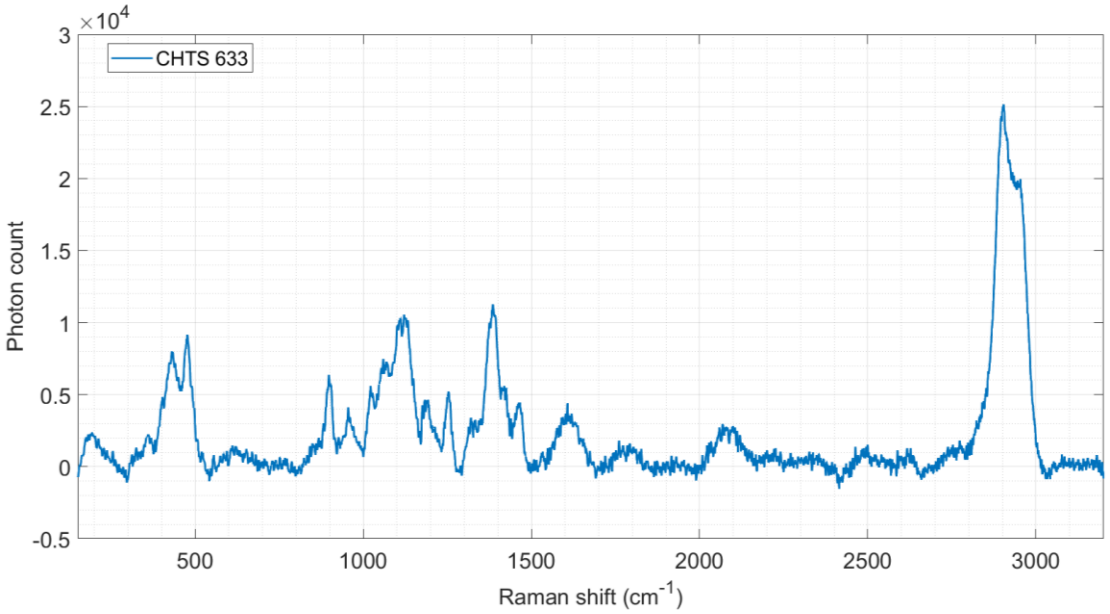

Figure 4.17. Reference Raman spectrum of chitosan, 633 nm laser line. Absolute intensities shown.

Table 4.4. Raman peaks assignments for chitosan, 633 nm laser line.

Raman shift (cm^{-1})	**Intensity**	**Assignment** [97]
1053-1191	s	C-C str. Region
1290-1350	s	C-N-H bend
1385	m	Bridge oxygen str.
1462	s	Amide-III
1542-1691	w	Amide-I, amide-II

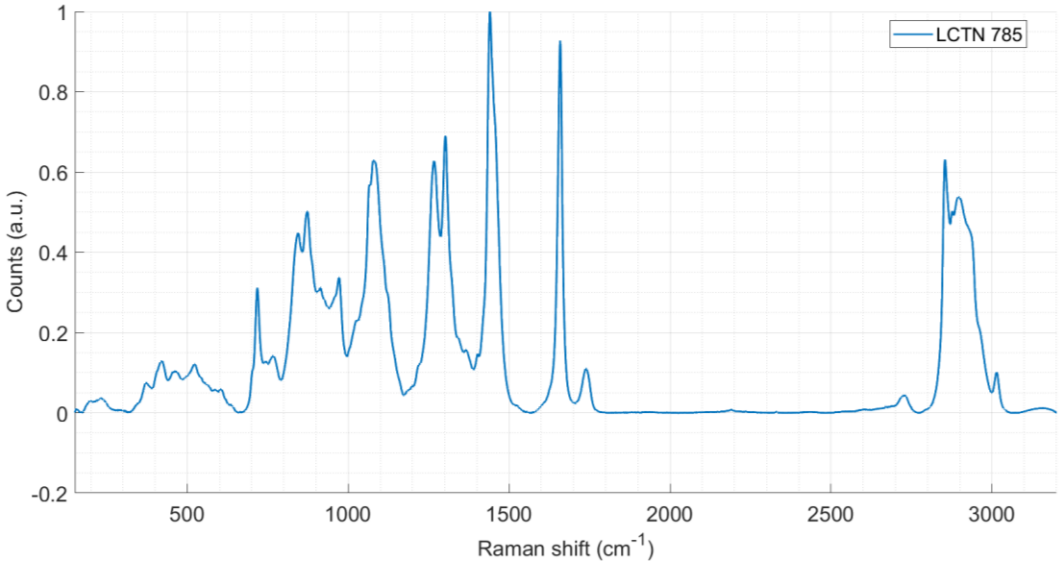

Figure 4.18. Reference Raman spectrum of soybean lecithin, 785 nm laser line.

Table 4.5. Raman peaks assignments for soybean lecithin, 785 nm laser line.

Raman shift (cm^{-1})	**Intensity**	**Assignment** [98]
718	m	CH_2 rocking
972	s	Glycogen/=CH_2 alkenes
1080	s	C-O str. (esters)
1267	s	CH_2 twisting (lipids)/C-O str. (phospholipids)
1302	s	C-N str. (amide-III)/P=O str. (phospholipids)
1440	vs	CH_2 scissoring/CH_3 asymm. bend (lipids)
1659	vs	Amide-I/C=O str. (proteins)
1740	w	C=O (phospholipids, cholesterol esters)

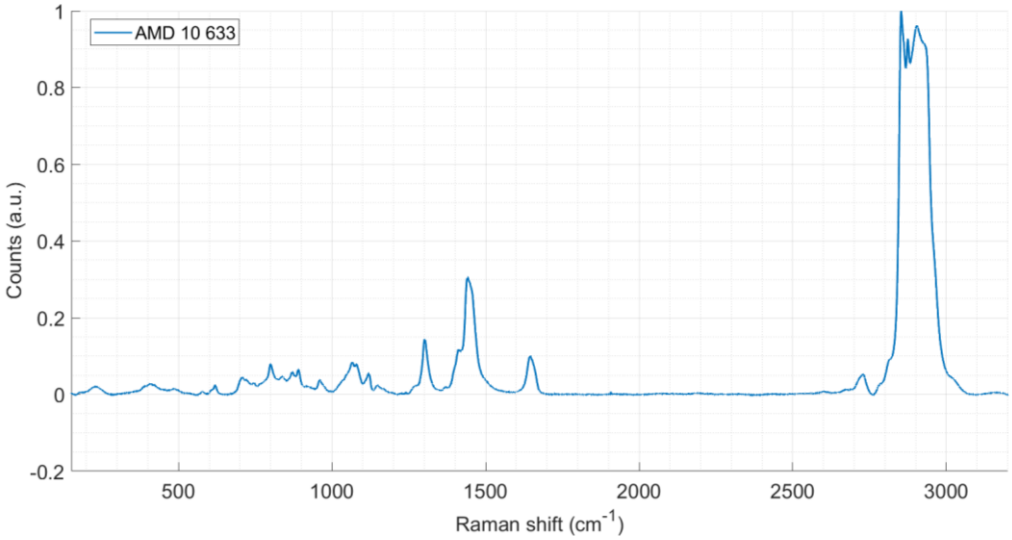

Figure 4.19. Reference Raman spectrum of AMD 10, 633 nm laser line.

Table 4.6. Raman peaks assignments for AMD 10, 633 nm laser line. [99–101]

Raman shift (cm^{-1})	Intensity	Assignment
619	w	Amide-V[99]
799	w	N-H bend out of plane (amide-V) [99]
890	w	C-C str. [100]
960	w	C-C str. [100]
1080	w	C-C, C-N, C=O str. [100]
1443	m	CH_2, CH_3 def. [101]
1645	w	C=O str. (amide-I) [99]

4.2 Characterization of the formulations prior to the photodegradation process

4.2.1 Characterization by point Raman maps

The four formulations of terpenoid-encapsulating microbeads have initially been characterized by point Raman maps, namely by acquiring spectra only in correspondence of a microbead. The aim is to sample a statistically relevant number of microspheres to answer the question of whether all microspheres contain the active ingredient and if the terpenoids mixture composition, evaluated in terms of spectral features, are retained. To do so, about 15 μL of microbeads aliquots were deposited on a glass slide (refer to the **Section 3.2.1** for details), and single Raman spectra were acquired over each microbead on a large portion of the sample area. For reference, few spectra were acquired outside of the beads too, to check background signals from the solution. The obtained dataset is compared to the reference spectra by means of the PCC analysis. Spectra that closely match the reference will have a high R-value, and vice versa. A colored chemometric scale, ranging from dark blue (low R-scores) to dark red (high R-scores), helps with the score visualization and is presented superimposed to the image of the mapped area. Points in the map that are closest to the maximum R-score, and thus to the dark red, will mostly consist of the compound whose spectrum was used for the comparison. The next paragraphs will show the results in detail.

Figure 4.20 shows the point Raman map of formulation A (1:10 dilution in deionized water), before the photodegradation process. It is clearly visible that the active principle is present in most of the micelles. The correspondence between experimental and reference Raman spectra is nearly perfect, as shown by **Figure 4.20.b**. Some micelles, however, appear to not contain the active principle. It is possible that these low-scoring micelles are only consisting of soybean lecithin, or air bubbles. On the contrary, no signal attributable to terpenoids was localized outside the micelles, indicating a good encapsulation efficacy.

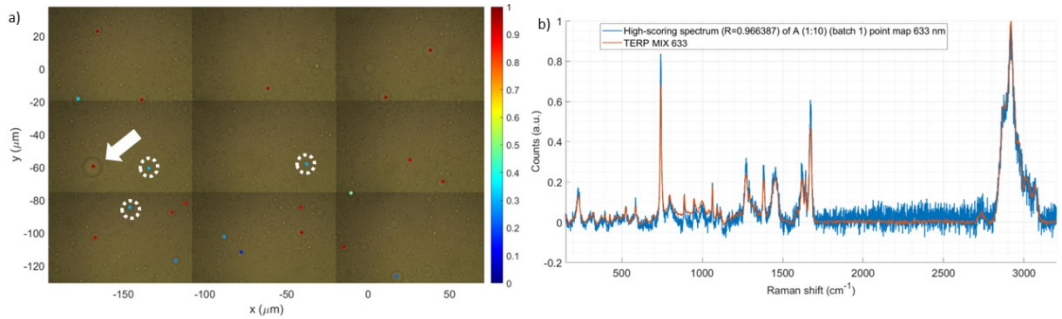

Figure 4.20. a) Point Raman map of formulation A (1:10), 633 nm laser line. Pearson's correlation coefficient (R) analysis, reference: terpenes mix. Raman spectra of the solution are highlighted by white dashed circles. The white

arrow points to the location of the high-scoring Pearson's R spectrum appointed in section (b). b) High-scoring Pearson's R spectrum (R≃0.97) compared to terpenes mix reference spectrum.

Figure 4.21 aims to verify the proportion of the three individual terpenoids (*i.e.*, geraniol, thymol and eugenol) in formulation A by comparing it with their proportion in the reference terpenoids mixture. In fact, this plot was obtained by weighting the Raman spectrum of each individual terpenoid by the corresponding deconvolution coefficient (see **Section 4.1.3**). One can thus obtain a clear match between the superposition of the weighted spectra and the experimental high-scoring spectrum of the point Raman map, indicating the presence of all three terpenoids in the beads of formulation A.

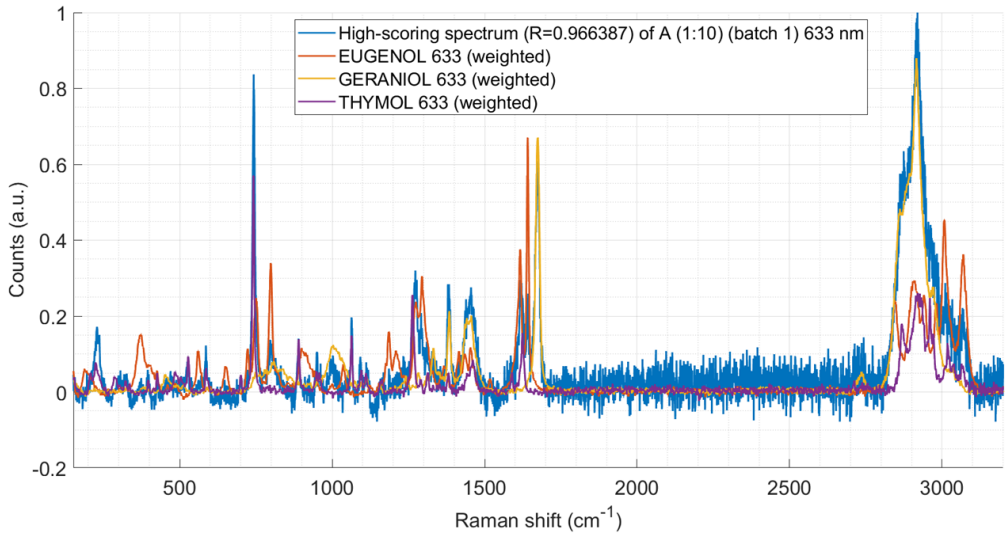

Figure 4.21. Comparison between the same experimental high-scoring spectrum shown in the previous figure and the deconvolution coefficient weighted Raman spectra of the single terpenoids. An almost perfect juxtaposition can be observed.

This analysis is only qualitative, meaning that the match between experimental and weighted spectra of individual terpenoids, although very good, is not only related to any information about their concentration. In **Figure 4.22** is presented the linear combination analysis for each of the mapped beads, in which the reference spectra of the three terpenoids are used as basis set. The continuous lines are referred to the coefficients for the reference spectrum of the terpenoids mixture, and the dots to the mapped beads. The index on the abscissae represents the number of the experimental spectrum that makes up the point Raman map. Regarding formulation A, some correspondence can be observed between the linear coefficients of the individual terpenoids in the experimental spectra and those of the terpenoid mixture reference. Although the correspondence is not perfect (*i.e.*, a perfect overlap between points and lines), it confirms the

presence of all the three components. Proportions that are far off from the reference, namely the highlighted indexes in **Fig. 4.22**, are attributable to very noisy spectra or of the solution.

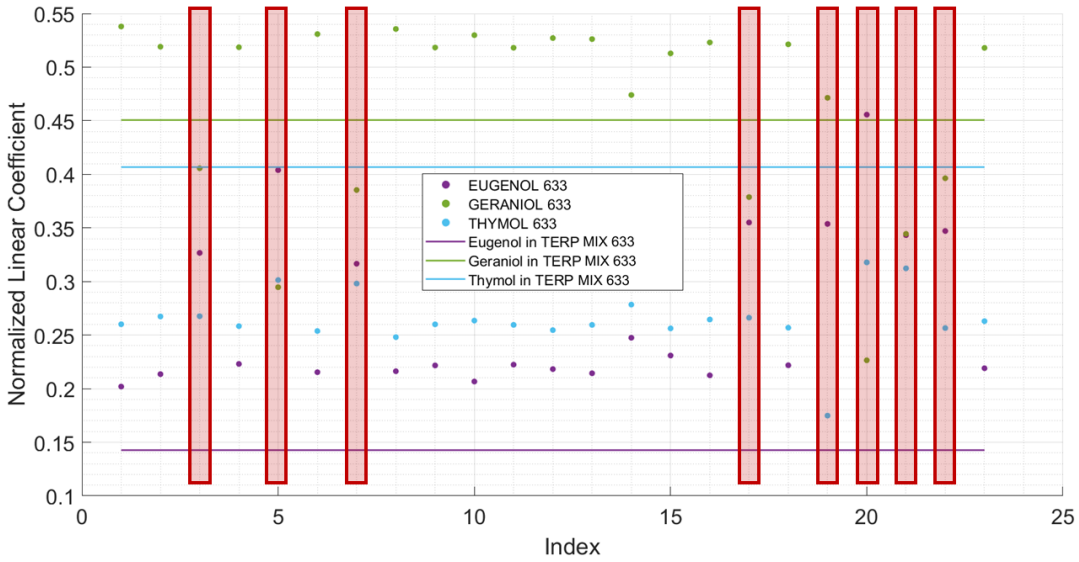

Figure 4.22. Proportions of the single terpenoids for each experimental spectra acquired for the creation of the point Raman map of A (1:10), 633 nm, pre-degradation. On the ordinates are the normalized linear coefficients, on the abscissae are the indexes indicating each spectrum acquired in the 2D Raman point map. The colored dots represent the contributions of each terpenoid to the experimental spectra, the colored straight lines represent the contributions of each terpenoid to the reference terpenoids mixture. Dark red boxes highlight the spectra whose proportions are far off from the reference ones.

Figure 4.23 shows the point Raman map of formulation B (1:10 dilution in deionized water), before the photodegradation process. As in the previous case, the match between the Raman spectra acquired at the core of the microbeads and the reference spectrum of the terpenoids mixture is almost perfect. Unlike before, however, all the analyzed microbeads showed the terpenoids Raman fingerprint, indicating perfect encapsulation of the active ingredient. Most likely, the presence of the chitosan stabilizes the microbeads, ensuring a more prolonged retention of the active ingredient within the microcapsules. However, chitosan contributions are not detectable for the reasons described in **Section 4.1.3**.

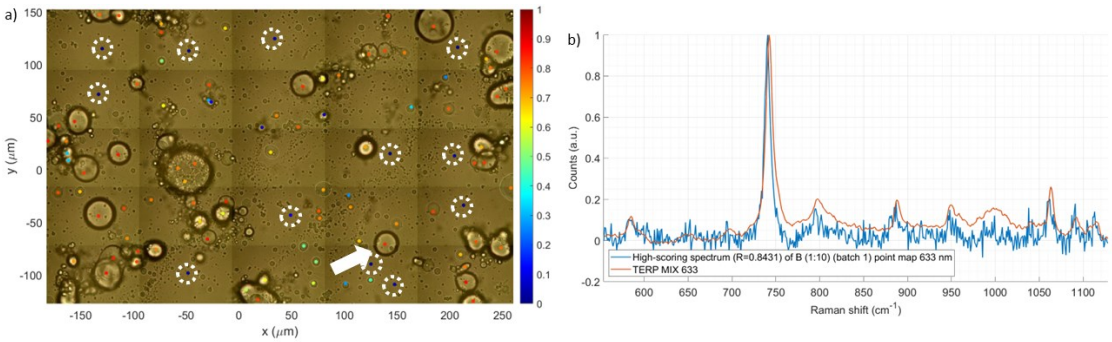

Figure 4.23. a) Point Raman map of formulation B (1:10), 633 nm laser line. Pearson's correlation coefficient (R) analysis, reference: terpenes mix. Raman spectra of the solution are highlighted by white dashed circles. The white arrow points to the location of the high-scoring Pearson's R spectrum appointed in section (b). b) High-scoring Pearson's R spectrum (R≃0.84) compared to terpenes mix reference spectrum.

Figure 4.24 shows the same plot already seen in **Fig. 4.22**, to evaluate the proportions of terpenoids in formulation B compared to the ones of the reference terpenoid mixture. The proportions are found to be quite similar, even if not perfect, although one may appreciate fluctuations along different beads. The match is indeed satisfactory, considering that the experimental spectra have been acquired in aqueous solution and in the presence of other compounds (*i.e*, chitosan, soybean lecithin), as opposed to the pure reference terpenoid mixture spectra, for instance. The proportions on the far right of the plot (index>70) do not match those of the reference. The corresponding spectra present a low R-value and have a low signal-to-noise ratio, that is because these spectra are obtained from the solution outside the microbeads: therefore, they present no contribution from the active ingredient. For this reason, the proportions do not match. The linear coefficients of individual terpenoids are different from those observed in **Fig. 4.22** because the mapped Raman shift window is different from the previous case. In this case, specifically, the acquired window has the diagnostic thymol peak at 741 cm^{-1} as its center. The deconvolution algorithm places larger linear coefficients for this terpenoid. In the previous case, the acquisition window was extended, so higher scores were given to geraniol, which has more intense and broader peaks around 3000 cm^{-1}.

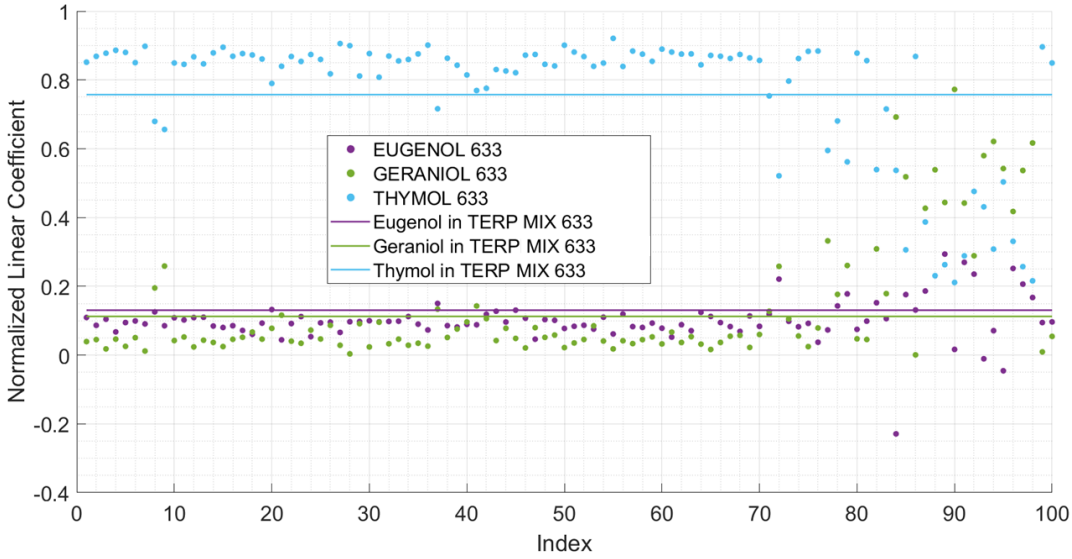

Figure 4.24. Proportions of the single terpenoids for each experimental spectra acquired for the creation of the 2D Raman point map of B (1:10), 633 nm, pre-degradation. On the ordinates are the normalized linear coefficients, on the abscissae are the indexes indicating each spectrum acquired in the 2D Raman point map. The colored dots represent the contributions of each terpenoid to the experimental spectra, the colored straight lines represent the contributions of each terpenoid to the reference terpenoids mixture.

Figure 4.25 shows the point Raman map of formulation C (1:10 dilution in deionized water), before the photodegradation process. As before, an excellent match can be observed between the experimental Raman spectra acquired inside the cores of the microbeads and the reference terpenoids mixture Raman spectrum, as well as a satisfactory absence of the active principle in the solution. The proportion analysis of the terpenoids yields very similar results as the ones observable in **Fig. 4.24**, with a very good match between the proportion of the terpenoids in formulation C and that of the reference mixture. For this reason, the corresponding plot will not be reported.

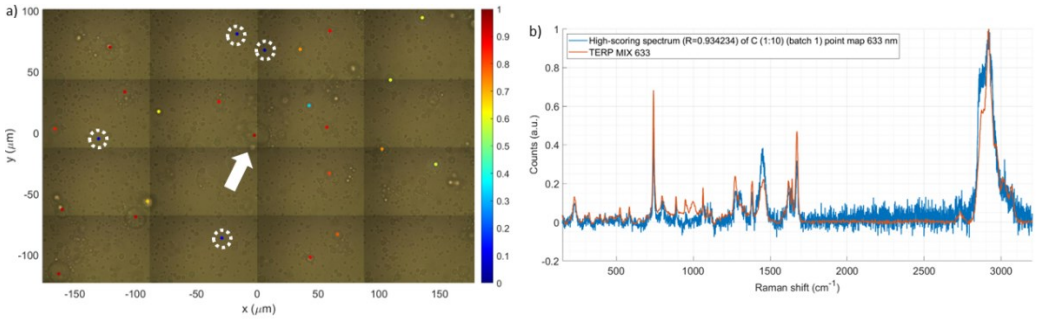

Figure 4.25. a) Point Raman map of formulation C (1:10), 633 nm laser line. Pearson's correlation coefficient (R) analysis, reference: terpenes mix. Raman spectra of the solution are highlighted by white dashed circles. The white arrow points to the location of the high-scoring Pearson's R spectrum appointed in section (b). b) High-scoring Pearson's R spectrum (R≃0.93) compared to terpenes mix reference spectrum.

By comparing the experimental spectra with that of AMD 10 reference, one can observe its localization within the microbeads cores, as expected (**Figure 4.26**). The experimental spectra show a blend of the terpenoids and AMD 10 spectral fingerprints, as one may appreciate by the increased intensity of the bands at 1442 and 2853 cm^{-1} in **Fig. 4.26**, with respect to the reference terpenoids mixture spectrum. Given that these two are the most intense AMD 10 bands, their increase confirms its presence within the terpenoids mixture in the cores of the microbeads. This fact is compatible with the high solubility of the active ingredients in AMD 10, and therefore confirms the mixing of these two components.

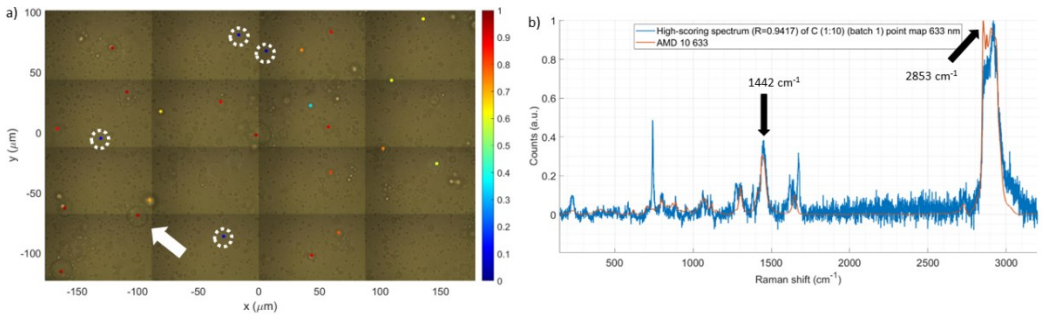

Figure 4.26. a) Point Raman map of formulation C (1:10), 633 nm laser line. Pearson's correlation coefficient (R) analysis, reference: AMD 10. Raman spectra of the solution are highlighted by white dashed circles. The white arrow points to the location of the high-scoring Pearson's R spectrum appointed in section (b). b) High-scoring Pearson's R spectrum (R≃0.94) compared to AMD 10 reference spectrum. The black arrows indicate the two most intense peaks of AMD 10.

Figure 4.27 shows the point Raman map of formulation D (1:10 dilution in deionized water), before the photodegradation process. The results are similar to previous situations, with a preferential localization of the active principle, as well as of AMD 10, within the cores of the microbeads, as expected.

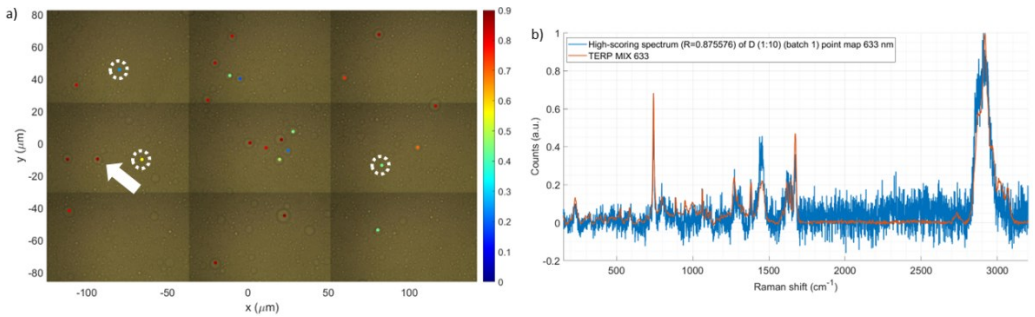

Figure 4.27. a) Point Raman map of formulation D (1:10), 633 nm laser line. Pearson's correlation coefficient (R) analysis, reference: terpenes mix. Raman spectra of the solution are highlighted by white dashed circles. The white arrow points to the location of the high-scoring Pearson's R spectrum appointed in section (b). b) High-scoring Pearson's R spectrum (R≃0.88) compared to terpenes mix reference spectrum.

The same results have been achieved by using the 785 nm laser line. **Figure 4.28** shows the 785 nm point Raman map of formulation D (1:10 dilution in deionized water), before the photodegradation process. The greater number of low R-value spectra could be appointed to the fact that 785 nm laser line Raman spectra had to be acquired with the sample deposited onto an adhesive aluminium foil, as was necessary for all acquisitions using this laser line, to mitigate the glass interference typical of the Raman technique with this excitation wavelength. It was therefore not possible to illuminate the sample in transmission, but only in reflection, which ultimately made the recognition of microbeads more difficult due to the weaker contrast. It is possible that these low-scoring spectra are thus from the solution outside the core of the microbeads. In any case, the spectra that are certainly attributable to the solution are highlighted in **Fig. 4.28.a** by dashed white circles.

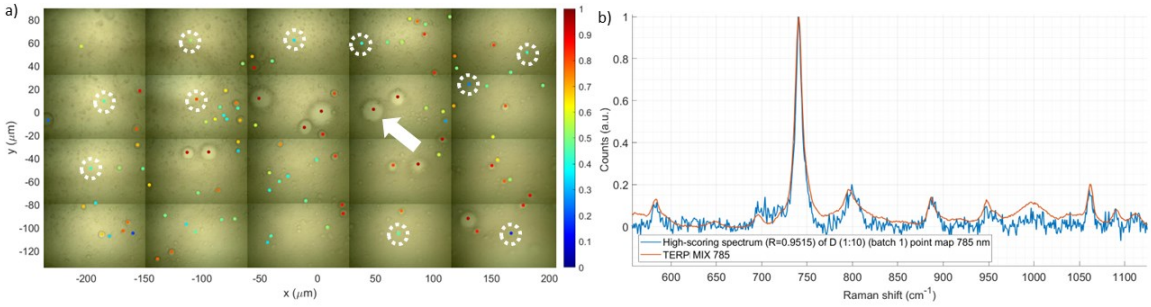

Figure 4.28. a) Point Raman map of formulation D (1:10), 785 nm laser line. Pearson's correlation coefficient (R) analysis, reference: terpenes mix. Raman spectra certainly attributable to the solution are highlighted by white dashed circles. The white arrow points to the location of the high-scoring Pearson's R spectrum appointed in section (b). b) High-scoring Pearson's R spectrum (R≃0.95) compared to terpenes mix reference spectrum.

By comparing the experimental spectra with that of AuNS@NBSH@CHTS reference, one can observe a limited number of matches throughout the mapped area (**Figure 4.29**). In fact, only two spectra show Raman signals traceable to those of AuNSs. The spectra shown in **Figures 4.29.b** and **4.29.c** show, to varying degrees, contributions from both the AuNSs (peak at 592 cm^{-1}) and the active ingredient (peak at 741 cm^{-1}). This could result from the fact that point Raman maps ensure only partial sampling of the microspheres, as far as the spectra are acquired at the center of the microbeads. In fact, in this way, the signal of terpenoids present in the core would completely mask that of the AuNSs, which are present only at the microbeads edges and therefore not within the sampled volume. The contributions of AuNSs observed in this analysis would thus mainly derive from sampling the boundary of a microbeads, where the vertical projection over the micelle interface makes both the active principle and the AuNSs clearly visible, as evidenced by **Fig. 4.29.c**.

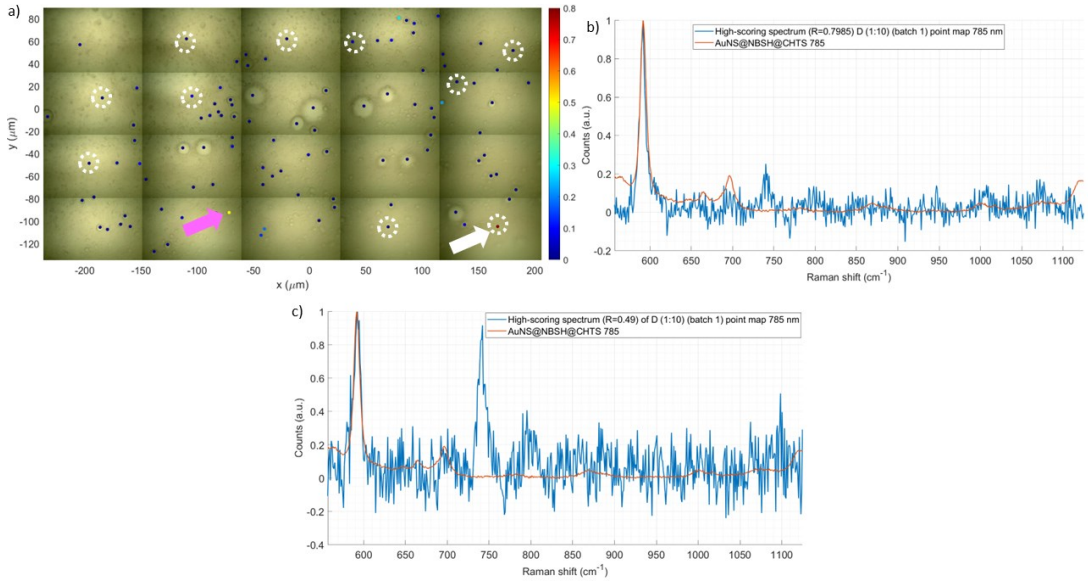

Figure 4.29. a) Point Raman map of formulation D (1:10), 785 nm laser line. Pearson's correlation coefficient (R) analysis, reference: AuNS@NBSH@CHTS. Raman spectra of the solution are highlighted by white dashed circles. The white arrow points to the location of the high-scoring Pearson's R spectrum appointed in section (b). The magenta arrow points to the location of the high-scoring Pearson's R spectrum appointed in section (c). b) High-scoring Pearson's R spectrum (R≃0.80) compared to AuNS@NBSH@CHTS reference spectrum. c) High-scoring Pearson's R spectrum (R≃0.49) compared to AuNS@NBSH@CHTS reference spectrum.

4.2.2 Characterization by 2D Raman maps

2D Raman maps are another key element for the characterization of the microbeads, being acquired by using the greater magnification and resolution possible with the micro-Raman instrument setup (100x optical magnification, spatial resolution of 1 μm; refer to **Section 3.2.1**). The aim is to correctly locate the position of each component among the morphological structure of the microbeads. As before for point Raman maps, the analysis is based on the PCC analysis and its visualization with the help of a colored, chemometric scale, which ultimately allows to localize the spectral contributions upon the image of the analyzed microbead.

Figure 4.30 shows the 2D Raman map of formulation A (1:10 dilution in deionized water), before the photodegradation process. There is a clearly visible localization of the terpenoids mixture within the core of the analyzed micelle, as shown by the comparison with the reference spectrum displayed in **Figure 4.30.b**. As for the point Raman maps described in **Section 4.2.1**, the Pearson's correlation analysis for soybean lecithin yielded non statistically significant R-values (<0.3).

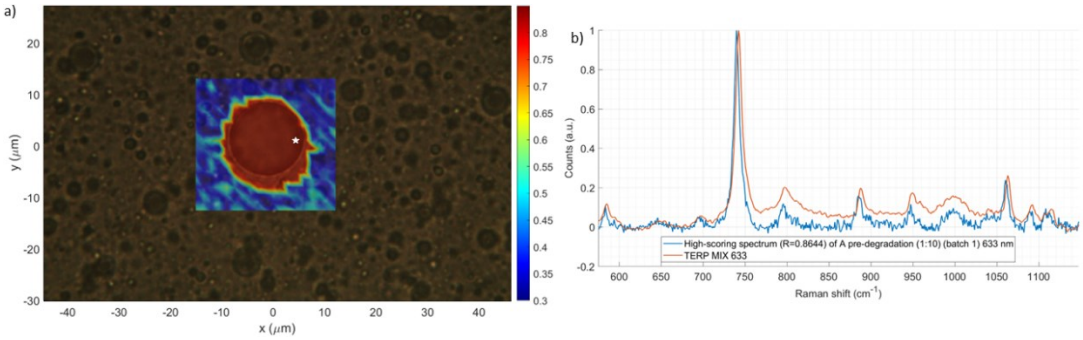

Figure 4.30. a) 2D Raman map of formulation A (1:10), 633 nm laser line. Pearson's correlation coefficient (R) analysis, reference: terpenes mix. The white star points to the location of the high-scoring Pearson's R spectrum appointed in section (b). b) High-scoring Pearson's R spectrum (R≃0.86) compared to terpenes mix reference spectrum.

Figure 4.31 shows the 2D Raman map of formulation B (1:10 dilution in deionized water), before the photodegradation process. Again, there is a visible localization of the active principle inside the core of mapped microbeads. The Pearson correlation with chitosan and soybean lecithin reference spectra yielded non-significant R-values (<0.30), as before.

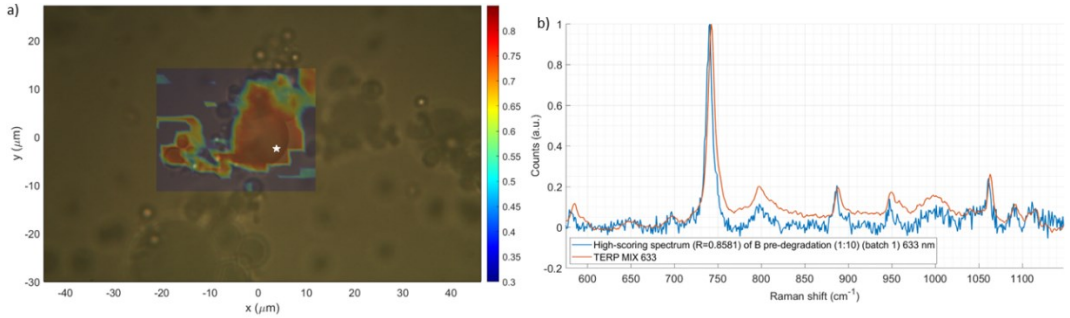

Figure 4.31. a) 2D Raman map of formulation B (1:10), 633 nm laser line. Pearson's correlation coefficient (R) analysis, reference: terpenes mix. The white star points to the location of the high-scoring Pearson's R spectrum appointed in section (b). b) High-scoring Pearson's R spectrum (R≃0.86) compared to terpenes mix reference spectrum.

Figure 4.32 shows the detailed 2D Raman map of formulation C (1:10 dilution in deionized water), before the photodegradation process. As far as the localization of the active principle is concerned, the detailed mapping yielded the same results as before.

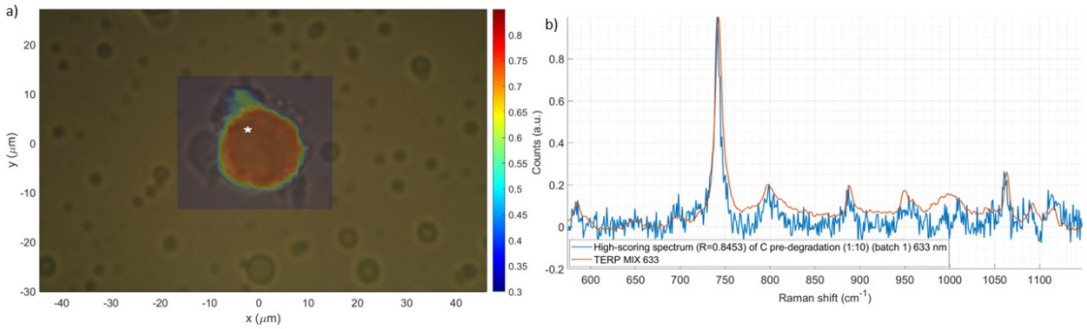

Figure 4.32. a) 2D Raman map of formulation C (1:10), 633 nm laser line. Pearson's correlation coefficient (R) analysis, reference: terpenes mix. The white star points to the location of the high-scoring Pearson's R spectrum appointed in section (b). b) High-scoring Pearson's R spectrum (R≃0.85) compared to terpenes mix reference spectrum.

AMD 10 could not be easily detected due to the measurement setup: indeed, the selected Raman shift acquisition range did not present any intense and diagnostic band of AMD 10, as shown in **Figure 4.33**. Furthermore, the intensity of the AMD 10 peaks within this range is too poor and not sufficient for its discrimination.

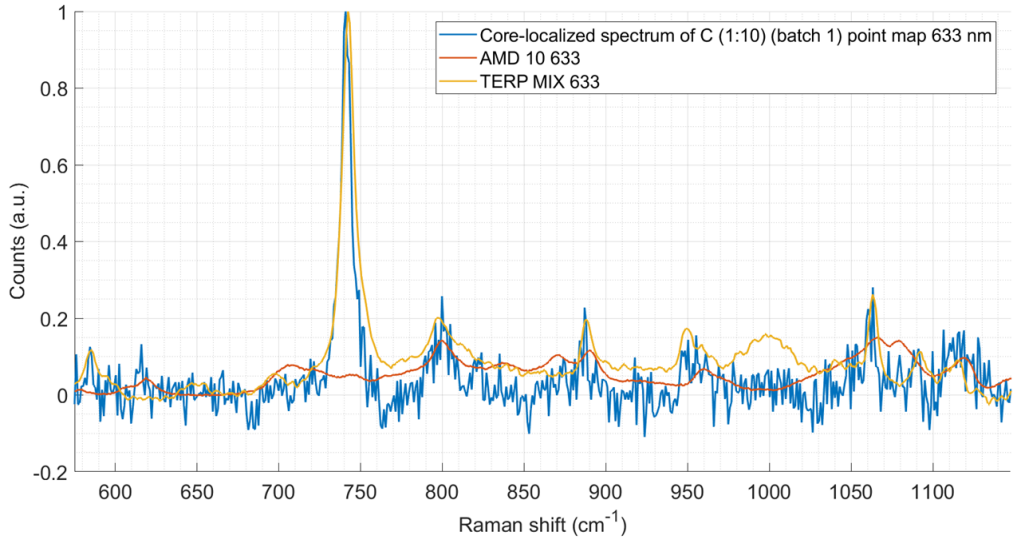

Figure 4.33. Comparison between an experimental Raman spectrum of the core of the microbead analyzed in the previous detailed map, the terpenoids mixture and AMD 10 reference spectra. The orange boxes highlight the weak but not null correspondence of the experimental spectrum with the AMD 10 reference one.

Figure 4.34 shows the 2D Raman map of formulation D (1:10 dilution in deionized water), before the photodegradation process. The map confirms the presence of the active principle inside the core of the microbeads, with an excellent correlation of the experimental spectra to the reference one of the active principles, as shown by **Figure 4.34.b**.

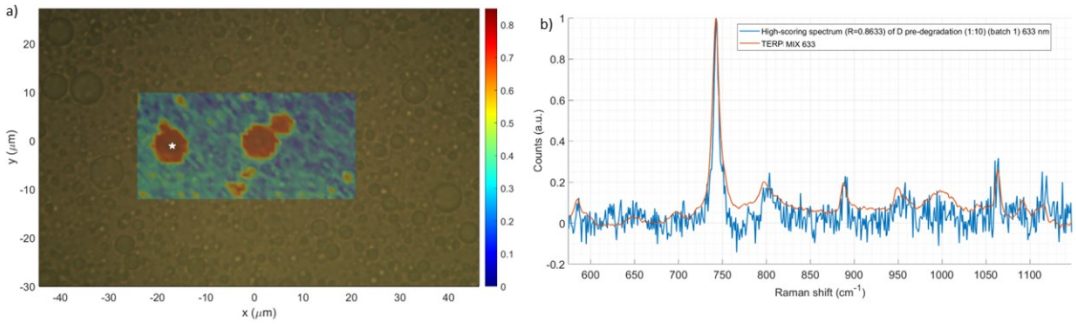

Figure 4.34. a) 2D Raman map of formulation D (1:10), 633 nm laser line. Pearson's correlation coefficient (R) analysis, reference: terpenes mix. The white star points to the location of the high-scoring Pearson's R spectrum appointed in section (b). b) High-scoring Pearson's R spectrum (R≃0.86) compared to terpenes mix reference spectrum.

Figure 4.35 shows the 2D Raman map of formulation D (1:10 dilution in deionized water), before the photodegradation process, acquired by using the 785 nm laser line, more sensible to the signals of the SERS reporter bonded to AuNSs. It can be easily seen that the signals of AuNS@NBSH@CHTS are localized preferentially outside the core of the analyzed microbead, as revealed by the same map visualized through the Pearson's correlation with the terpenoids mixture (**Figure 4.36**). Although the spectra attributable to the active principles present a low signal-to-noise ratio, it is clearly visible that the terpenoids are localized inside the core of the mapped microbead. As seen with point Raman maps (**Section 4.2.1**), these spectra possess both diagnostic peaks of AuNSs and of the terpenoids mixture.

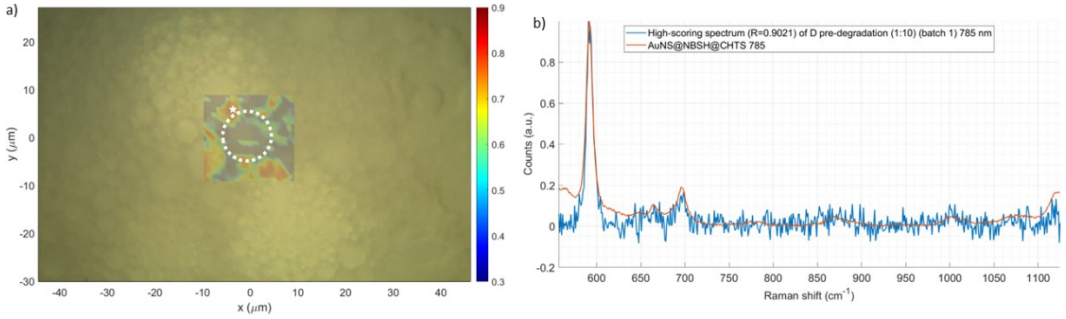

Figure 4.35. a) 2D Raman map of formulation D (1:10), 785 nm laser line. Pearson's correlation coefficient (R) analysis, reference: AuNS@NBSH@CHTS. The white star points to the location of the high-scoring Pearson's R spectrum appointed in sections (b). The dashed white circle pinpoints the location of the mapped microbead, otherwise difficult to see in this figure. b) High-scoring Pearson's R spectrum (R≃0.90) compared to AuNS@NBSH@CHTS reference spectrum.

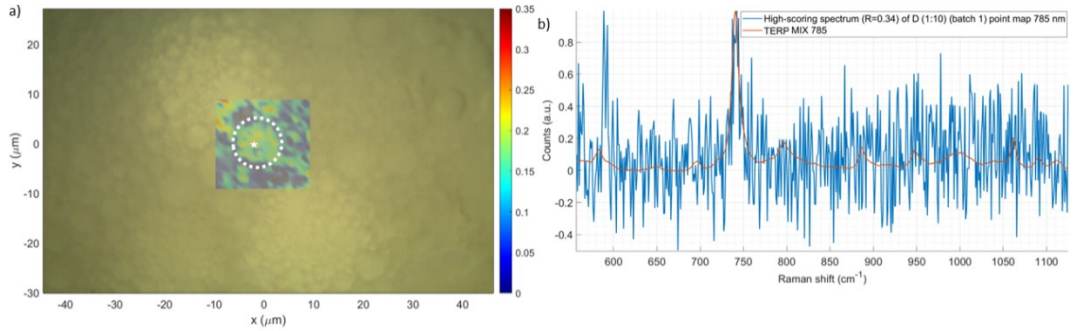

Figure 4.36. a) 2D Raman map of formulation D (1:10), 785 nm laser line. Pearson's correlation coefficient (R) analysis, reference: terpenoids mixture. The mapped microbead is the same as the one represented in the previous figure. The white star points to the location of the high-scoring Pearson's R spectrum appointed in sections (b). The dashed white circle pinpoints the location of the mapped microbead, otherwise difficult to see in this figure. b) High-scoring Pearson's R spectrum (R≃0.34) compared to terpenoids mixture reference spectrum.

4.2.3 3D Raman maps

The 2D Raman maps presented above reported about the coexistence of both the terpenoids mixture and the AuNS@NBSH@CHTS nanostructures in formulation D, also suggesting the latter being preferentially located at the edges of the microbeads. On the other hand, the TEM inspection reported in **Fig. 4.13** resulted in the presence of the AuNS@NBSH@CHTS in correspondence of what was attributed to the low contrast 2D projection of the beads. The following analysis, namely 3D confocal micro-Raman mapping, is expected to shed light on the relative arrangement of terpenoids and AuNS@NBSH@CHTS in formulation D. The main advantage of this technique is the ability to map a relatively large portion of sample volume, allowing for the investigation of multiple layers by moving alongside the *z* axis. By these means, one can discern the true spatial location of AuNS@NBSH@CHTS within the microbeads in formulation D. The statistical analysis is analogous to that of the 2D maps and was carried out using Pearson's correlation coefficient analysis. The reconstructed 3D volumes were therefore obtained by shaping isosurfaces enclosing the spectra which resulted in R-values above a determined threshold for each of the investigated species. Therefore, colored 3D shapes are visible within the 3D maps: these shapes indicate all points whose corresponding Raman spectrum is trustfully ascribed to the terpenoids mixture, as well as to the AuNS@NBSH@CHTS.

Figure 4.37 shows the results of the 3D Raman map of a microbead from formulation D obtained by using the 785 nm laser line. The optical microscope image is superimposed to the 3D

map under the bottom layer, and the contours of the beads are highlighted in green for clarity. Although the internal volume does not appear continuous, a clear higher concentration of red isosurfaces is visibly located within the core of the microbead, representing spectra with high correspondence to the terpenoid mixture (**Figure 4.37.a**). Similarly, several volumes colored in blue, ascribed to AuNS@NBSH@CHTS, are present in the surroundings of the mapped bead (**Figure 4.37.b**) and well recall the inhomogeneous distribution of the nanostructures already appreciated by TEM analysis (**Figure 4.13**). The sideview (**Figure 4.37.b**) allows to determine that the height of the microbead (~10 μm) is indeed smaller than the diameter upon the *xy* plane (~20 μm). This may be due to the settling of the microbead on the bottom of the microscope glass.

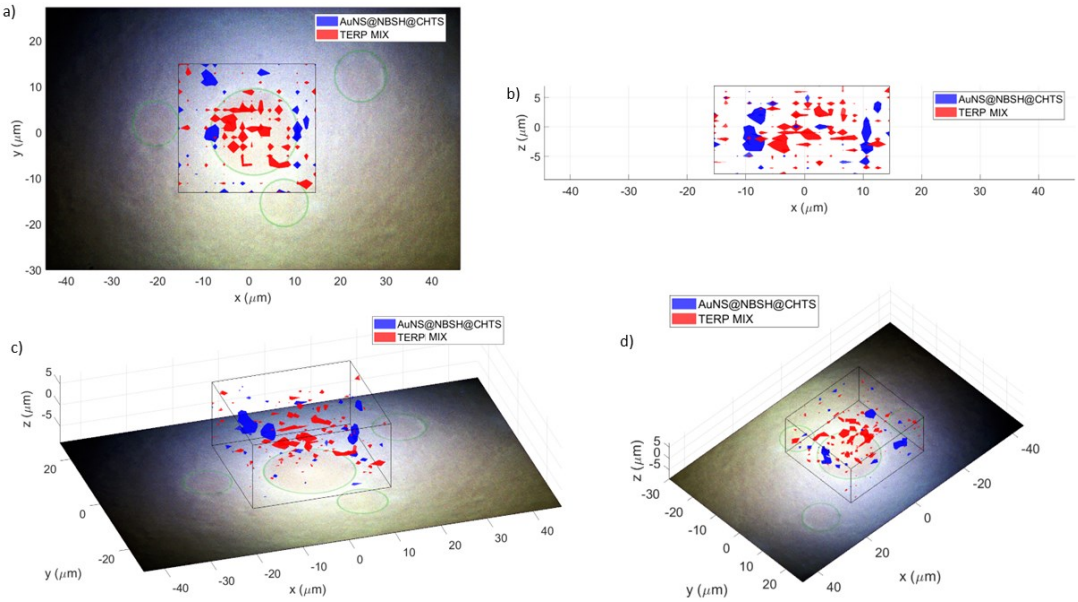

Figure 4.37. 3D Raman map of a microbead of formulation D, 785 nm laser line, shown from different perspectives: a) from the top, b) from the front side, c) from the upper-left front angle and d) from the upper-right back angle. Green circles in the image highlight the position of the microbeads, otherwise not very intelligible. The colored spots indicate the location of the Raman spectra with a value for the Pearson's R correlation coefficient greater than or equal to 0.50 for the AuNSs (blue spots) and 0.23 for the terpenoids mixture (red spots).

It is worth noting that the two species, namely the terpenoid mixture and AuNS@NBSH@CHTS, have opposite performances when analyzed at 633 instead of at 785 nm. While the first comes in higher signals at 633 nm, the AuNS@NBSH@CHTS nanostructures appear clearer when inspected at 785 nm. For that reason, and in order to provide a better 3D reconstruction, a second run of confocal Raman mapping was performed, in which the same bead from formulation D was first inspected using the 633 nm, and then by the 785 nm laser line.

Figure 4.38 shows the 3D Raman map of formulation D acquired by using the 633 nm laser line. A good localization of both the active principle and the AuNSs is achieved. While the diameter

of the mapped microbead appears to be similar in size to the one of the previous maps (~20 μm), its height appears to be about 4 μm, as shown by **Figure 4.38.b**.

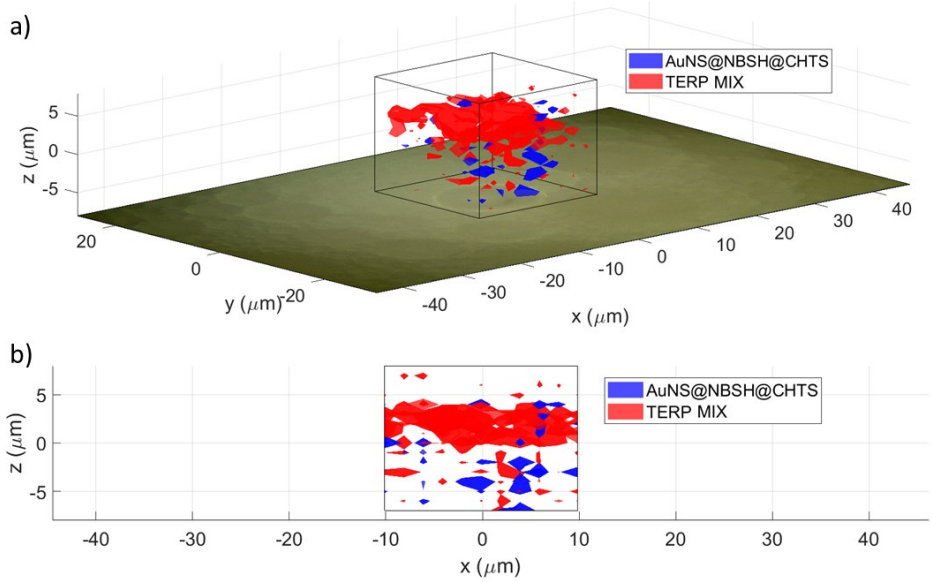

Figure 4.38. 3D Raman map of a microbead of formulation D, 633 nm laser line, shown from different perspectives: a) from the front, b) from the side. The colored spots indicate the location of the Raman spectra with a value for the Pearson's R correlation coefficient greater than or equal to 0.3 for the AuNSs (blue spots) and 0.23 for the terpenoids mixture (red spots).

Figure 4.39 shows the 3D Raman map of the same microbead of formulation D acquired by using the 785 nm laser line. Even though the microbead is the same as the one shown in **Figure 4.38**, its height is closer to ~10 μm rather than to 4 μm. This may be due to the larger confocal volume (*i.e.*, the laser spot) of the 785 nm laser line, in respect to the 633 nm, according to the already mentioned Rayleigh criterion (**Section 2.2.1**). As before, however, the active principle resulted well localized at the core of the microbeads, while the AuNSs contributions appear to be arranged outside the core of the microbead. The fact that the signals from the AuNS@NBSH@CHTS do not build a close shell around the bead must not surprise, as the TEM images (**Fig. 4.13**) already suggested an incomplete coverage. The quantity of nanostructures used to produce formulation D may be subjected to optimization in order to completely cover the surface of all the microbeads in a satisfactory and continuous manner. However, this was outside of the scope of the present study, at least at this stage.

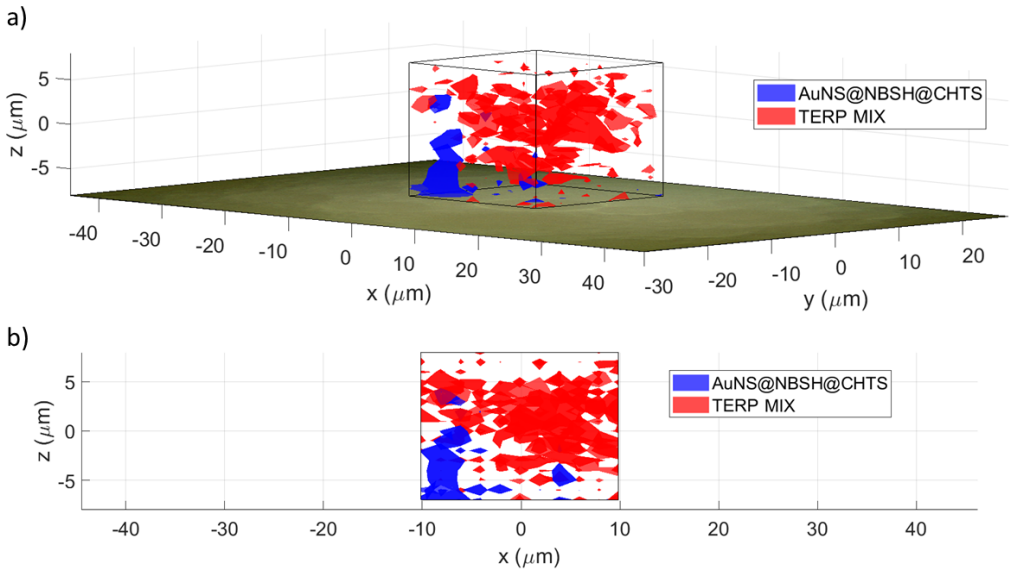

Figure 4.39. 3D Raman map of a microbead of formulation D, 785 nm laser line, shown from different perspectives: a) from the front, b) from the side. The colored spots indicate the location of the Raman spectra with a value for the Pearson's R correlation coefficient greater than or equal to 0.5 for the AuNSs (blue spots) and 0.19 for the terpenoids mixture (red spots).

Figure 4.40 shows the combined results for the localization of the terpenoids mixture from the abovementioned 3D Raman maps, both the 633 nm and the 785 nm one. The results from both laser lines appear to be in agreement with each other, localizing the active principle preferentially in the core of the microbead.

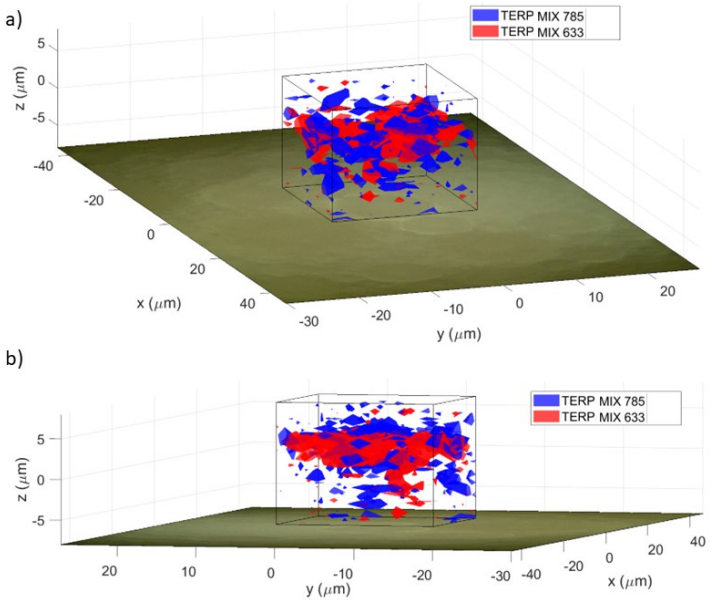

Figure 4.40. Mixed 3D Raman map of a microbead of formulation D, acquired using both the 633 and the 785 nm laser lines subsequently. The colored spots indicate the location of the Raman spectra with a value for the Pearson's R correlation coefficient greater than or equal to 0.2 for the terpenoids mixture acquired with the 785 nm laser line (blue spots) and 0.22 for the terpenoids mix acquired with the 633 nm laser line (red spots).

Figure 4.41 shows the combined results for the localization of AuNS@NBSH@CHTS from the above-mentioned 3D Raman maps, both the 633 nm and the 785 nm one. As before, there is an agreement between the two laser lines: the AuNSs contributions are both localized outside the microbead's core. However, there is a poor coincidence between the positions of the signals relating to the nanostars, as one might have expected. This may be due to the motion of the microbead, and its components, in the period between the beginning of the acquisition of the first map and the end of the acquisition of the second map, as they were acquired one after the other along the span of about 24 consecutive hours. It should be recalled that the microbead shell is not covalently attached to the core, nor the molecules and nanostructures that constitute the shell are bounded between themselves. This causes the shell to behave in a fluid-like manner, and the nanostructures within it are subjected to move in time as well. It should also be recalled that the resolving power given by the 785 nm laser line is smaller than the one of the 633 nm laser line, explaining why the AuNSs locations resulting from the 785 nm excitation (blue spots in **Fig. 4.41**) are larger the ones resulting from the 633 nm one (red spots in the same figure).

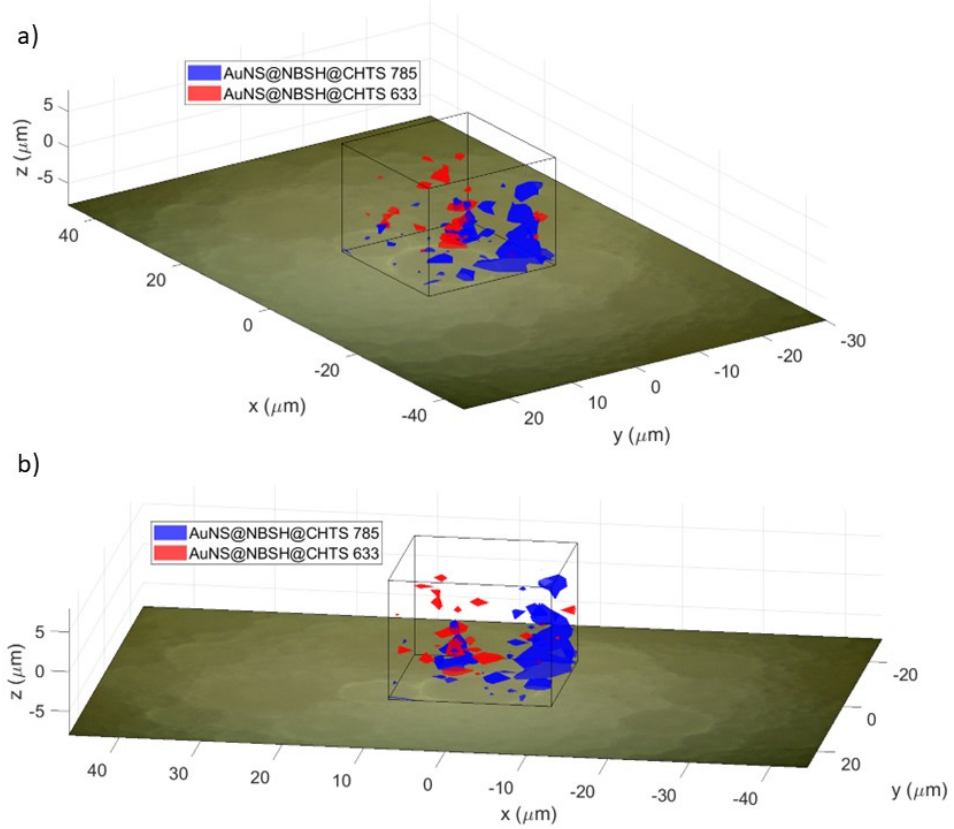

Figure 4.41. Mixed 3D Raman map of a microbead of formulation D, acquired using both the 633 and the 785 nm laser lines subsequently. The colored spots indicate the location of the Raman spectra with a value for the Pearson's R correlation coefficient greater than or equal to 0.2 for the AuNS@NBSH@CHTS acquired with the 785 nm laser line (blue spots) and 0.22 for the AuNS@NBSH@CHTS acquired with the 633 nm laser line (red spots).

4.3 Characterization of the formulations after the photodegradation process

To check the stability of the four formulations under UV irradiation, they have been continuously subjected to UV light (365 nm, 4 W) for a week (168.0 h), following the photodegradation protocol described by Luiz de Oliveira *et al.* [33] In their study, the authors used an irradiance setup similar to the one used in this thesis, while the characterization was driven exclusively by analyzing the terpenoids through HPLC means. They concluded that geraniol, when encapsulated in chitosan/arabic gum microcapsules, increases its half-life ($t_{50\%}$), and thus its resistance to UV-light photoinduced degradation, by 18.5 times. Specifically, the $t_{50\%}$ increased from 4.2±0.1 hours for emulsified geraniol to 74.1±0.4 hours for encapsulated geraniol. With respect to Luiz de Oliveira *et al.*, the photodegradation process was herein followed by Raman mapping characterization, similarly to what was already done for the formulations prior to the photodegradation (**Section 4.2**). In addition, their formulations contained only geraniol, unlike the ones herein studied, containing the mixture of the three terpenoids of interest. Indeed, the process herein implemented turned out to be more complicated, because both the terpenoids and the structures of microbeads have been damaged during the photodegradation process. The subsequent analysis, either by Raman spectroscopy or qualitative observations, attempts to shed light on all the variables observed before and after the photodegradation.

The most apparent change after the photodegradation process is the phase separation of the formulations, which is visible by the naked eye (**Figure 4.42**). The number and characteristics of the phases in which the formulations separated depended on their composition. A comparison between the formulations after degradation in the presence of UV light (**Fig. 4.42.b**) and in the absence of light (**Fig. 4.42.c**), whilst maintaining the other experimental conditions (t=168.0 h, T_{amb}, cuvettes sealed with parafilm), allows for a better appreciation of the changes due to photodegradation. Specifically, a distinct yellow color of the floating phases – opaque and milky in formulations B and C, transparent in formulations A and D – can be observed in the photodegraded samples. The same is much less pronounced in the transparent floating phases of samples aged in absence of light. In contrast, the opaque, milky yellow staining is absent in these samples. The phase separation is still somehow similar across the sample series under UV-light, and dark, conditions.

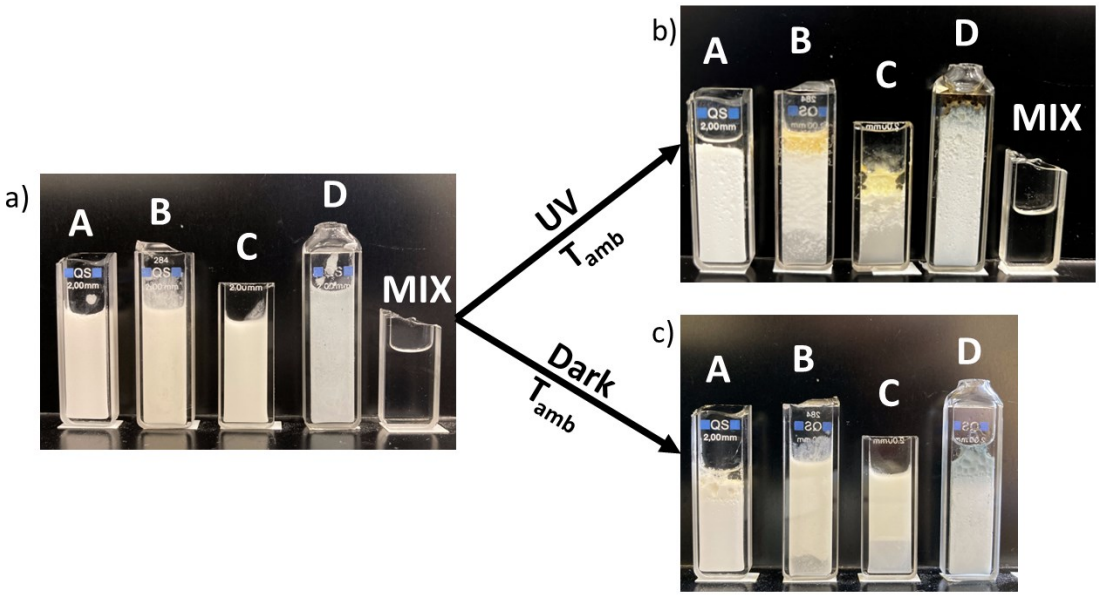

Figure 4.42. The formulations before (a) and after (b) the UV light irradiation process. In addition, a photo of the formulations after one week of degradation conducted in the absence of UV radiation (storage in the dark) at room temperature (c) is shown. The mixture of terpenes is absent since the sample in our possession was finished.

To better appreciate the bluish coloration of the D formulation, along with the changes it underwent during degradation both in the presence and absence of UV light, **Figure 4.43** shows the said formulation on a white background.

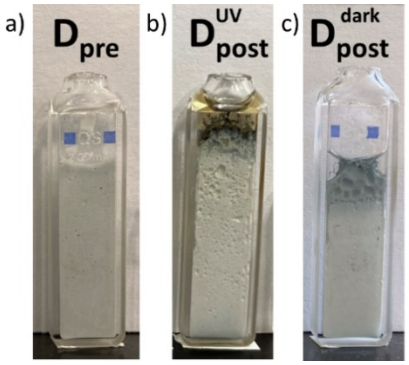

Figure 4.43. Pictures of formulation D before (a), after the photodegradation process (b) and after the degradation in absence of light (c). A similar phase separation after the degradation can be observed, while the coloration of the floating transparent phase is more pronounced for the photodegradation condition.

Figure 4.44 shows in detail the characteristics of the different phases after the photodegradation process, along with the nomenclature of said phases.

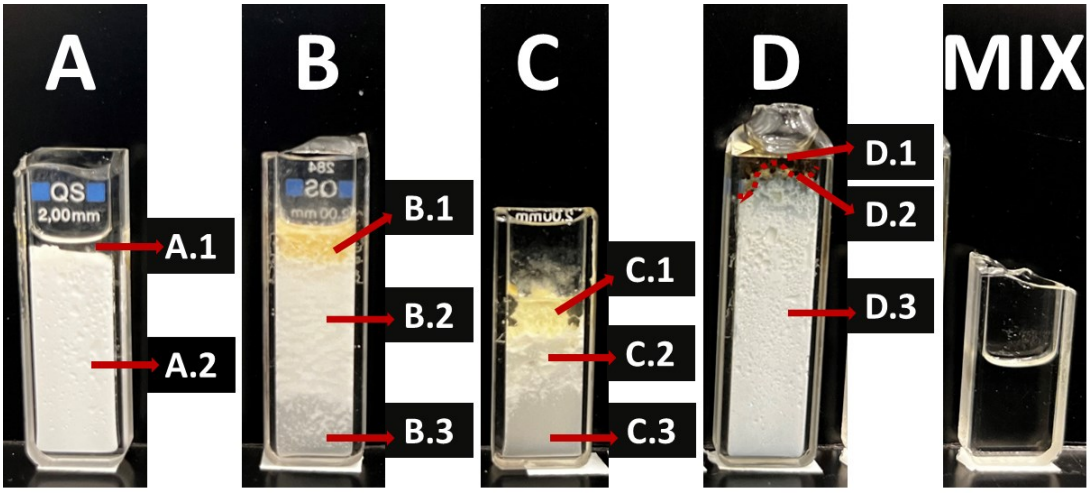

Figure 4.44. Detailed view of the different phases in which the formulations have separated after the UV light irradiation. Their nomenclature is also reported by red arrows

Simple, qualitative tests were performed to check the phase separation of the main different components (**Figure 4.45**). Handbooks report the following densities: 0.92 g/cm^3 for AMD 10, 0.89 g/cm^3 for geraniol and 1.07 g/cm^3 for eugenol. Therefore, the following blends were also checked:

- water and AMD 10 (**Figure 4.45.a**)
- water and eugenol (**Figure 4.45.b**)
- water and geraniol (**Figure 4.45.c**)
- water and geraniol/eugenol 2:1 mixture (**Figure 4.45.d**)

The blends were shaken by hand and left to coalesce for one day. Thymol, being solid at room temperature, has not been considered for these tests, also considering that it dissolves in the oil phase consisting of the mixture of the other terpenoids (*i.e.*, geraniol and eugenol, 2:1). The result obtained for the mixture of eugenol and geraniol in water (**Figure 4.45.d**) is of particular interest. In fact, the deposition on the bottom of the solution of the yellow-colored phase of eugenol (yellow because it was aged eugenol, as better discussed in the following), and on top of the solution of the colorless phase of geraniol, were observed before agitation. After agitation and subsequent coalescence, a breakdown of the solution again into three phases was again observed, with the aqueous phase in the middle, but this time both the organic phases had a yellowish color. This can be rationalized by considering some degree of mixing between the eugenol (yellowish) and geraniol, which remains even after coalescence. However, it must be remembered that eugenol, at the beginning of the thesis work, did not present a yellowish tint but was colorless. Indeed, while conducting these tests, it was observed that the eugenol sample, despite being kept in the dark and refrigerated throughout the duration of the thesis work, underwent a yellowing process, as evidenced by **Figure 4.46**.

The results of the coalescence experiments will be very useful in explaining some phenomena observed following the spectroscopic analysis of the phases, as will be presented later.

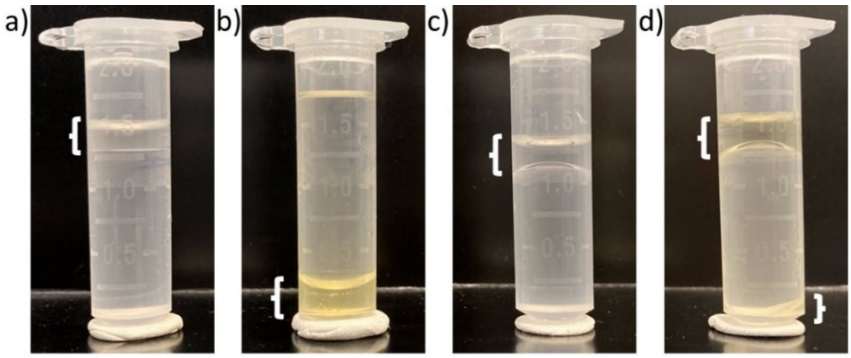

Figure 4.45. Results of the coalescence experiments of water and AMD 10 (a), water and eugenol (b), water and geraniol (c) and water and geraniol/eugenol 2:1 mixture (d) blends. The white brackets highlight the organic phases, otherwise difficult to discern in some cases.

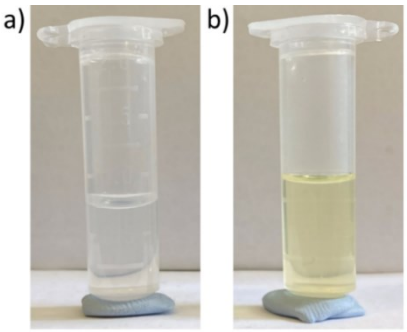

Figure 4.46. Pictures of fresh eugenol (a) and eugenol aged in the dark and in the refrigerator (b).

Raman analysis of fresh (colorless) and aged (yellowish) eugenol returned no significant difference, neither in relative intensities nor for peak position. **Figure 4.47** shows the comparison between the two spectra.

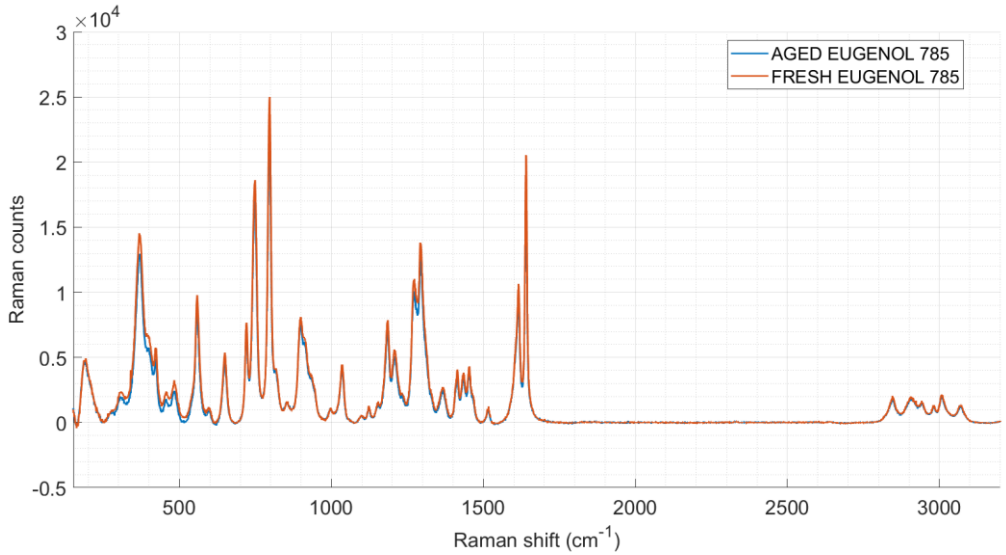

Figure 4.47. Comparison between Raman spectra of fresh (colorless) and aged (yellowish) eugenol.

To better understand the phase separation of formulations subject to photodegradation, each phase was analyzed by Raman spectroscopy directly through the cuvettes. At least three different Raman spectra were acquired at low optical magnification (10x) to sample a larger volume of solution and thus increase the representativeness of the measurements by averaging the obtained results. Furthermore, detailed spectra of formulations that still presented the microbeads were acquired to assess whether, and to what extent, the active ingredients were still present in their core. The next chapters show the results for each formulation in detail.

4.3.1 Photodegradation of formulation A: results

The low optical magnification (10x) Raman spectra of phases 1 and 2 of formulation A post-degradation are shown by **Figure 4.48**.

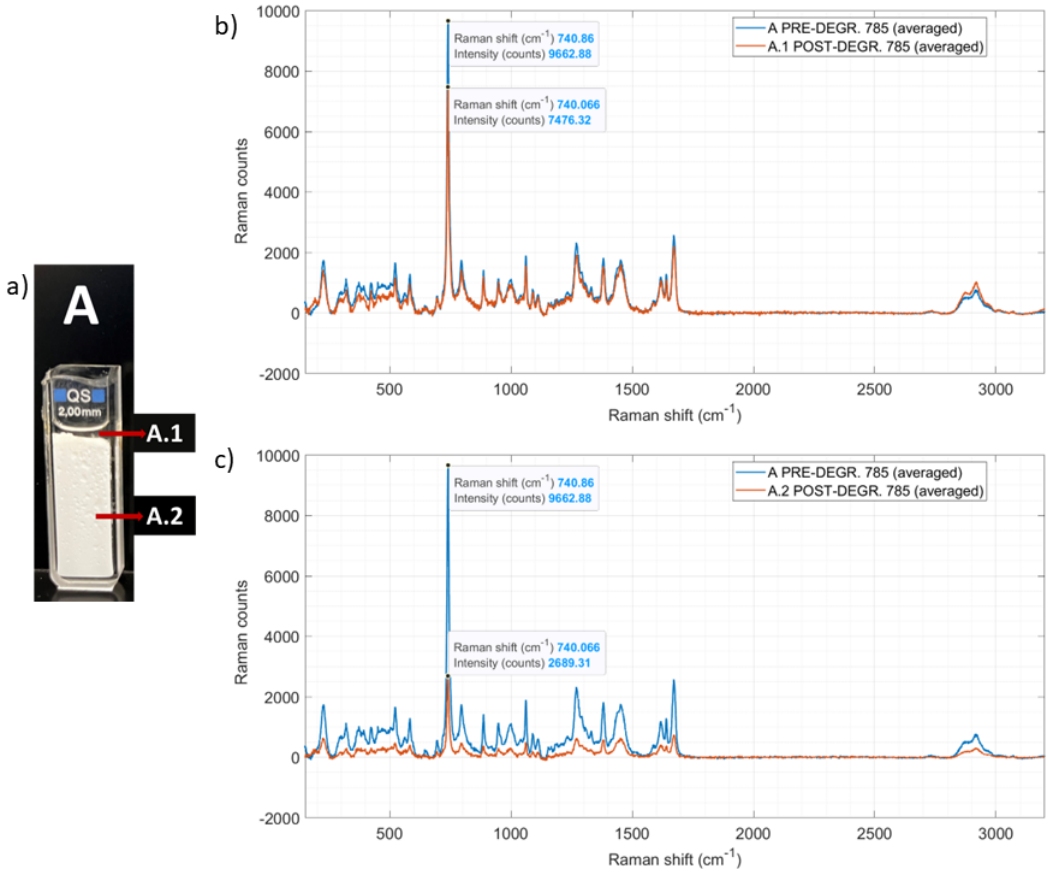

Figure 4.48. Picture of formulation A after degradation (a). Raman spectra of phases A.1 (orange) (b) and A.2 (orange) (c) compared to the Raman spectrum of formulation A before degradation (blue) (b, c); 785 nm excitation. The data tips highlight the Raman shift and absolute intensity of the thymol peak, diagnostic of the overall terpenoids mixture.

The most noticeable change is a decrease in the overall absolute intensities of phases A.1 and A.2 spectra, compared to the spectrum of formulation A acquired before degradation (under

the same measuring conditions). In addition, the spectrum of A.1 is more intense than that of A.2. This last finding can be rationalized by a phase separation due to the natural process of micelle coalescence. The oil phase containing the mixture of the three terpenoids migrated to the surface, being less dense than water, giving rise to phase A.1. This phase is thus richer in terpenoid mixture than phase A.2, which still contains some amount of terpenoids, but also water and soybean lecithin. This decreases their local concentration, resulting in the lower absolute intensities observed for this phase. Phase A.2 is thus probably composed of macroscopic lecithin formations, given also its visual reminiscence to the solution that was obtained after adding soybean lecithin to water, before proceeding with emulsification using the homogenizer (refer to **Section 3.2.3**). These macroscopic formations would then give rise to the scattering of ambient light, giving the A.2 phase its characteristic opalescent white appearance.

The degradation process used in this thesis work did not produce any visible change in the Raman peaks of formulation A, except for the appearance of a very low-intensity peak localized at 192 cm^{-1}, shown in detail by **Figure 4.49**. This peak is visible in both A.1 and A.2 phases. Unfortunately, even if clear and recursive along the UV-irradiated formulation series, this contribution at very low Raman shift remains un-attributed.

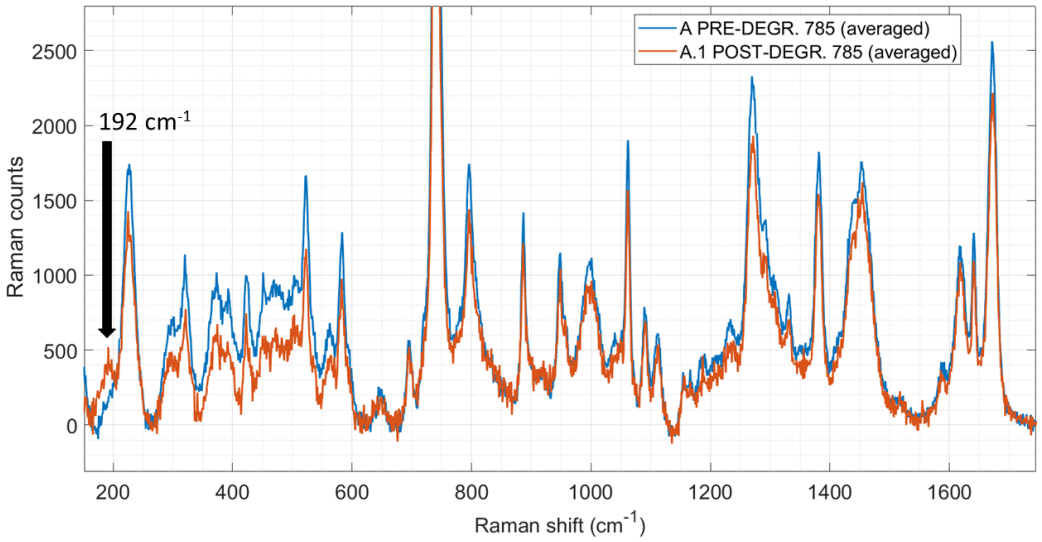

Figure 4.49. Enlargement of the Raman spectrum of phase A.1, compared to the non-degraded formulation A spectrum. The black arrow points to the location of the abovementioned peak located at 192 cm^{-1}, the only peak different in position from the pre-degradation situation.

A comparison of the normalized spectra of phases A.1 and A.2 with that of the reference mixture makes it possible to assess whether there have been enrichments or depletions of any of the three terpenoids within the analyzed phase. It was chosen to perform the comparison with the reference spectrum of the terpenoid mixture and not that of the pre-degradation formulation A because it was observed that the contributions of lecithin are not detectable. With this

comparison it was thus also possible to attribute the presence of the terpenoids in phases A.1 and A.2. **Figure 4.50** displays said comparison. Specifically, there is an increase in peak intensity at 192 cm^{-1}, regarding the spectrum of phase A.2 when compared with that of A.1. In fact, we go from a percentage intensity of about 7 percent, relative to the spectrum of A.1, to about 12 percent of that of A.2.

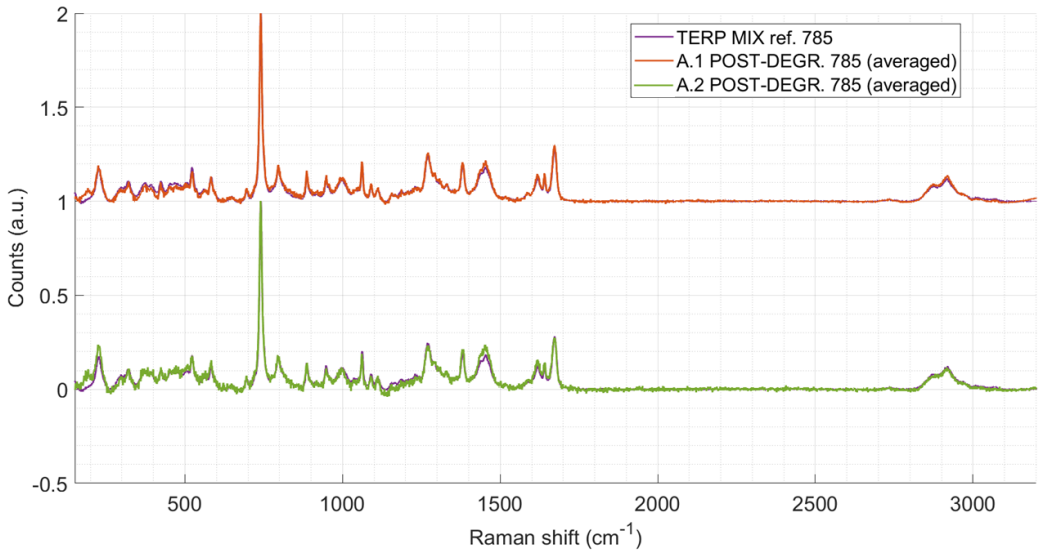

Figure 4.50. Comparison between the terpenoids reference mixture and the spectra of A.1 and A.2, all normalized.

Figure 4.51 shows the averaged Raman spectrum of phase A.2, compared to the terpenoids mixture reference spectrum, acquired at high optical magnification. Its spectrum was acquired because, due to the milky, opalescent appearance of the said phase, the presence of micelles was assumed in phase A.2. This hypothesis was refuted by the inspection under the optical microscope, as shown in **Figure 4.51.a**. This is probably due to the absence of chitosan in solution, which would have given a greater degree of stabilization to the micelles. In fact, the chitosan-containing formulations have not undergone a complete phase-separation process, as it will be shown in the next paragraphs. Nevertheless, the characteristic thymol peak at 741 cm^{-1}, also diagnostic of the presence of the terpene mixture, is still present (**Fig. 4.51.b**), in agreement with what had been observed from the spectrum acquired at low magnification of phase A.2 (**Fig. 4.48.c**). Its absolute intensity under the same acquisition conditions (acquisition time, laser intensity) is much lower than that of the reference spectrum, indicating a lower quantity of active principle in the same sampled volume, confirming the smaller local concentration of the active principles in said phase given by their migration towards the surface of the solution (phase A.1).

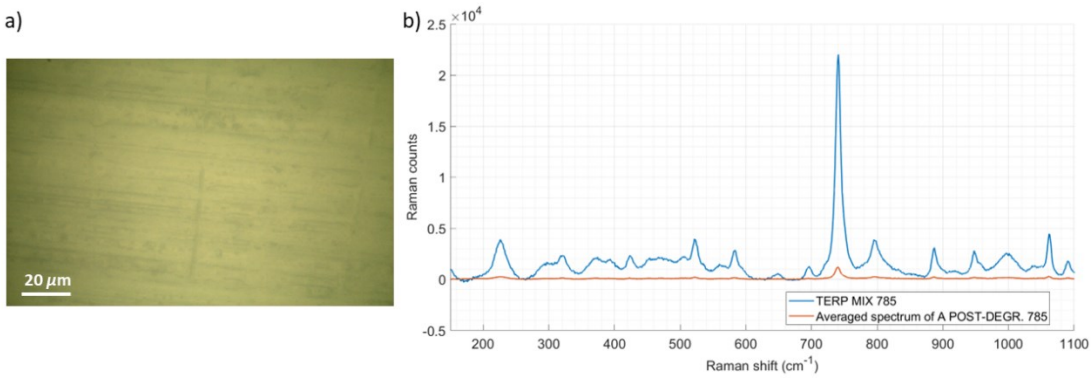

Figure 4.51. a) 50x zoom magnification image of phase A.2 after irradiation. No micelles are visible. b) Averaged (n=3) Raman spectrum of phase A.2 after irradiation, 785 nm laser line, compared to the terpenoids mixture reference spectrum.

4.3.2 Photodegradation of formulation B: results

Figure 4.52 shows the Raman spectra of phases B.1, B.2 and B.3, obtained after the UV irradiation of formulation B.

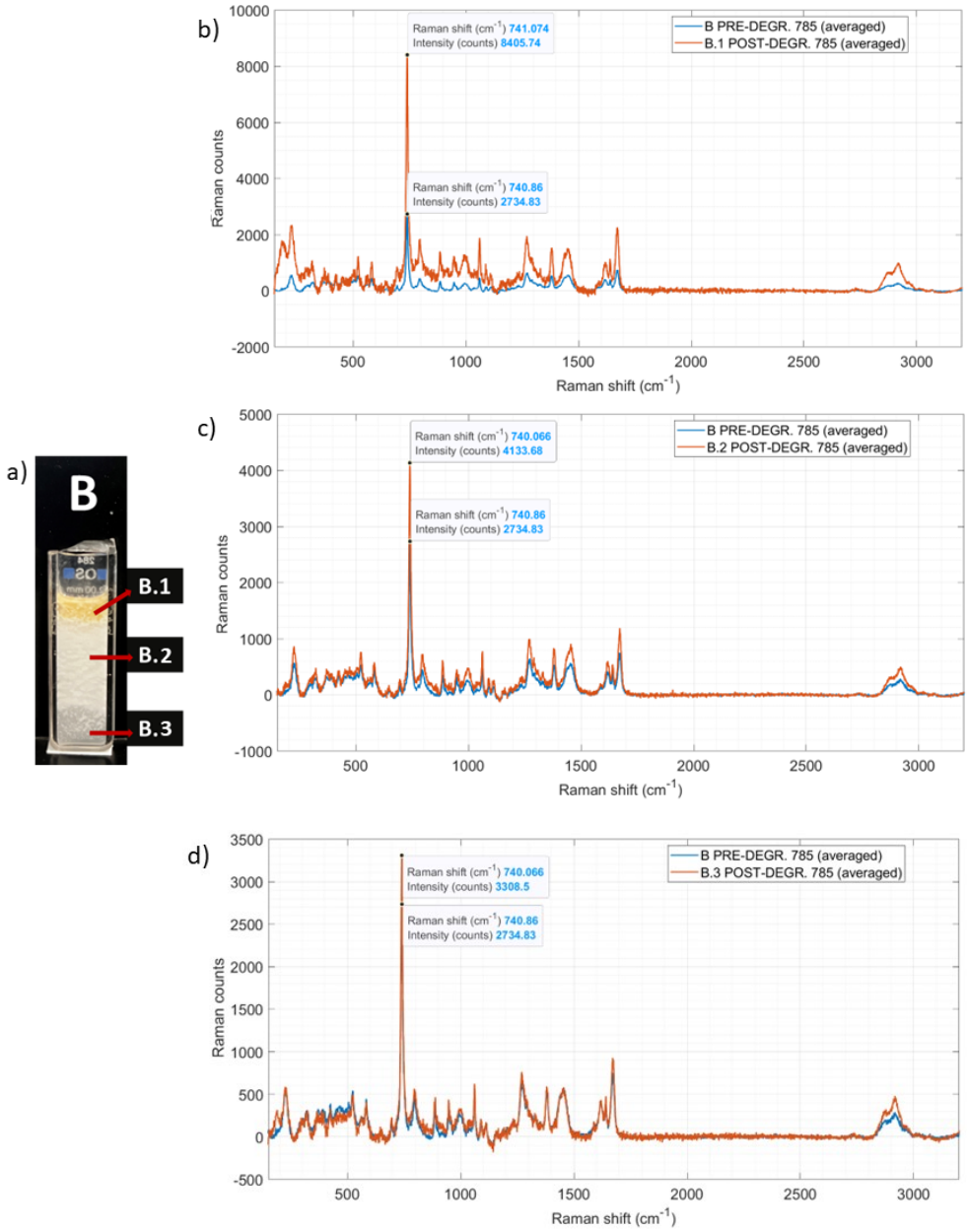

Figure 4.52. Picture of formulation B after degradation (a). Raman spectra of phases B.1 (orange) (b), B.2 (orange) (c) and B.3 (orange) (d) compared to the Raman spectrum of formulation B before degradation (blue) (b, c, d); 785 nm excitation. The data tips highlight the Raman shift and absolute intensity of the thymol peak, diagnostic of the overall terpenoids mixture.

One can first observe an increase in the absolute intensity of the peaks related to the terpenoid mixture in phases B.1, B.2, an B.3, compared with the averaged spectrum of the B formulation before degradation. Furthermore, the trend is increasing when passing from phase B.3 to B.1, *i.e.*, as the height of the solution increases. This finding is consistent with what was

already observed for degraded formulation A, *i.e.*, the migration of the terpenoid mixture upward in solution, as it is overall less dense than water. Thus, there is a concentration gradient that increases as the acquisition height of the Raman spectra along the cuvette increases as well. The absolute intensity of terpenoid peaks, greater than that observed for the averaged spectrum of the pre-degradation sample, should not be surprising: in fact, the coalescence of the phases increases the local concentration of terpenoids especially in the B.1 and B.2 phases, and this is reflected in the intensity of the Raman peaks.

As with formulation A, a direct comparison of the normalized spectra of the B phases after degradation and the terpenoids mixture reference helps to understand whether enrichment or depletion has occurred concerning one or more compounds within the formulation. **Figure 4.53** shows this comparison. As in the previous case, the low-frequency peak located at 192 cm^{-1} results as the only clear difference between pre- and post-degradation. The relative intensity of this peak changes depending on which phase is considered: 21% for phase B.1, 5% for phase B.2 and 10% for phase B.3, considered in respect to the base peak. A greater relative intensity corresponds, as already mentioned, to a greater local concentration, in this case in phases B.1 and B.3 compared to the central phase B.2. Unfortunately, as mentioned before, there is no clear attribution as far as this weak peak is concerned.

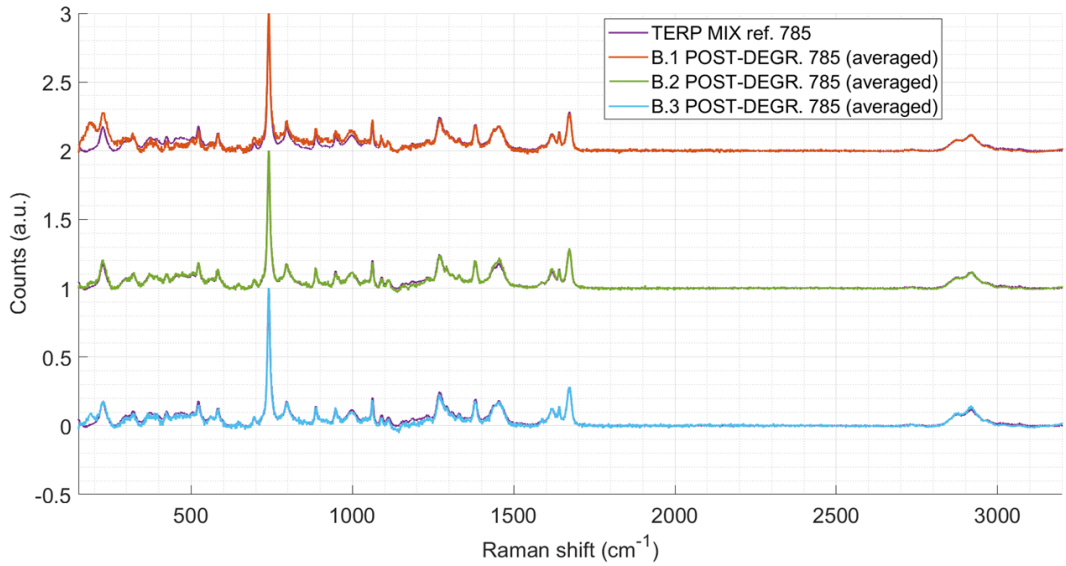

Figure 4.53. Comparison between the terpenoids reference mixture and the spectra of B.1, B.2 and B.3, all normalized.

Figure 4.54 shows the averaged spectrum of three microbeads belonging to phase B.2, that is the phase mostly similar to the pre-degradation condition from the macroscopic point of view. This spectrum is compared with the spectrum of beads of similar dimensions from formulation B before the degradation, the acquisition conditions being the same. A decrease in the absolute

intensity of the thymol peak, diagnostic of the whole terpenoid mixture, is therefore observed if compared to the spectrum of the pre-degradation condition. As for phase A.2, this would suggest the release of the active principle and its migration to the solution, particularly towards the top of the solution, as confirmed by the low magnification Raman spectra (**Fig. 4.52**).

Contrary to what was found for phase A.2, the microbeads are still present in phase B.2 even after the degradation process, as supported by **Figure 4.54.a**. By analyzing the absolute intensity of the peak at 741 cm^{-1} and comparing it with the same value obtained for phase A.2, one can observe an increasing trend: there is a transition from 1220 Raman counts for phase A.2 to 2322 Raman counts for phase B.2. This fact would indicate a higher local concentration of the active principle in the sampled volume, *i.e.*, in the core of the survived microbeads of phase B.2.

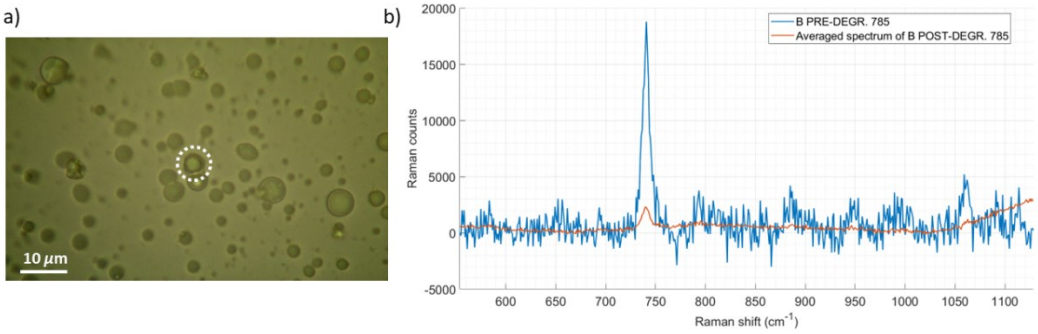

Figure 4.54. a) 100x zoom magnification image of phase B.2 after irradiation. b) Averaged (n=3) Raman spectrum of microbeads from phase B.2, after degradation (orange), compared to the spectrum of a bead of similar dimensions from formulation B, before degradation (blue).

4.3.3 Photodegradation of formulation C: results

Figure 4.55 shows the Raman spectra of phases C.1, C.2 and C.3, obtained after the UV irradiation of formulation C. The results are somewhat similar to the ones found for formulation B in the previous chapter. A progression in the Raman signal absolute intensities is observable, starting from the bottom phase (C.3) towards the floating one (C.1). As stated before, this is compatible with the migration of the active principles towards the top of the solution as a result of their density. In addition to the previous cases, it is also possible to observe the spectral contribution of AMD 10, present only from formulation C onwards. The absolute intensities of its characteristic signals (1303, 1440 and 2855 cm^{-1}) are also increasing from C.3 towards C.1, in agreement with the results of the coalescence experiments (**Fig. 4.45**), which saw the phase of AMD 10 floating on the aqueous one because of its lower density (0.92 g/cm^3).

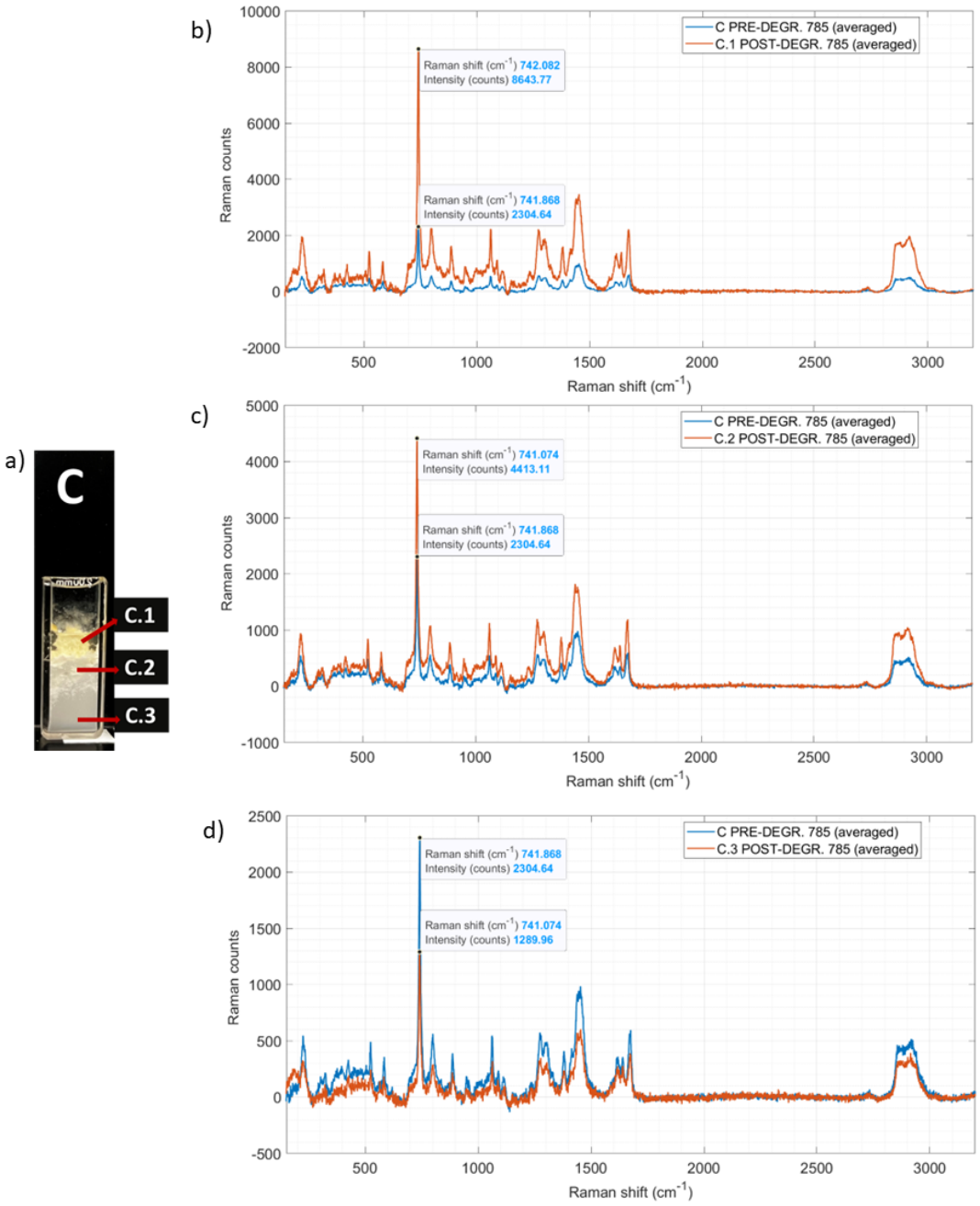

Figure 4.55. Picture of formulation C after degradation (a). Raman spectra of phases C.1 (orange) (b), C.2 (orange) (c) and C.3 (orange) (d) compared to the Raman spectrum of formulation C before degradation (blue) (b, c, d); 785 nm excitation. The data tips highlight the Raman shift and absolute intensity of the thymol peak, diagnostic of the overall terpenoids mixture.

Figure 4.56 shows the direct comparison of the normalized spectra of the C phases after degradation, to better assess whether or not there has been enrichment of any component. Unlike the previous cases, the comparison is performed with the averaged spectrum composed of the contributions of both the terpenoids mixture and AMD 10, and not with that of the terpenoids mixture reference only. This is to better control changes in the contribution of AMD 10. The comparison with this spectrum is legitimate: in fact, it has been ascertained that the contribution

of other components beyond terpenoids and AMD 10 is not detectable. As in the case of formulation A and B, an increase in relative peak intensity can be observed at 192 cm^{-1}. Also, as with B, this increase is more pronounced for the floating (C.1) and bottom (C.3) phases, while no such peak formation is observed for the central aqueous phase. In contrast to formulation B, however, the relative increase of such a peak is greater for the C.3 than for the C.1 phase: it goes from a relative peak intensity of 19% related to the C.3 phase, to 8% for the C.1 phase.

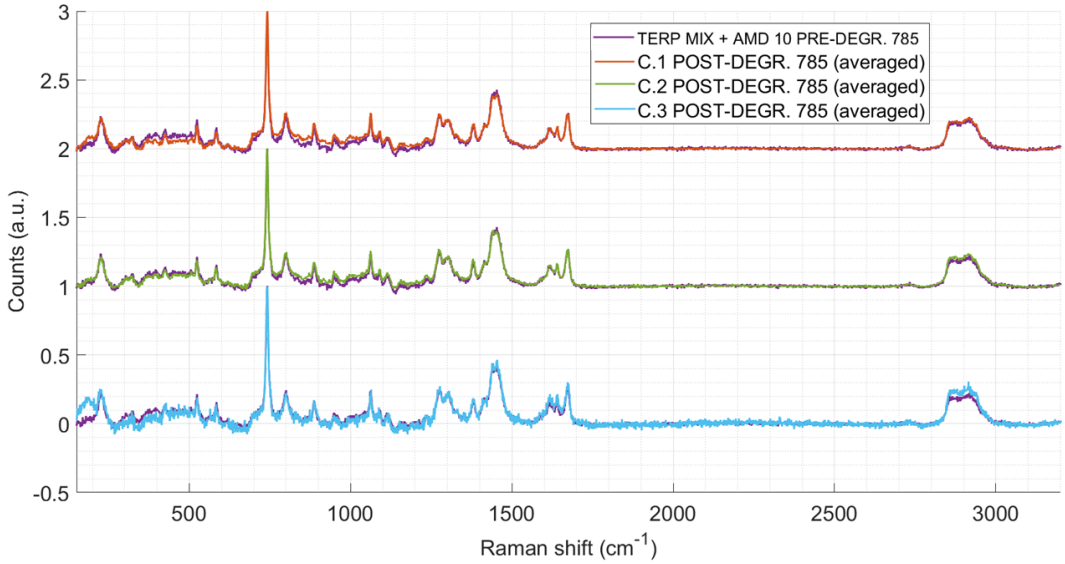

Figure 4.56. Comparison between the C pre-degradation spectrum and the spectra of C.1, C.2 and C.3, all normalized.

As with the previous formulations, **Figure 4.57** shows the averaged spectrum of three microbeads belonging to phase C.2, the most similar to the pre-degradation condition, as shown by its normalized spectrum in the previous figure (**Fig. 4.56**). The results are similar to the previous ones: the thymol peak at 741 cm^{-1}, diagnostic of the presence of the terpenoids mixture, is always present, and its absolute intensity appears to have decreased if compared to that of microbeads of similar dimensions from formulation C before the degradation (**Fig. 4.57.b**). In addition, its absolute intensity is found to have increased with respect to the case of B seen before. Specifically, the absolute intensities that peak go from 2322 Raman counts for the microbeads of B post-degradation to 3024 for the microbeads of C post-degradation, under the same acquisition conditions. This increasing trend concerns the amount of active ingredient present in the core of the microbeads after degradation. It could therefore indicate a greater degree of retention of the active ingredient, and thus more effective protection, by the microbeads of formulation C (with respect to formulations B and A) following UV-irradiation-induced degradation.

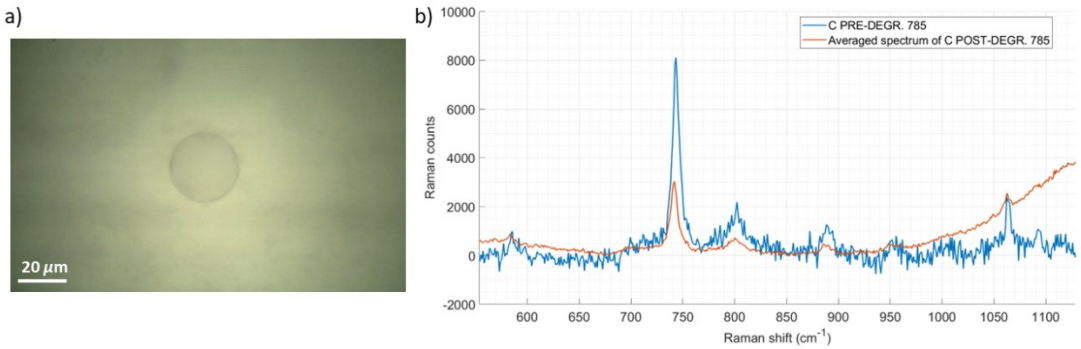

Figure 4.57. a) 50x zoom magnification image of phase C.2 after irradiation. b) Averaged (n=3) Raman spectrum of microbeads from phase C.2, after degradation (orange), compared to the spectrum of a bead of similar dimensions from formulation C, before degradation (blue).

A further characterization was carried out by 2D Raman maps means, as was done for pre-degradation microbeads (**Section 4.2.2**). **Figure 4.58** shows the results of such detailed analysis. A clear localization of the active principle inside the microbeads core is present. However, as seen in **Section 4.2.2** and contrary to the results of the detailed 2D Raman maps prior the photodegradation, the signals are much lower in intensity. This is also reflected on the Pearson's R-values for the dataset, which are particularly low (R≈0.30). However, this finding agrees with other experimental data obtained from previous measurements, reported in this chapter. In fact, the low scores obtained by Pearson's correlation coefficient analysis, resulting from a lower signal-to-noise ratio of the spectra in the dataset, are consistent with a lower presence of the active ingredients in the core of the microbeads, also evidenced by **Figure 4.57**.

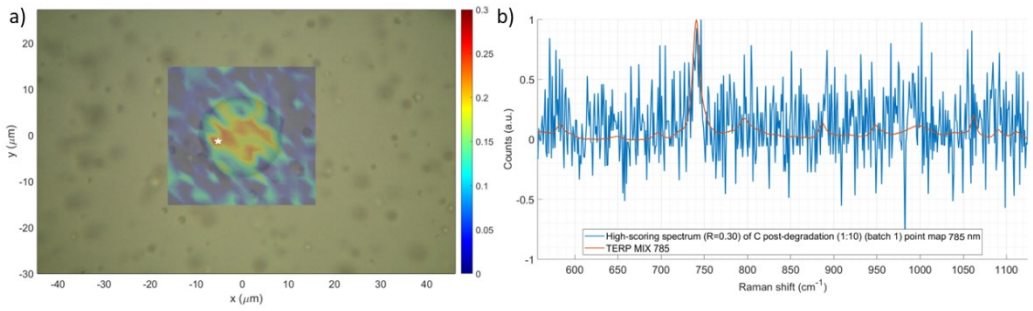

Figure 4.58. a) 2D Raman map of formulation C (1:10) post-degradation, 785 nm laser line. Pearson's correlation coefficient (R) analysis, reference: terpenes mix. The white star points to the location of the high-scoring Pearson's R spectrum appointed in section (b). b) High-scoring Pearson's R spectrum (R≃0.30) compared to terpenes mix reference spectrum.

4.3.4 Photodegradation of formulation D: results

Figure 4.59 shows the Raman spectra of phases D.1, D.2 and D.3, obtained after the UV irradiation of formulation D. Unlike the previous cases, the spectra appear more complicated to rationalize due to the AuNS@NBSH@CHTS contributions, diagnosed from the peak at 591 cm^{-1}. Nonetheless, two main phases can be observed, as in the case of formulation A (refer to **Section 4.3.1**), namely the floating phase D.1 and the underlying phase D.3. Also, there is a sort of interface between the two phases D.1 and D.3, which has been called D.2. The floating phase D.1 is composed only of active principle (mixture of terpenoids) and AMD 10, as will be shown later by comparison with the reference spectrum (**Figure 4.60**). From the spectrum of this phase, in fact, one can observe an increase in the absolute intensity of the diagnostic peak at 741 cm^{-1} of the terpenoids mixture, as well as the absence of the AuNS@NBSH@CHTS peak at 591 cm^{-1}. This agrees with the tendency of the terpenoid phase to migrate upwards of the solution, as could be observed for all the other formulations. It is also possible to note the absence of the peak at 192 cm^{-1}.

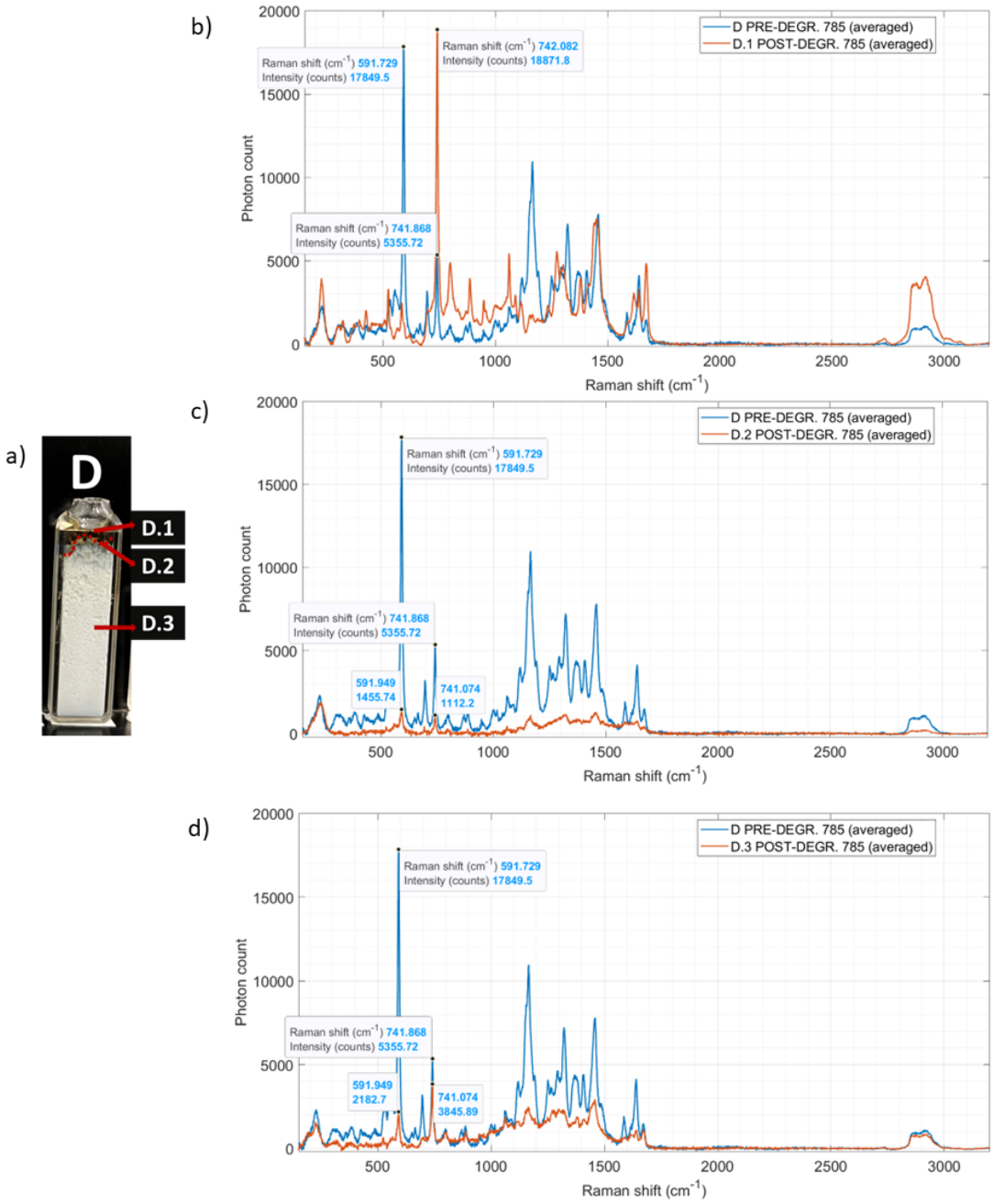

Figure 4.59. Picture of formulation D after degradation (a). Raman spectra of phases D.1 (orange) (b), D.2 (orange) (c) and D.3 (orange) (d) compared to the Raman spectrum of formulation D before degradation (blue) (b, c, d); 785 nm excitation. The data tips highlight the Raman shift and absolute intensity of the thymol peak, diagnostic of the overall terpenoids mixture, and of the AuNSs peak.

The 192 cm^{-1} peak is instead clearly visible in the averaged spectrum of phase D.3, with a relative intensity of 26%, as shown in **Fig. 4.60**. The averaged spectrum of phase D.3 also shows a decrease in the intensity of the terpenoids diagnostic peak, again in agreement with the hypothesis of their upward migration. Finally, the spectrum of D.3 shows a low, albeit significant, contribution from the signal at 591 cm^{-1} attributable to AuNSs capped with chitosan and Nile blue

A. This data would guarantee an important permanence of this component in the structure of the microbeads, specifically in the shell, as will be shown later with the aid of 2D Raman maps (**Figure 4.64**).

The peak at 591 cm^{-1} instead exceeds in absolute intensity the peak of the terpenoid mixture in the D.2 interface. This interface possesses dark colored agglomerates, reminiscent of AuNSs agglomerates that naturally form after prolonged storage of AuNSs solutions outside the refrigerator. An optical microscope image of one of these agglomerates present in interface D.2 is shown in **Figure 4.61**. The D.2 averaged spectrum, acquired focusing on these agglomerates, confirms a majority component of AuNS@NBSH@CHTS, although there is also a not negligible contribution from the terpenoid mixture. The large contribution at 231 cm^{-1} in the D.2 interface spectrum (in green in **Fig. 4.60**) is not easy to rationalize, since it belongs to the low energy zone of the Raman spectrum. On the other side, large differences in relative intensities in the area from 1000 to 1700 cm^{-1} in the spectra of D.2 and D.3 can be attributed to baseline aberrations, although baseline parameters do not vary between the different spectra.

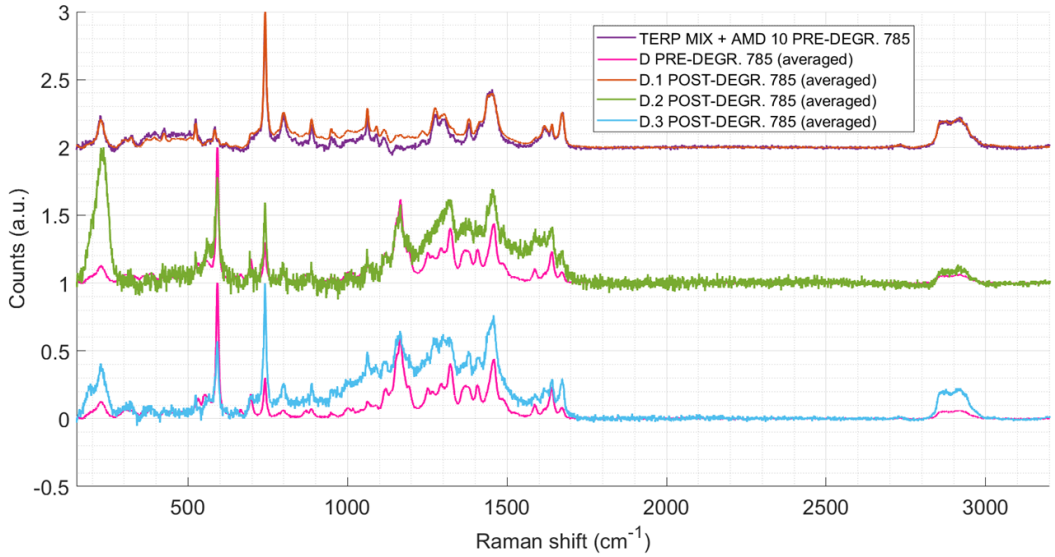

Figure 4.60. Comparison between reference spectra (terpenoids mixture and AMD 10, D pre-degradation) and the spectra of D.1, D.2 and D.3, all normalized.

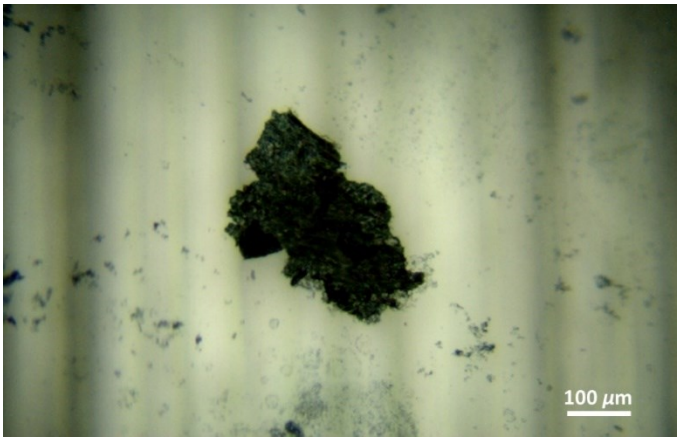

Figure 4.61. Microscope picture (20x optical zoom magnification) of one the dark colored agglomerates found at the interface D.2.

Figure 4.62 shows the averaged spectrum of three microbeads belonging to phase D.3, the most similar to the pre-degradation condition from the macroscopic point of view, as well as the microscopic. As in the previous cases, it is possible to observe a permanence of the active principle in the core of the analyzed microbeads, as evidenced by the peak at 741 cm^{-1}. Its absolute intensity decreases with respect to that of beads of similar dimensions from formulation D, before the degradation. However, the decrease is smaller than that observed for formulations B and C. Furthermore, this peak appears to have grown in absolute intensity with respect to the same peaks analyzed for the post-degradation B and C microbeads. We therefore observe Raman counts equal to 4390 for the microbeads of D, against 3024 for C and 2322 for B, as reported before. An unequivocal growing trend passing from B to D can be found, as will be explained in detail in the next and final chapter.

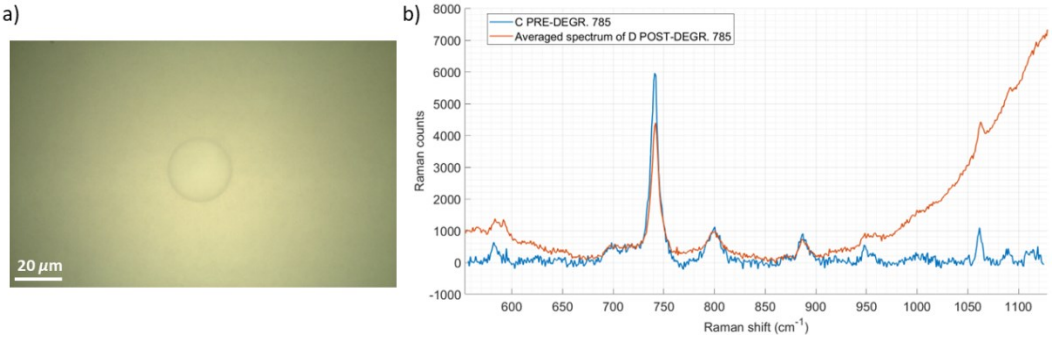

Figure 4.62. a) 50x zoom magnification image of phase D.3 after irradiation. b) Averaged (n=3) Raman spectrum of microbeads from phase D.3, after degradation (orange), compared to the spectrum of a bead of similar dimensions from formulation D, before degradation (blue).

It was considered appropriate to study in detail the morphology of D microbeads after the photodegradation process, since formulation D is virtually identical to formulation C, except for

the presence of chitosan modified with AuNSs. This has been achieved with the 2D Raman map presented in **Figure 4.63** and **4.64**. As for the results described above regarding formulation C, the R-values of the dataset spectra compared to the terpenoids mixture reference spectrum are not very high (≤0.33). Still, it can be said that the active ingredient is certainly preferentially localized within the core of the analyzed microbead (**Figure 4.63.a**).

Regarding AuNS@NBSH@CHTS, their contributions present a higher Pearson's R-value (≤0.59), and the spectra are found to have a higher signal-to-noise ratio with respect to the terpenoids ones. The localization of the AuNSs appears to be outside the core of the microbeads (**Figure 4.64.a**).

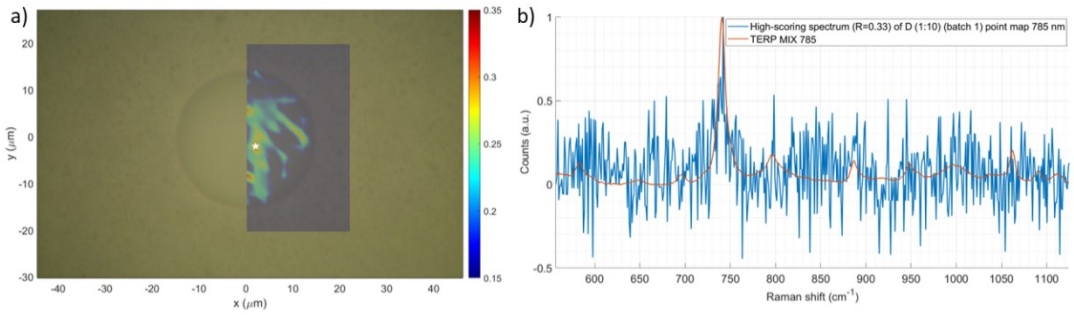

Figure 4.63. a) 2D Raman map of formulation D (1:10) post-degradation, 785 nm laser line. Pearson's correlation coefficient (R) analysis, reference: terpenes mix. The white star points to the location of the high-scoring Pearson's R spectrum appointed in section (b). b) High-scoring Pearson's R spectrum (R≃0.33) compared to terpenes mix reference spectrum.

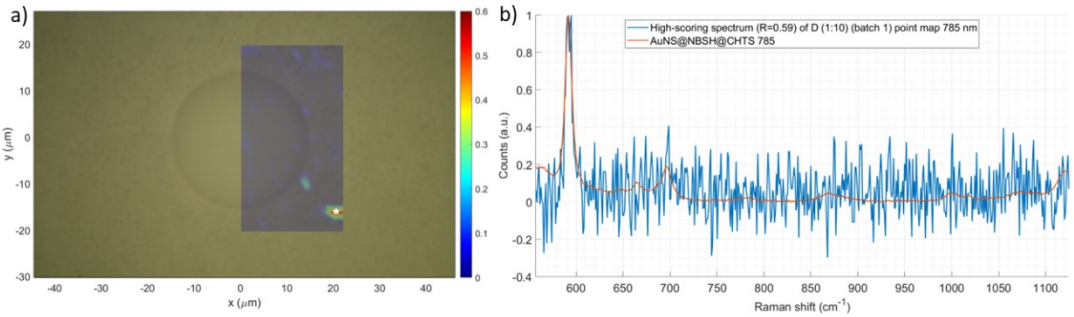

Figure 4.64. a) 2D Raman map of formulation D (1:10) post-degradation, 785 nm laser line. Pearson's correlation coefficient (R) analysis, reference: AuNS@NBSH@CHTS. The white star points to the location of the high-scoring Pearson's R spectrum appointed in section (b). b) High-scoring Pearson's R spectrum (R≃0.59) compared to AuNS@NBSH@CHTS reference spectrum.

4.3.5 Photodegradation of the terpenoids mixture: results

Figure 4.65 shows the averaged Raman spectrum of the terpenoids mixture after the degradation process.

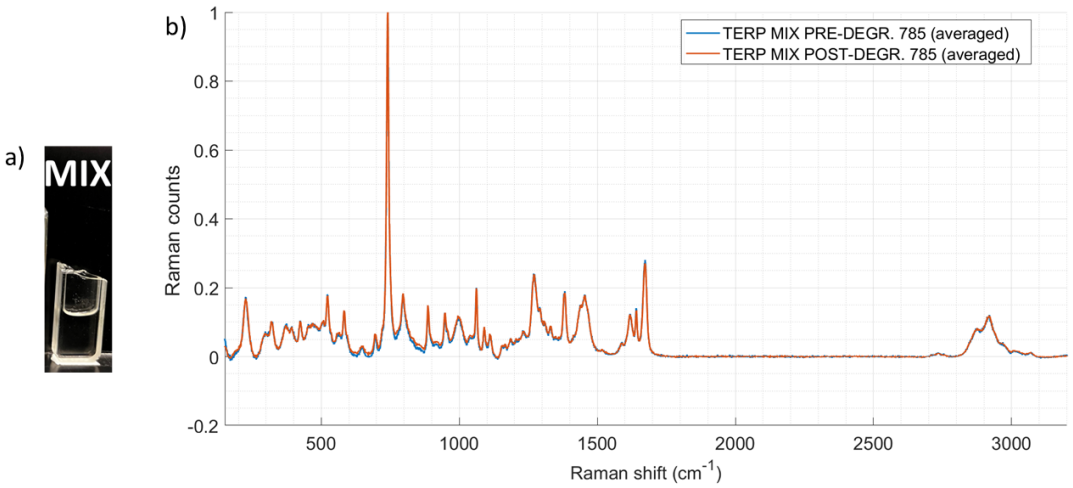

Figure 4.65. Picture of the terpenoids mixture after degradation (a). Raman spectrum of the terpenoids mixture after the degradation (orange) compared to the Raman spectrum of condition prior to the degradation (blue) (b); 785 nm excitation.

No change is visible in the position of peaks. The peak at 192 cm^{-1} found in all formulations is not present in the spectrum of the degraded terpenoid mixture. Given the presence of this peak in all degraded formulations, its attribution is certainly attributable to one or more compounds present in the simpler formulation (A): in fact, all the compounds present in formulation A are also present from formulation B onward, as highlighted in **Section 3.2.3**. As can be seen from **Figure 4.65**, the degraded terpenoids mixture does not show a peak at 192 cm^{-1}. Moreover, the terpenoid mixture has no water content inside, unlike the formulations. It is therefore reasonable to ascribe the peak at 192 cm^{-1} as the contribution from an oxidation product (unfortunately, not better defined) due to the oxygen content present in formulations, intended as part of H_2O and as dissolved $O_{2(aq.)}$, as widely supported by the literature reported in **Section 2.1.2**.

The next chapter will address in detail the final considerations regarding the stability of microbeads subject to degradation.

4.3.6 Comparative evaluation of the different formulations subject to degradation

In previous chapters, a net increase in absolute intensities of the terpenoids diagnostic peak, acquired inside the cores of post-degradation microbeads, was reported. This increase was compared with the same acquisition conditions and is therefore representative of the amount of active ingredient remaining in the core of the microbeads after the degradation process. **Figure 4.66** shows an overlap of all the spectra acquired by focusing on the core of the survived microbeads, as well as on phase A.2, which did not present any micelle. To better evaluate the contributions of the different active principles, only a representative peak for each component was selected. Specifically, the peaks at 741, 796 and 2918 cm^{-1} are reported, attributable to thymol, eugenol and geraniol, respectively. As anticipated before, all the peaks show an increasing trend in the absolute intensity from formulations A towards D after the degradation, although they have a lower intensity than the pristine samples.

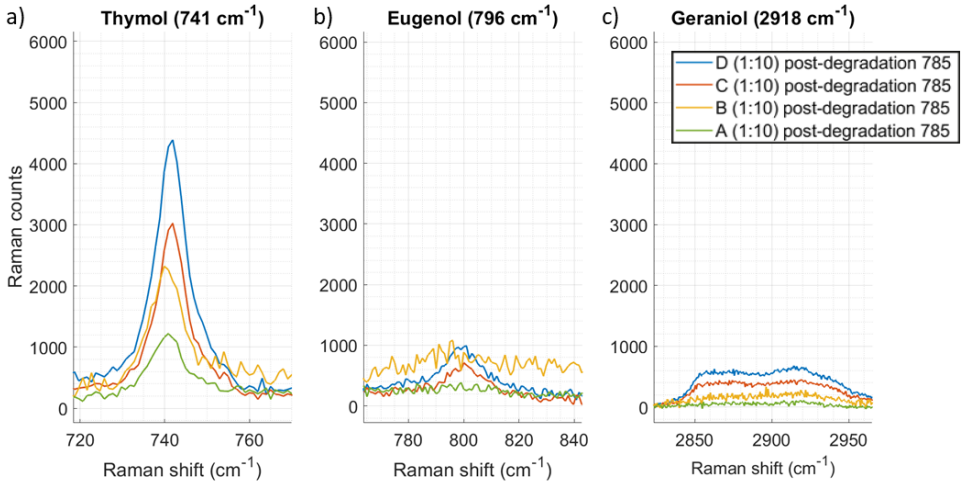

Figure 4.66. General trends of selected peaks for thymol, eugenol, and geraniol before and after degradation.

The intensities of the pristine samples were evaluated starting from the data obtained in **Section 4.2.1**, during the acquisition phase of the point Raman maps. To evaluate the differences in intensity of the peaks before and after degradation it was therefore necessary to equalize the experimental conditions. First, the spectra were corrected by the laser power and acquisition time used to acquire pre- and post-degradation spectra of the same sample. Second, only microbeads of the same dimensions were considered along the pre- and post-degradation (a value of zero was assigned to degraded A as no beads were recovered). The results of this extrapolation are displayed in **Figure 4.67**, showing the absolute intensities of thymol peaks acquired at the core of the microbeads, before and after the degradation process across formulations B to D. The absolute intensities of these peaks are also reported in **Table 4.7**. It was not necessary to repeat

the analysis for the other peaks, as it was already discussed that the overall spectral shape is retained before and after the UV-irradiation.

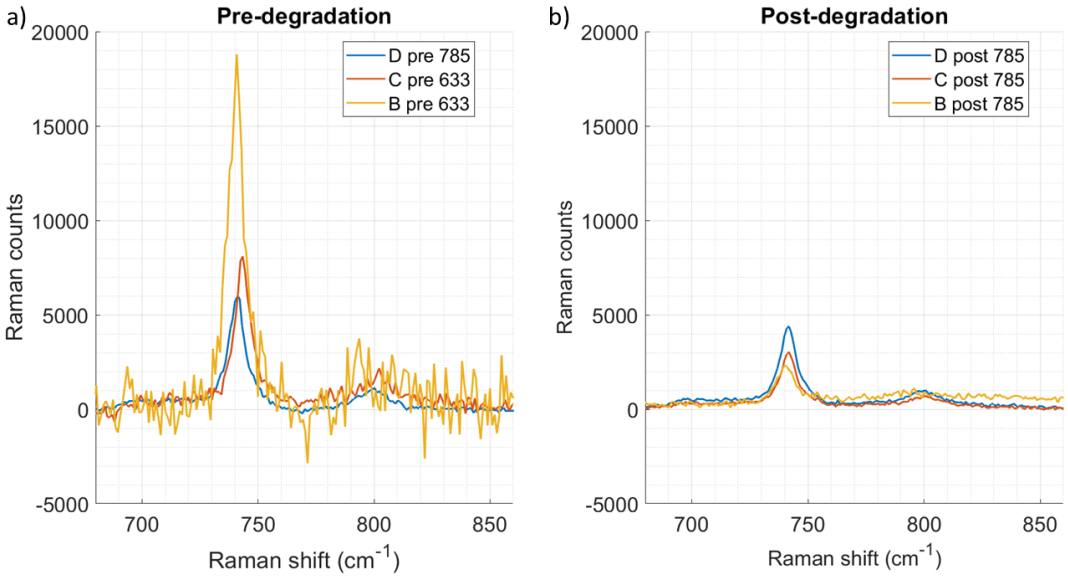

Figure 4.67. Absolute intensities of the thymol peaks acquired at the core of the microbeads, before and after the degradation process

Table 4.7. Numerical values for the absolute intensities of the thymol peaks acquired in the core of the microbeads, before and after the degradation process.

Formulation	Intensity PRE (Raman counts)	Intensity POST (Raman counts)	Difference PRE-POST (Raman counts)	Ratio POST/PRE
B	18792	2322	16470	0,12
C	8105	3024	5081	0,37
D	5953	4390	1563	0,74

One can clearly see that the intensity differences become smaller as the formulations progress in complexity and photoprotection degree, as well as the ratio of the band intensities becomes increasingly larger, as shown in **Figure 4.68**.

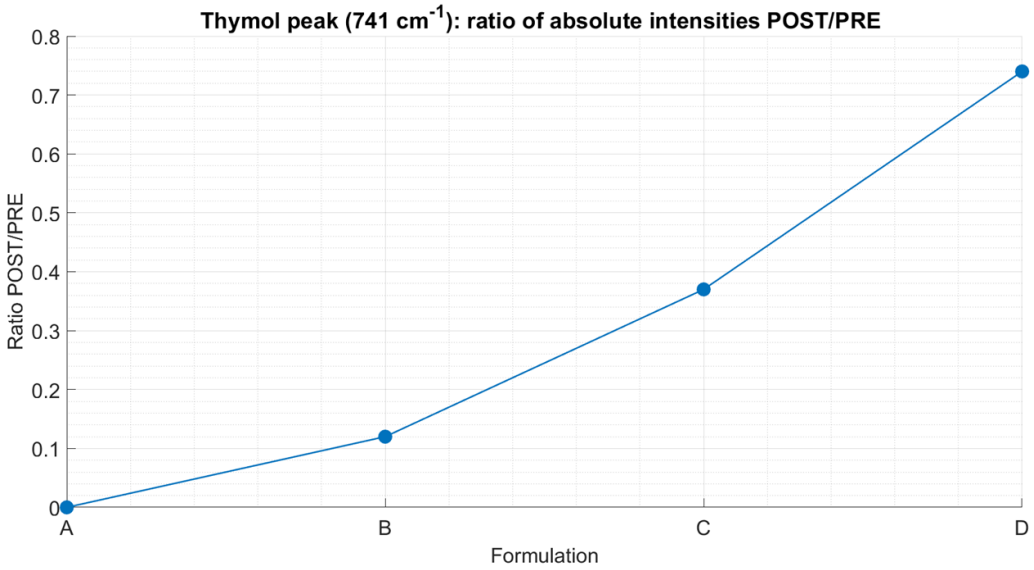

Figure 4.68. Ratio of the intensities post-degradation to that of pre-degradation, as the complexity of the formulations increases.

This trend would thus seem to confirm a progressively more efficient retention of the active ingredient as the complexity of the formulation increases, according to the initial hypothesis argued in **Section 4.1.1**. One possible critical issue, however, remains: the sampling was performed by acquiring spectra in the core of the microbeads, and thus the volume sampled, all conditions being equal, remains the same. All recorded contributions are generated by the same volume of active ingredient contained in microbeads, from formulation B to D. Nonetheless, the already described differences between pre- and post-degradation intensities of the terpenoids diagnostic peak were observed. This would suggest that the local concentration of terpenoids in the core decreased over the course of degradation, to an ever-decreasing extent from B to D. Even so, it is still not clear what is supposed to replace terpenoids within microbeads of the same nominal size. Further investigation will be focused on this specific direction.

5. Conclusions

During the course of this thesis work, an experimental design was developed to test the degree of photoprotection and stability of formulations encapsulating a mixture of terpenoids. Said formulations have been subjected to extensive morphological and spectroscopic characterization prior to the photodegradation conditions. These were chosen as similar to the environmental ones, to simulate the conditions that they should be able to sustain during their usage in fields and crops. It has been found that the microbeads tend to release the active principle more markedly if they are subjected to UV radiation for a prolonged period of time, and that the phases in which the formulations separate follow the coalescence process typical of a density-driven segregation.

Alongside the analysis of the photodegradation processes, a characterization by means of Raman maps has allowed to establish the correct localization of most components, both before and after the degradation process. Indeed, the bioactive principles (the mixture of terpenoids), as well as the dispersing oil phase (AMD 10), were found in the core of the microbeads. In addition, the statistical analysis of the contributions of each terpenoid made it possible to establish that the same proportion was always present within all the microbeads analyzed, indicating a homogeneous encapsulation for the three different components, namely thymol, eugenol, geraniol. Other primary components, such as soybean lecithin, could not be localized due to their intrinsic low concentration within the morphological structure of the microbeads. Components difficult to identify because of their low Raman scattering cross-section, such as chitosan, have been identified and localized in the shell of microbeads thanks to the exploitation of the SERS effect. This was brought by Au nanostars functionalized with chitosan and with the SERS reporter Nile blue A. In addition to acting as plasmonic components capable of stimulating the SERS effect, AuNSs have also been used by virtue of their wide absorption in the visible, up to the near IR (NIR) range. This theoretical degree of protection was tested during the photodegradation experiments of the microbeads. Analyzing the quantity of active ingredient contained in the core of the microbeads after photodegradation and comparing it with the same quantity prior to the photodegradation progress, it was found that the microbeads containing AuNSs within the chitosan shell are the most stable. In fact, they retain the active ingredient in their core more effectively, ensuring greater and longer bioavailability over time.

6. Bibliography

(1) Sell, C. S. *A Fragrant Introduction to Terpenoid Chemistry*; The Royal Society of Chemistry: Cambridge, 2003.

(2) Ruzicka, L. The Isoprene Rule and the Biogenesis of Terpenic Compounds. *Experientia* **1953**, *9* (10), 357–396. https://doi.org/10.1007/BF02167631.

(3) Perveen, S. Introductory Chapter: Terpenes and Terpenoids. In *Terpenes and Terpenoids*; IntechOpen, 2018. https://doi.org/10.5772/intechopen.79683.

(4) Masyita, A.; Mustika Sari, R.; Dwi Astuti, A.; Yasir, B.; Rahma Rumata, N.; Emran, T. bin; Nainu, F.; Simal-Gandara, J. Terpenes and Terpenoids as Main Bioactive Compounds of Essential Oils, Their Roles in Human Health and Potential Application as Natural Food Preservatives. *Food Chem X* **2022**, *13*. https://doi.org/10.1016/j.fochx.2022.100217.

(5) Turek, C.; Stintzing, F. C. Stability of Essential Oils: A Review. *Compr Rev Food Sci Food Saf* **2013**, *12* (1), 40–53. https://doi.org/10.1111/1541-4337.12006.

(6) Zhang, H. J.; Tan, G. T.; Santarsiero, B. D.; Mesecar, A. D.; van Hung, N.; Cuong, N. M.; Soejarto, D. D.; Pezzuto, J. M.; Fong, H. H. S. New Sesquiterpenes from Litsea Verticillata. *J Nat Prod* **2003**, *66* (5), 609–615. https://doi.org/10.1021/np020508a.

(7) Nita Yadav; Rajesh Yadav; Murli Dhar Kharya. Chemistry of Terpenoids. *International Journal of Pharmaceutical Sciences Review and Research* **2014**, *27* (2), 272–278.

(8) Dehsheikh, A. B.; Sourestani, M. M.; Dehsheikh, P. B.; Mottaghipisheh, J.; Vitalini, S.; Iriti, M. Monoterpenes: Essential Oil Components with Valuable Features. *Mini-Reviews in Medicinal Chemistry* **2020**, *20* (11), 958–974. https://doi.org/10.2174/1389557520666200122144703.

(9) Triaux, Z.; Petitjean, H.; Marchioni, E.; Steyer, D.; Marcic, C. Comparison of Headspace, Hydrodistillation and Pressurized Liquid Extraction of Terpenes and Terpenoids from Food Matrices—Qualitative and Quantitative Analysis. *Journal of Analytical Chemistry* **2021**, *76* (3), 284–295. https://doi.org/10.1134/S1061934821030151.

(10) Pavlić, B.; Teslić, N.; Zengin, G.; Đurović, S.; Rakić, D.; Cvetanović, A.; Gunes, A. K.; Zeković, Z. Antioxidant and Enzyme-Inhibitory Activity of Peppermint Extracts and Essential Oils Obtained by Conventional and Emerging Extraction Techniques. *Food Chem* **2021**, *338*. https://doi.org/10.1016/j.foodchem.2020.127724.

(11) Essien, S. O.; Young, B.; Baroutian, S. Recent Advances in Subcritical Water and Supercritical Carbon Dioxide Extraction of Bioactive Compounds from Plant Materials. *Trends Food Sci Technol* **2020**, *97*, 156–169. https://doi.org/10.1016/j.tifs.2020.01.014.

(12) Isman, M. B. Pesticides Based on Plant Essential Oils: From Traditional Practice to Commercialization. In *Naturally Occurring Bioactive Compounds*; Elsevier, 2006; Vol. 3, pp 29–44.

(13) Pandey, A. K.; Sonker, N.; Singh, P. Efficacy of Some Essential Oils Against Aspergillus Flavus with Special Reference to Lippia Alba Oil an Inhibitor of Fungal Proliferation and Aflatoxin B1 Production in Green Gram Seeds during Storage. *J Food Sci* **2016**, *81* (4), M928–M934. https://doi.org/10.1111/1750-3841.13254.

(14) Aktar, W.; Sengupta, D.; Chowdhury, A. Impact of Pesticides Use in Agriculture: Their Benefits and Hazards. *Interdiscip Toxicol* **2009**, *2* (1), 1–12. https://doi.org/10.2478/v10102-009-0001-7.

(15) Pavela, R.; Benelli, G. Essential Oils as Ecofriendly Biopesticides? Challenges and Constraints. *Trends Plant Sci* **2016**, *21* (12), 1000–1007. https://doi.org/10.1016/j.tplants.2016.10.005.

(16) Sankhla, M. S.; Parihar, K.; Kumar, R.; Bhagat, D. S.; Sonone, S. S.; Singh, G. K.; Nagar, V.; Awasthi, G.; Yadav, C. S. Ecofriendly Approach for Steroids, Terpenes, and Alkaloids-Based Biosurfactant. *Biointerface Res Appl Chem* **2023**, *13* (2). https://doi.org/10.33263/BRIAC132.114.

(17) Tabari, M. A.; Rostami, A.; Khodashenas, A.; Maggi, F.; Petrelli, R.; Giordani, C.; Tapondjou, L. A.; Papa, F.; Zuo, Y.; Cianfaglione, K.; Youssefi, M. R. Acaricidal Activity, Mode of Action, and Persistent Efficacy of Selected Essential Oils on the Poultry Red Mite (Dermanyssus Gallinae). *Food and Chemical Toxicology* **2020**, *138*. https://doi.org/10.1016/j.fct.2020.111207.

(18) Liu, Z.; Li, Q. X.; Song, B. Pesticidal Activity and Mode of Action of Monoterpenes. *J Agric Food Chem* **2022**, *70* (15), 4556–4571. https://doi.org/10.1021/acs.jafc.2c00635.

(19) dos Santos, M. C.; Teodoro, A. V.; Menezes, M. S.; Pinto-Zevallos, D. M.; de Fátima Arrigoni-Blank, M.; Cruz Oliveira, E. M.; Sampaio, T. S.; Farias, A. P.; Coelho, C. R.; Blank, A. F. Bioactivity of Essential Oil from Lippia Gracilis Schauer against Two Major Coconut Pest Mites and Toxicity to a Non-Target Predator. *Crop Protection* **2019**, *125*. https://doi.org/10.1016/j.cropro.2019.104913.

(20) Kordali, S.; Cakir, A.; Ozer, H.; Cakmakci, R.; Kesdek, M.; Mete, E. Antifungal, Phytotoxic and Insecticidal Properties of Essential Oil Isolated from Turkish Origanum Acutidens and Its Three Components, Carvacrol, Thymol and p-Cymene. *Bioresour Technol* **2008**, *99* (18), 8788–8795. https://doi.org/10.1016/j.biortech.2008.04.048.

(21) Gaire, S.; Scharf, M. E.; Gondhalekar, A. D. Synergistic Toxicity Interactions between Plant Essential Oil Components against the Common Bed Bug (Cimex Lectularius L.). *Insects* **2020**, *11* (2). https://doi.org/10.3390/insects11020133.

(22) Ministero della Salute. *Area tematica Prodotti fitosanitari: Archivio banche dati. As visited on 3 Sep 2022: <http://www.fitosanitari.salute.gov.it/fitosanitariwsWeb_new/FitosanitariServlet?ACTION=cercaSostanza&FROM=0&TO=49&PROVENIENZA=LISTA&SOST=1314,1304,>*. http://www.fitosanitari.salute.gov.it/fitosanitariwsWeb_new/Fitosanita...

(23) Eastman S.R.L. *Cedroz - Product description. As visited on 1 Sep 2022: <https://www.eastman.com/Pages/ProductHome.aspx?product=71111396&pn=Cedroz>*.

(24) Sipcam Italia S.P.A. *3LOGY. As visited on 1 Sep 2022: <http://www.sipcamitalia.it/it/fungicidi/25/3logy/X/16396>*.

(25) Bernhard, R. A.; Marr, A. G. The Oxidation of Terpenes. I. Mechanism and Reaction Products of D-Limonene Autoxidation. *J Food Sci* **1960**, *25* (4), 517–530.

(26) Sköld, M.; Börje, A.; Harambasic, E.; Karlberg, A. T. Contact Allergens Formed on Air Exposure of Linalool. Identification and Quantification of Primary and Secondary Oxidation Products and the Effect on Skin Sensitization. *Chem Res Toxicol* **2004**, *17* (12), 1697–1705. https://doi.org/10.1021/tx049831z.

(27) Neuenschwander, U.; Hermans, I. Autoxidation of α-Pinene at High Oxygen Pressure. *Physical Chemistry Chemical Physics* **2010**, *12* (35), 10542–10549. https://doi.org/10.1039/c0cp00010h.

(28) Neuenschwander, U.; Guignard, F.; Hermans, I. Mechanism of the Aerobic Oxidation of α-Pinene. *ChemSusChem* **2010**, *3* (1), 75–84. https://doi.org/10.1002/cssc.200900228.

(29) Choe, E.; Min, D. B. Mechanisms and Factors for Edible Oil Oxidation. *Compr Rev Food Sci Food Saf* **2006**, *5* (4), 169–186.

(30) Brophy, J. J.; Davies, N. W.; Southwell, I. A.; Stiff, I. A.; Williams, L. R. Gas Chromatographic Quality Control for Oil of Melaleuca Terpinen-4-Ol Type (Australian Tea Tree). **1989**, *37*, 1330–1335.

(31) Misharina, T. A. Changes in the Composition of the Essential Oil of Marjoram during Storage. *Appl Biochem Microbiol* **2003**, *39* (3), 311–316. https://doi.org/10.1023/A:1023592030874.

(32) Bäcktorp, C.; Wass, J. R. T. J.; Panas, I.; Sköld, M.; Börje, A.; Nyman, G. Theoretical Investigation of Linalool Oxidation. *Journal of Physical Chemistry A* **2006**, *110* (44), 12204–12212. https://doi.org/10.1021/jp0603278.

(33) de Oliveira, J. L.; Campos, E. V. R.; Pereira, A. E. S.; Nunes, L. E. S.; da Silva, C. C. L.; Pasquoto, T.; Lima, R.; Smaniotto, G.; Polanczyk, R. A.; Fraceto, L. F. Geraniol Encapsulated in Chitosan/Gum Arabic Nanoparticles: A Promising System for Pest Management in Sustainable Agriculture. *J Agric Food Chem* **2018**, *66* (21), 5325–5334. https://doi.org/10.1021/acs.jafc.8b00331.

(34) Glasl, H. On the Shelf Life of Terpenoids in Extracts and Solutions with Different Alcohol Content. *Arch Pharm (Weinheim)* **1975**, *308* (2), 88–93. https://doi.org/10.1002/ardp.19753080203.

(35) Mcgraw, G. W.; Hemingway, R. W.; Ingram, L. L.; Canady,' And, C. S.; Mcgraw+, W. B. Thermal Degradation of Terpenes: Camphene, A3-Carene, Limonene, and Ot=Terpinene. *Environ. Sci. Technol* **1999**, *33*, 4029–4033. https://doi.org/10.1021/es9610641.

(36) Geier K. Quality Assurance of Essential Oils., Technical Univ., Munich, 2006.

(37) Rowshan, V.; Bahmanzadegan, A.; Saharkhiz, M. J. Influence of Storage Conditions on the Essential Oil Composition of Thymus Daenensis Celak. *Ind Crops Prod* **2013**, *49*, 97–101. https://doi.org/10.1016/j.indcrop.2013.04.029.

(38) Bollmann, M. The Essential Oils by E. Gildemeister and Fr. Hoffmann. *Angewandte Chemie* **1956**, *68* (22), 720–720. https://doi.org/10.1002/ange.19560682231.

(39) Nanditha, B.; Prabhasankar, P. Antioxidants in Bakery Products: A Review. *Crit Rev Food Sci Nutr* **2009**, *49* (1), 1–27. https://doi.org/10.1080/10408390701764104.

(40) Tiwari, N.; Ebenazer, A.; Franklyne, J. S.; Sivakumar, A.; Mukherjee, A.; Chandrasekaran, N. Drug Loaded Essential Oil Microemulsions Enhance Photostability and Evaluation of in Vitro Efficacy. *Photodiagnosis Photodyn Ther* **2020**, *29*. https://doi.org/10.1016/j.pdpdt.2019.101638.

(41) Campolo, O.; Giunti, G.; Laigle, M.; Michel, T.; Palmeri, V. Essential Oil-Based Nano-Emulsions: Effect of Different Surfactants, Sonication and Plant Species on Physicochemical Characteristics. *Ind Crops Prod* **2020**, *157*. https://doi.org/10.1016/j.indcrop.2020.112935.

(42) Krzyżowski, M.; Baran, B.; Łozowski, B.; Francikowski, J. The Role of Dilution Mediums in Studies of Fumigant Insecticidal Activity of Essential Oils. *J Pest Sci (2004)* **2020**, *93* (4), 1119–1124. https://doi.org/10.1007/s10340-020-01241-7.

(43) Ibáñez, M. D.; Blázquez, M. A. Phytotoxic Effects of Commercial Essential Oils on Selected Vegetable Crops: Cucumber and Tomato. *Sustain Chem Pharm* **2020**, *15*. https://doi.org/10.1016/j.scp.2019.100209.

(44) Rodríguez, J.; Martín, M. J.; Ruiz, M. A.; Clares, B. Current Encapsulation Strategies for Bioactive Oils: From Alimentary to Pharmaceutical Perspectives. *Food Research International* **2016**, *83*, 41–59. https://doi.org/10.1016/j.foodres.2016.01.032.

(45) Sagalowicz, L.; Leser, M. E. Delivery Systems for Liquid Food Products. *Curr Opin Colloid Interface Sci* **2010**, *15* (1–2), 61–72. https://doi.org/10.1016/j.cocis.2009.12.003.

(46) Sri, J. S.; Seethadevi, A.; Prabha, K. S.; Muthuprasanna, P.; Pavitra, P. Microencapsulation: A Review. **2012**, 512–531.

(47) Sagis, L. *Microencapsulation and Microspheres for Food Applications*, 1st ed.; Elsevier, 2015.

(48) Chen, Q.; Zhong, F.; Wen, J.; McGillivray, D.; Quek, S. Y. Properties and Stability of Spray-Dried and Freeze-Dried Microcapsules Co-Encapsulated with Fish Oil, Phytosterol Esters, and Limonene. *Drying Technology* **2013**, *31* (6), 707–716. https://doi.org/10.1080/07373937.2012.755541.

(49) Heidebach, T.; Först, P.; Kulozik, U. Microencapsulation of Probiotic Cells for Food Applications. *Crit Rev Food Sci Nutr* **2012**, *52* (4), 291–311. https://doi.org/10.1080/10408398.2010.499801.

(50) Zuidam, J.; Nedović, V. *Encapsulation Technologies for Active Food Ingredients and Food Processing*, 1st ed.; Elsevier, 2012.

(51) Wang, B.; Adhikari, B.; Barrow, C. J. Optimisation of the Microencapsulation of Tuna Oil in Gelatin-Sodium Hexametaphosphate Using Complex Coacervation. *Food Chem* **2014**, *158*, 358–365. https://doi.org/10.1016/j.foodchem.2014.02.135.

(52) Kamkar, A.; Molaee-aghaee, E.; Khanjari, A.; Akhondzadeh-basti, A.; Noudoost, B.; Shariatifar, N.; Alizadeh Sani, M.; Soleimani, M. Nanocomposite Active Packaging Based on Chitosan Biopolymer Loaded with Nano-Liposomal Essential Oil: Its Characterizations and Effects on Microbial, and Chemical Properties of Refrigerated Chicken Breast Fillet. *Int J Food Microbiol* **2021**, *342*. https://doi.org/10.1016/j.ijfoodmicro.2021.109071.

(53) Sani, M. A.; Tavassoli, M.; Hamishehkar, H.; McClements, D. J. Carbohydrate-Based Films Containing PH-Sensitive Red Barberry Anthocyanins: Application as Biodegradable Smart Food Packaging Materials. *Carbohydr Polym* **2021**, *255*. https://doi.org/10.1016/j.carbpol.2020.117488.

(54) Scholfield, C. R. *Composition of Soybean Lecithin*; 1981; Vol. 58.

(55) Wu, Y.; Wang, T. Soybean Lecithin Fractionation and Functionality. *JAOCS, Journal of the American Oil Chemists' Society* **2003**, *80* (4), 319–326. https://doi.org/10.1007/s11746-003-0697-x.

(56) van Nieuwenhuyzen, W.; Szuhaj, B. F. Effects of Lecithins and Proteins on the Stability of Emulsions. *Lipid - Fett* **1998**, *100* (7), 282–291. https://doi.org/10.1002/(SICI)1521-4133(199807)100:7<282::AID-LIPI282>3.0.CO;2-W.

(57) Ogawa, S.; Decker, E. A.; McClements, D. J. Production and Characterization of O/W Emulsions Containing Cationic Droplets Stabilized by Lecithin - Chitosan Membranes. *J Agric Food Chem* **2003**, *51* (9), 2806–2812. https://doi.org/10.1021/jf020590f.

(58) Adriana, R. M.; Leticia, M. de A.; Maria, I. R. M.; Leonor, A. de S.-S. Importance of Lecithin for Encapsulation Processes. *African Journal of Food Science* **2014**, *8* (4), 176–183. https://doi.org/10.5897/ajfs2013.1092.

(59) Mondéjar-López, M.; López-Jimenez, A. J.; García Martínez, J. C.; Ahrazem, O.; Gómez-Gómez, L.; Niza, E. Comparative Evaluation of Carvacrol and Eugenol Chitosan Nanoparticles as Eco-Friendly Preservative Agents in Cosmetics. *Int J Biol Macromol* **2022**, *206*, 288–297. https://doi.org/10.1016/j.ijbiomac.2022.02.164.

(60) Huang, D.; Boxin, O. U.; Prior, R. L. The Chemistry behind Antioxidant Capacity Assays. *J Agric Food Chem* **2005**, *53* (6), 1841–1856. https://doi.org/10.1021/jf030723c.

(61) Ogawa, S.; Decker, E. A.; McClements, D. J. Influence of Environmental Conditions on the Stability of Oil in Water Emulsions Containing Droplets Stabilized by Lecithin-Chitosan Membranes. *J Agric Food Chem* **2003**, *51* (18), 5522–5527. https://doi.org/10.1021/jf026103d.

(62) Mei, L.; Decker, E. A.; McClements, D. J. Evidence of Iron Association with Emulsion Droplets and Its Impact on Lipid Oxidation. *J Agric Food Chem* **1998**, *46* (12), 5072–5077. https://doi.org/10.1021/jf9806661.

(63) Carvalho, A. G. S.; Silva, V. M.; Hubinger, M. D. Microencapsulation by Spray Drying of Emulsified Green Coffee Oil with Two-Layered Membranes. *Food Research International* **2014**, *61*, 236–245. https://doi.org/10.1016/j.foodres.2013.08.012.

(64) Metrohm. *Oxidation stability of oils and fats – Rancimat. As visited on 6 Sep 2022: <methodhttps://www.metrohm.com/en_us/applications/ab-application-bulletins/ab-204.html>*.

(65) Nusinov, A. A.; Tobiska, W. K. Status of ISO Draft International Standard for Determining Solar Irradiances (DIS 21348). In *35th COSPAR Scientific Assembly*; Paris, 2004; p 900.

(66) Nasir, A. Photoprotection in the Era of Nanotechnology. In *Principles and Practice of Photoprotection*; Springer International Publishing, 2016; pp 335–360. https://doi.org/10.1007/978-3-319-29382-0_19.

(67) Borase, H. P.; Patil, C. D.; Salunkhe, R. B.; Suryawanshi, R. K.; Salunke, B. K.; Patil, S. v. Phytolatex Synthesized Gold Nanoparticles as Novel Agent to Enhance Sun Protection Factor of Commercial Sunscreens. *Int J Cosmet Sci* **2014**, *36* (6), 571–578. https://doi.org/10.1111/ics.12158.

(68) Rizzi, V.; Gubitosa, J.; Fini, P.; Nuzzo, S.; Agostiano, A.; Cosma, P. Snail Slime-Based Gold Nanoparticles: An Interesting Potential Ingredient in Cosmetics as an Antioxidant, Sunscreen, and Tyrosinase Inhibitor. *J Photochem Photobiol B* **2021**, *224*. https://doi.org/10.1016/j.jphotobiol.2021.112309.

(69) Gubitosa, J.; Rizzi, V.; Fini, P.; del Sole, R.; Lopedota, A.; Laquintana, V.; Denora, N.; Agostiano, A.; Cosma, P. Multifunctional Green Synthetized Gold Nanoparticles/Chitosan/Ellagic Acid Self-Assembly: Antioxidant, Sun Filter and Tyrosinase-Inhibitor Properties. *Materials Science and Engineering C* **2020**, *106*. https://doi.org/10.1016/j.msec.2019.110170.

(70) nobleprize.org. *The Nobel Prize in Physics, 1930. As visited on 6 Sep 2022: <https://www.nobelprize.org/prizes/physics/1930/summary/>*.

(71) Smith, E.; Dent, G. *Modern Raman Spectroscopy: A Practical Approach*, 2nd edition.; Elsevier, 2017.

(72) Edinburgh Instruments. *What is Raman spectroscopy? As visited on 6 Sep 2022: <https://www.edinst.com/blog/what-is-raman-spectroscopy/>*.

(73) Long, D. A. *The Raman Effect: A Unified Treatment of the Theory of Raman Scattering by Molecules*; Wiley, 2002.

(74) Spring, K. R.; Fellers, T. J.; Davidson, M. W. *Resolution and Contrast in Confocal Microscopy. As visited on 7 Sep 2022: <http://www.olympusconfocal.com/theory/resolutionintro.html>*.

(75) Jimenez de Aberasturi, D.; Henriksen-Lacey, M.; Litti, L.; Langer, J.; Liz-Marzán, L. M. Using SERS Tags to Image the Three-Dimensional Structure of Complex Cell Models. *Adv Funct Mater* **2020**, *30* (14). https://doi.org/10.1002/adfm.201909655.

(76) Fleischmann, M.; Hendra, P. J.; Mcquillan, A. J. Raman Spectra of Pyridine Adsorbed at a Silver Electrode. *Chem Phys Lett* **1974**, *26* (2), 163–166.

(77) Rodrigues, M. S.; Borges, J.; Lopes, C.; Pereira, R. M. S.; Vasilevskiy, M. I.; Vaz, F. Gas Sensors Based on Localized Surface Plasmon Resonances: Synthesis of Oxide Films with Embedded Metal Nanoparticles, Theory and Simulation, and Sensitivity Enhancement Strategies. *Applied Sciences (Switzerland)* **2021**, *11* (12). https://doi.org/10.3390/app11125388.

(78) Maher, R. C. SERS Hot Spots. In *Raman Spectroscopy for Nanomaterials Characterization*; Springer-Verlag Berlin Heidelberg, 2011; pp 215–260. https://doi.org/10.1007/978-3-642-20620-7_10.

(79) Langer, J.; de Aberasturi, D. J.; Aizpurua, J.; Alvarez-Puebla, R. A.; Auguié, B.; Baumberg, J. J.; Bazan, G. C.; Bell, S. E. J.; Boisen, A.; Brolo, A. G.; Choo, J.; Cialla-May, D.; Deckert, V.; Fabris, L.; Faulds, K.; Javier García de Abajo, F.; Goodacre, R.; Graham, D.; Haes, A. J.; Haynes, C. L.; Huck, C.; Itoh, T.; Käll, M.; Kneipp, J.; Kotov, N. A.; Kuang, H.; le Ru, E. C.; Lee, H. K.; Li, J. F.; Ling, X. Y.; Maier, S. A.; Mayerhöfer, T.; Moskovits, M.; Murakoshi, K.; Nam, J. M.; Nie, S.; Ozaki, Y.; Pastoriza-Santos, I.; Perez-Juste, J.; Popp, J.; Pucci, A.; Reich, S.; Ren, B.; Schatz, G. C.; Shegai, T.; Schlücker, S.; Tay, L. L.; George Thomas, K.; Tian, Z. Q.; van Duyne, R. P.; Vo-Dinh, T.; Wang, Y.; Willets, K. A.; Xu, C.; Xu, H.; Xu, Y.; Yamamoto, Y. S.; Zhao, B.; Liz-Marzán, L. M. Present and Future of Surface-Enhanced Raman Scattering. *ACS Nano* **2020**, *14* (1), 28–117. https://doi.org/10.1021/acsnano.9b04224.

(80) Radziuk, D.; Moehwald, H. Prospects for Plasmonic Hot Spots in Single Molecule SERS towards the Chemical Imaging of Live Cells. *Physical Chemistry Chemical Physics* **2015**, *17* (33), 21072–21093. https://doi.org/10.1039/c4cp04946b.

(81) Kim, W.; Kim, N.; Park, J. W.; Kim, Z. H. Nanostar Probes for Tip-Enhanced Spectroscopy. *Nanoscale* **2016**, *8* (2), 987–994. https://doi.org/10.1039/c5nr06657c.

(82) Wang, L.; Wu, B.; Kang, M.; Zhang, X.; Liu, L.; Otto, A.; Mrozek, I.; Grabhorn, H. Surface-Enhanced Raman Scattering. *J. Phys.: Condens. Matter* **1992**, *4*, 1143–1212.

(83) Parkinson, M.; Mortimer, A.; Jones, C.; Larking, S.; Swartz, A. *Bancroft's Theory and Practice of Histological Techniques Content Strategist: Michael Houston Content Development Specialists*, 8th edition.; Elsevier, 2019.

(84) Edinburgh Instruments. *What are absorption, excitation and emission spectra? As visited on 18 Sep 2022: <https://www.edinst.com/blog/what-are-absorption-excitation-and-emission-spectra/>*.

(85) Baginskiy, I.; Lai, T. C.; Cheng, L. C.; Chan, Y. C.; Yang, K. Y.; Liu, R. S.; Hsiao, M.; Chen, C. H.; Hu, S. F.; Her, L. J.; Tsai, D. P. Chitosan-Modified Stable Colloidal Gold Nanostars for the Photothermolysis of Cancer Cells. *Journal of Physical Chemistry C* **2013**, *117* (5), 2396–2410. https://doi.org/10.1021/jp311271p.

(86) Sedgwick, P. Pearson's Correlation Coefficient. *BMJ (Online)* **2012**, *345* (7864). https://doi.org/10.1136/bmj.e4483.

(87) United States Department of Energy - National Renewable Energy Laboratory. *Reference Solar Spectral Irradiance: ASTM G-173. As visited on 9 Sep 2022: <http://rredc.nrel.gov/solar/spectra/am1.5/ASTMG173/ASTMG173.html>*.

(88) John Turkevich, B.; Cooper Stevenson, P.; Hillier, J. A Study of the Nucleation and Growth Processes in the Synthesis of Colloidal Gold. *Anal. Chem* **1941**, *47* (2), 475.

(89) Lai, C.; Liu, X.; Qin, L.; Zhang, C.; Zeng, G.; Huang, D.; Cheng, M.; Xu, P.; Yi, H.; Huang, D. Chitosan-Wrapped Gold Nanoparticles for Hydrogen-Bonding Recognition and Colorimetric Determination of the Antibiotic Kanamycin. *Microchimica Acta* **2017**, *184* (7), 2097–2105. https://doi.org/10.1007/s00604-017-2218-z.

(90) Sciutto, G.; Litti, L.; Lofrumento, C.; Prati, S.; Ricci, M.; Gobbo, M.; Roda, A.; Castellucci, E.; Meneghetti, M.; Mazzeo, R. Alternative SERRS Probes for the Immunochemical Localization of Ovalbumin in Paintings: An Advanced Mapping Detection Approach. *Analyst* **2013**, *138* (16), 4532–4541. https://doi.org/10.1039/c3an00057e.

(91) Chandu, B.; Sree Satya Bharati, M.; Albrycht, P.; Rao, S. V. Fabrication of Nanocages on Nickel Using Femtosecond Laser Ablation and Trace Level Detection of Malachite Green and Nile Blue Dyes Using Surface Enhanced Raman Spectroscopic Technique. *Opt Laser Technol* **2020**, *131*. https://doi.org/10.1016/j.optlastec.2020.106454.

(92) Ni, F.; Feng, H.; Gorton, L.; Cotton, T. M. Electrochemical and SERS Studies of Chemically Modified Electrodes: Nile Blue A, a Mediator for NADH Oxidation. *Langmuir* **1990**, *6* (1), 66–73. https://doi.org/https://doi.org/10.1021/la00091a010.

(93) Peter J. Larkin. *Infrared and Raman Spectroscopy: Principles and Spectral Interpretation*, Second edition.; 2018. https://doi.org/https://doi.org/10.1016/C2015-0-00806-1.

(94) Potara, M.; Maniu, D.; Astilean, S. The Synthesis of Biocompatible and SERS-Active Gold Nanoparticles Using Chitosan. *Nanotechnology* **2009**, *20* (31). https://doi.org/10.1088/0957-4484/20/31/315602.

(95) Schneider, C. A.; Rasband, W. S.; Eliceiri, K. W. NIH Image to ImageJ: 25 Years of Image Analysis. *Nat Methods* **2012**, *9* (7), 671–675. https://doi.org/10.1038/nmeth.2089.

(96) Jentzsch, P. V.; Ramos, L. A.; Ciobotă, V. Handheld Raman Spectroscopy for the Distinction of Essential Oils Used in the Cosmetics Industry. *Cosmetics* **2015**, *2* (2), 162–176. https://doi.org/10.3390/cosmetics2020162.

(97) Nirmala, R.; Il, B. W.; Navamathavan, R.; El-Newehy, M. H.; Kim, H. Y. Preparation and Characterizations of Anisotropic Chitosan Nanofibers via Electrospinning. *Macromol Res* **2011**, *19* (4), 345–350. https://doi.org/10.1007/s13233-011-0402-2.

(98) Ogruc Ildiz, G.; Celik, O.; Atak, C.; Yilmaz, A.; Kabuk, H. N.; Kaygisiz, E.; Ayan, A.; Meric, S.; Fausto, R. Raman Spectroscopic and Chemometric Investigation of Lipid–Protein Ratio Contents of Soybean Mutants. *Appl Spectrosc* **2020**, *74* (1), 34–41. https://doi.org/10.1177/0003702819859940.

(99) Kolesov, B. A. Raman Spectra of Crystalline Secondary Amides. *Spectrochim Acta A Mol Biomol Spectrosc* **2017**, *179*, 216–220. https://doi.org/10.1016/j.saa.2017.02.046.

(100) Maiti, N. C.; Apetri, M. M.; Zagorski, M. G.; Carey, P. R.; Anderson, V. E. Raman Spectroscopic Characterization of Secondary Structure in Natively Unfolded Proteins: α-Synuclein. *J Am Chem Soc* **2004**, *126* (8), 2399–2408. https://doi.org/10.1021/ja0356176.

(101) le Parc, R.; Freitas, V. T.; Hermet, P.; Cojocariu, A. M.; Cattoen, X.; Wadepohl, H.; Maurin, D.; Cheuk, H.; Tse, J. R.; Bartlett, R.; Ferreira, S.; Spectroscopy, R.; Cattoën, X.; Tse, C. H.; Bartlett, J. R.; Ferreira, R. A. S.; Carlos, L. D.; Wong, M.; Man, C.; Bantignies, J.-L. Infrared and Raman Spectroscopy of Non-Conventional Hydrogen Bonding between N,N'-Disubstituted Urea and Thiourea Groups: A Combined Experimental and Theoretical Investigation. *Physical Chemistry Chemical Physics* **2019**, *21* (6). https://doi.org/10.1039/c8cp06625fï.